Electromagnetically generated dipolar vortices in shallow stratified fluids

Wong, C.H.

Award date:
2015

Department of Applied Physics
Fluid Dynamics Laboratory
Turbulence and Vortex Dynamics
Building: Cascade
P.O. Box 513
5600 MB Eindhoven

Electromagnetically Generated Dipolar Vortices in Shallow Stratified Fluids

C.H. Wong

April 10, 2015

Supervisors:
V.H.M.R. Fernandes, Eindhoven University of Technology
L.P.J. Kamp, Eindhoven University of Technology
G.J.F. van Heijst, Eindhoven University of Technology

Abstract

Geophysical flows affect the Earth's climate and weather and in these flows, dipolar vortices play an important role. In order to gain a better understanding of dipolar vortices, they are generated and studied in the laboratory.

In this study, a novel method of electromagnetically generating symmetric dipolar vortices with improved control over propagation trajectory is investigated experimentally and numerically.
As a first step, the generated dipoles have been characterized. In the formation phase, the dipole has two closely packed concentrated vorticity patches which is point-dipole-like. In the early time stage, the dipole is similar to a super-smooth dipole and in later time stages the dipole transitions into a more Chaplygin-Lamb dipole-like structure.

Subsequently, the new generation method has been applied in various dipolar vortex collisions experiments where the collision outcomes are sensitive to small deviations in propagation trajectory, to highlight the improved control over the propagation trajectory.

Lastly, the new method has been applied in experiments with a shearing background flow to illustrate the method's minimal intrusiveness in experiments, especially with background flows.

Contents

1 Introduction **1**
- 1.1 Vortices in geophysical flows 1
- 1.2 Geophysical flows and quasi-2D flow conditions 2
- 1.3 The realization of Q2D conditions in the laboratory 3
- 1.4 Dipolar vortex generation methods 4
- 1.5 Study outline 8

2 Theory **9**
- 2.1 Relevant equations and dimensionless numbers 9
- 2.2 Dipolar vortex models 11
  - 2.2.1 The Chaplygin-Lamb dipolar vortex 11
  - 2.2.2 The super-smooth dipolar vortex 12
  - 2.2.3 The point-dipolar vortex 14

3 Experimental and numerical methods **15**
- 3.1 Experimental setup 16
- 3.2 Experimental methods 19
  - 3.2.1 Experimental procedure 19
- 3.3 Numerical methods 20

4 Characterization of the electromagnetically forced dipolar vortex **23**
- 4.1 Important forcing parameters and vortex characteristics 23
- 4.2 General behaviour of the generated dipolar vortex 25
- 4.3 Comparison of the generated dipolar vortex with the super-smooth and Chaplygin-Lamb dipole 27
  - 4.3.1 Comparison of vorticity fields 27
  - 4.3.2 Comparison of vorticity cross-sections 32
  - 4.3.3 Comparison of vortex eccentricities ϵ 35
  - 4.3.4 Comparison of the ω-ψ scatter plots 39
  - 4.3.5 Summary of comparison 45

5 The dipolar vortex behaviour with varied forcing parameters 46
5.1 The effect of varied parameters I and B 47
5.2 The effect of varying t_f 49
5.3 The effect of varying d_e 50
5.4 The enstrophy decay time t_d 54
5.5 The effect of stronger forcing on the generated dipolar vortex. 60
5.6 The behaviour of the vortex size d_v with varied forcing parameters 62
5.7 Vortex core separation distance d_c as a function of time 66
5.7.1 The effect of varied parameters I, B and t_f on d_c . . . 69
5.7.2 The effect of varied parameters d_e on d_c 70
5.8 The propagation speed of the vortex centre v_c as a function of time 73
5.9 The ω-ψ scatter plots with varied forcing parameters 80
5.10 Asymmetry in coherence of the dipolar vortex cores 83
5.10.1 The effect of the electric potential switch 84
5.11 Numerical simulations with varied dimensionless numbers C and Re 86
5.11.1 The effect of varying C 89
5.11.2 The effect of varying Re 92

6 Electromagnetically forced dipolar vortex collisions 93
6.1 Head-on frontal dipolar vortex collision 94
6.2 Frontal dipolar vortex collision with offset 97
6.3 Oblique dipolar vortex collision 100
6.4 Dipolar vortex collision with a sharp-edged wall 103
6.5 Dipolar vortex collision with a sharp-edged gap in a simply connected domain 105

7 Vortex-shear interaction 107
7.1 Brief introduction 107
7.2 Experimental setup: Dipolar vortex and shear flow interaction 107
7.3 Perpendicular fluid injection 110
7.4 Oblique fluid injection 113
7.5 Applying the electromagnetic dipole generator in a shearing background flow 115
7.5.1 Parallel vortex-shear interaction 115

8 Conclusions 117

References 119

Chapter 1

Introduction

1.1 Vortices in geophysical flows

On Earth there are large-scale flows that occur naturally. These flows are referred to as geophysical flows which drive the fluid motion in the Earth's atmosphere and oceans. Consequently, geophysical flows affect the climate and weather. Therefore by having a better understanding of geophysical flows, weather and climate forecasts can be improved.

In geophysical flows, vortex structures play a significant role. A prime example is atmospheric blocking, where large-scale vortex patterns in the atmospheric pressure field are nearly stationary and can persist for several days or even weeks. Due to this blocking, the weather and climate remains unchanged for extended periods of time. An illustration of atmospheric blocking is shown in Figure 1.1a. In Figure 1.1a, the blocking high and low pressure system forms a dipolar vortex-like structure. The figure is sketching a situation where the structure is affecting and deflecting the Jet stream and the trajectory of a hurricane.

There are many different types of vortices. The two most elementary vortex structures are the monopolar vortex and dipolar vortex. The monopolar vortex is a single vortex whereas the dipolar vortex is a structure with two closely packed vortices with oppositely signed vorticity. Vorticity is a measure of rotation at a certain point, expressed in units of s^{-1}. The two poles of dipolar vortex interact with each other which results in a self-induced propagation. This effect is called self-propulsion. In addition to self-propulsion, dipolar vortices can trap particles inside and the combination gives rise to a naturally occurring transport mechanism. One example, are vortex struc-

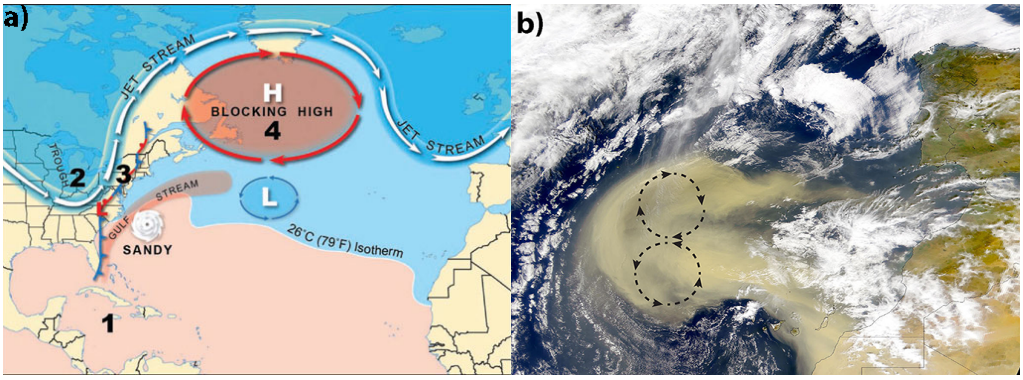

Figure 1.1: a) Figure showing an illustration of atmospheric blocking. The blocking high and low pressure system form a dipolar-vortex like structure that affects the weather and climate of the surrounding region. Image courtesy of T. Rabenhorst. b) Figure depicting the transportation of Sahara sand over the Atlantic Ocean by a vortex-like structure. Image taken from N. Kuring, SeaWiFS Project.

tures that trap sand from the Sahara desert and transports the sand over large distances. Figure 1.1b shows a satellite image of Sahara sand being transported over the Atlantic ocean by a dipolar vortex like structure.

1.2 Geophysical flows and quasi-2D flow conditions

An important feature of large-scale geophysical flows is that they are two-dimensional(2D) in good approximation or also known as quasi-2D(Q2D). This Q2D behaviour is due to the combination of the Earth's planetary background rotation, shallowness of the fluid layer and density stratification. The planetary background rotation is the first Q2D flow inducing factor. How background rotation induces Q2D flow is described by the Taylor-Proudman theorem [1][2].
The second factor, the shallow-layer approximation is considered valid as the Earth's atmosphere and oceans have a typical horizontal length scale that is significantly bigger than its typical vertical length scale.
The third factor is density stratification which suppresses vertical motion due to buoyancy forces.

1.3 The realization of Q2D conditions in the laboratory

Laboratory experiments involving Q2D vortices generally utilize a combination of shallow-layer, stratification and background rotation to promote Q2D conditions. This study focuses specifically on generating symmetric dipolar vortices that have a straight propagation trajectory. The experiments in this study are carried out in a shallow stratified fluid.

The use of background rotation is a method to achieve Q2D flow conditions. This was proven theoretically by Proudman [2] and studied experimentally by Taylor [1]. Comparatively, the shallow layer is not as effective when using background rotation. This is due to enhanced bottom friction effects which consequently result in a faster decay of generated dipoles. Experiments using background rotation typically have a larger fluid depth. Thus the bottom friction effects play a significantly smaller role and vortices in rotating fluid are relatively 'long-lived'.

In a study by Zavala et al. [3], non-linear Ekman effects influence dipolar vortices. The Ekman effect results in an asymmetry in decay rate between the cyclonic and anticyclonic parts of the dipole. The cyclonic direction shares the same rotational direction as the background rotation and vice versa for the anticyclonic direction. The asymmetry results in a deflected propagation trajectory in the anticyclonic direction. Background rotation is more effective for inducing Q2D condition but non-linear Ekman effects are a disadvantage when working with background rotation. Non-linear Ekman effects can be suppressed by increasing the magnitude of the background rotation. However, a faster rotating table can be relatively hazardous and technically difficult to build.

1.4 Dipolar vortex generation methods

Dipolar vortices are easily generated in shallow fluid layers by using any external forcing that induces linear momentum. One example of such an external forcing is an electromagnetical forcing. Notable studies on generating vortices electromagnetically are performed by Tabeling et al. [4] (array of monopolar vortices) and Honji & Haraguchi [5] (dipolar vortices). A sketch of the setup by Tabeling et al. is shown in Figure 1.2. In both studies the setup is similar but also in numerous other studies as this specific setup is commonly used. This type of setup consists of a rectangular container with electrodes positioned at opposite sides. While magnets are placed beneath the container.
An electric potential is applied over the two electrodes which generates an electric current running through the electrolytic fluid. The combination of the electric current and magnetic field generates a Lorentz force. In this type of method, the curl of the generated Lorentz force is non-zero which means that vorticity is generated, leading to a dipolar vortex.

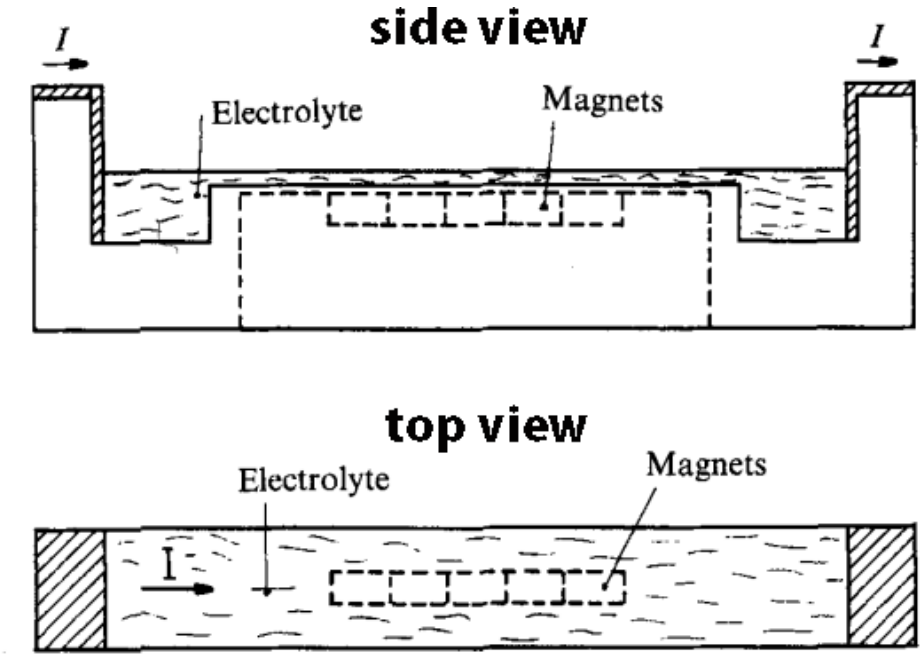

Figure 1.2: Figure showing an illustration of an alternative electromagnetical forcing mechanism used in the study performed by Tabeling et al. Image taken from Tabeling et al. [4].

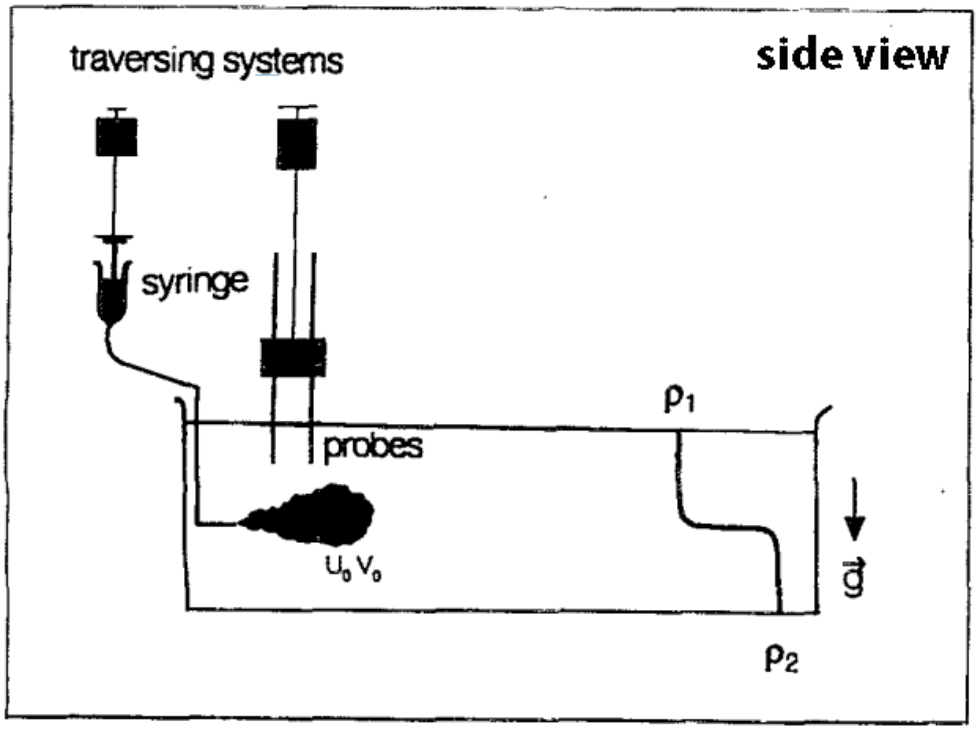

Figure 1.3: Figure showing an illustration of a syringe-type setup used in the study performed by Flór et al. Image taken from Flór et al. [6].

There are alternative forcing mechanisms besides electromagnetic forcing such as injections with pipettes/syringes in stratified fluid. The time evolution of the injected fluid by using pipettes/syringes has for example been documented in a study by Flór et al. [6] and by Flór & van Heijst [7].

The experimental setup used by Flór et al. consists of a syringe-type forcing mechanism as depicted in Figure 1.3. Flór et al. [6] made observations of the evolution of an isolated turbulent region in a two-layer stratified fluid. During the forcing a conical 3D turbulent region emerges. Subsequently, the vertical inertia becomes the same order as buoyancy forces. At this time the turbulent region reaches its maximum vertical size. Soon after the gravitational collapse starts to set in, which causes the structure to reduce in size. Afterwards, the structure transforms into a single sharp intrusion and a dipolar vortex structure emerges.
The syringe-type method generates a jet which is initially turbulent. This initial turbulent phase of the dipole results in relative unpredictable propagation trajectory and strength.

Flór et al. utilized a linearly stratified fluid, which has the advantage that the generated vortices are relatively long-lived. However, the preparation time for setting up this type of stratification can take up to one week, while the setup time for a two-layer stratification is generally in the order of ten minutes (used in the proposed method).

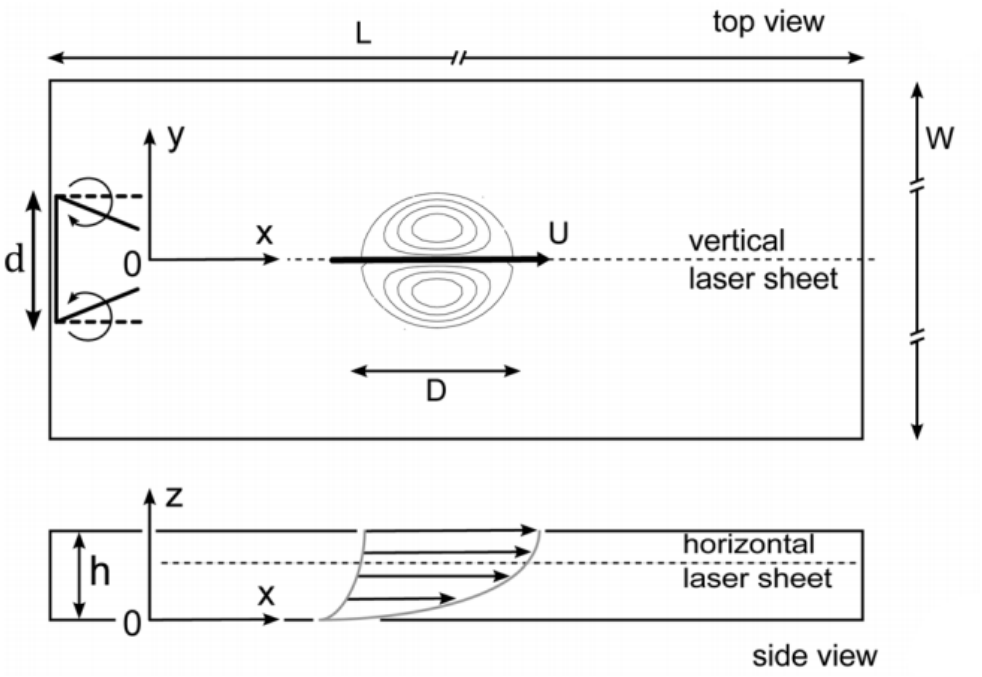

Figure 1.4: Figure showing an illustration of a mechanical flap mechanism used in the study performed by Albagnac et al. Image taken from Albagnac et al. [8].

Mechanical forcing mechanisms can also be used to generate dipoles instead of syringes and electromagnetic forcing mechanisms. To give an example: Albagnac et al. [8] used two mechanical flaps. An illustration of this experimental setup is shown in Figure 1.4. These mechanical flaps are relatively large in size, which can be relatively intrusive. The intrusiveness of large mechanical mechanisms is most notable during experiment with background flow.

For example, investigations on the interaction between vortices and shear flow as for example studied by Trieling et al. [9]. The no-slip condition imposed by the mechanical components submerged into the fluid blocks and perturbs the background flow.
Fernandes et al. [10] used a piston mechanism to study dipolar vortex-shear interaction. The mechanism is fixed at a position permanently and thus restricting to only generate dipoles at a single position. Furthermore, this mechanism can only generate dipoles propagating at a relatively small range of angle.

1.5 Study outline

The goal of this study is to investigate a new method of generating dipolar vortices in a shallow stratified fluid layer, considering a novel design of a dipolar vortex generator device, utilizing electromagnetic forcing.

The project has three parts: (i) to characterize the generated dipolar vortices, (ii) to apply the dipole generator in experiments. The latter part of the project is performed in order:

1. to show the enhanced control over propagation trajectories and vortex strength, compared to alternative methods. This is achieved by studying dipolar vortex collisions. Dipolar vortex collisions are sensitive to small offsets of propagation trajectories and strength. Thereby giving an indication if there is sufficient control.

2. To illustrate the compact design as a relative unintrusive forcing mechanism. This is achieved by generating dipolar vortices in a shearing background flow.

Furthermore, the new dipolar vortex generation method is investigated numerically through Comsol Multiphysics to complement experimental results.

Chapter 2

Theory

2.1 Relevant equations and dimensionless numbers

The equation governing the incompressible flow in a Newtonian fluid is given by the Navier-Stokes equation (NS) [11] which is the conservation of momentum:

$$\frac{\partial \bar{\mathbf{u}}}{\partial t} + (\bar{\mathbf{u}} \cdot \nabla)\bar{\mathbf{u}} = -\frac{\mathbf{1}}{\rho}\nabla \mathbf{P} + \nu \nabla^{\mathbf{2}} \bar{\mathbf{u}} + \frac{\mathbf{1}}{\rho}\bar{\mathbf{J}} \times \bar{\mathbf{B}} \tag{2.1}$$

with velocity $\bar{\mathbf{u}}$, the density ρ, the pressure P, the kinematic viscosity ν, the electric current density $\bar{\mathbf{J}}$ and the magnetic field $\bar{\mathbf{B}}$. Furthermore, considering incompressible fluids

$$\nabla \cdot \bar{\mathbf{u}} = \mathbf{0}. \tag{2.2}$$

Vorticity is an important parameter in studies considering vortices. Vorticity ω is defined as:

$$\bar{\omega} = \nabla \times \bar{\mathbf{u}}. \tag{2.3}$$

The vorticity equation is derived by taken the curl of the NS equation (equation (2.1)) as follows

$$\frac{\partial \bar{\omega}}{\partial t} + (\bar{\omega} \cdot \nabla)\bar{\omega} = \omega \cdot \nabla \bar{\mathbf{u}} - \omega \nabla \cdot \bar{\mathbf{u}} + \frac{\nabla \rho \times \nabla \mathbf{P}}{\rho^{\mathbf{2}}} + \nu \nabla^{\mathbf{2}} \bar{\omega} + \frac{\mathbf{1}}{\rho}\nabla \times (\bar{\mathbf{J}} \times \bar{\mathbf{B}}) \tag{2.4}$$

The Navier-Stokes equation can be non-dimensionalized for this specific flow system. This is done by using a typical length scale L, a typical time scale T, a initial current density J_0 and the magnetic field strength B_0. This will result in the non-dimensionalized Navier-Stokes equation:

$$\frac{\partial \bar{\mathbf{u}}^*}{\partial t^*} + (\bar{\mathbf{u}}^* \cdot \nabla^*)\bar{\mathbf{u}}^* = -\nabla^* P^* + \frac{\nu}{U_0 L}\nabla^{*2}\bar{\mathbf{u}}^* + \frac{J_0 B_0 L}{\rho {U_0}^2}(\bar{\mathbf{J}}^* \times \bar{\mathbf{B}}^*) \tag{2.5}$$

$$J_0 = \frac{I_0}{A(L)} \tag{2.6}$$

$$A(L) = HL_J \tag{2.7}$$

$$U_0 = \frac{L}{T} \tag{2.8}$$

J_0 can be expressed in terms of I_0 and a typical surface area $A(L)$ as expressed in equation (2.6), that depends on the typical electric current cross-sectional length scale L_J and H the typical fluid depth as described in equation (2.7). U_0 can be reformulated with the typical length scale L and the typical time scale T, as illustrated in equation (2.8).

The typical length scale L is defined as d_e the electrode gap distance as

$$L = d_e \tag{2.9}$$

and the typical time scale T is defined as t_f the forcing time duration as

$$T = t_f. \tag{2.10}$$

Then the substitution of equations (2.6), (2.7) and (2.8) into equation (2.5) will result in:

$$\frac{\partial \bar{\mathbf{u}}^*}{\partial t^*} + (\bar{\mathbf{u}}^* \cdot \nabla^*)\bar{\mathbf{u}}^* = -\nabla^* P^* + \frac{1}{Re}\nabla^{*2}\bar{\mathbf{u}}^* + C(\bar{\mathbf{J}}^* \times \bar{\mathbf{B}}^*) \tag{2.11}$$

Equation (2.11) has two non-dimensional numbers, the electromagnetic forcing coefficient C and the Reynolds number Re:

$$\mathrm{C} = \frac{I_0 B_0 t_f^2}{\rho H \alpha d_e^2} \tag{2.12}$$

$$\mathrm{Re} = \frac{d_e^2}{\nu t_f} \tag{2.13}$$

The coefficient $\alpha = 4.84$ in equation (2.12) is discussed later.

The dimensionless numbers C and Re are used in the non-dimensional NS equation and used as input parameters in numerical simulations. These numerical simulations model the generated dipoles by the proposed electromagnetic device. The numerical fluid simulation is strictly 2D but the flow in experiments are quasi-2D and will exhibit some 3D effects.

2.2 Dipolar vortex models

There have been numerous studies on analytical solutions of 2D vortex structures. For this study, there are three relevant analytical solutions. Namely, the Chaplygin [12]-Lamb [13] (circular) dipole, the super-smooth (elliptical) dipole and the point-dipolar vortex.

2.2.1 The Chaplygin-Lamb dipolar vortex

The most widely known theoretical dipolar vortex solution is the Chaplygin-Lamb(CL) dipole solution. The CL solution was first known as the Lamb-dipole but Meleshko and van Heijst [14] found out that this solution was found independently by Chaplygin (1899, 1903) and Lamb (1895, 1906).

The Chaplygin-Lamb (CL) dipole is an analytic solution considering the steady, inviscid, incompressible, 2D Euler equations where the dipolar vortex solution has a continuous vorticity distribution on a circular region. Stokes showed that any flow represented by the stream function $\psi(x, y)$ defined as:

$$u = \frac{\partial \psi}{\partial y}, v = -\frac{\partial \psi}{\partial x} \tag{2.14}$$

with u and v the velocity components in x and y-direction (Cartesian). Note that with $\bar{\omega} = \omega \bar{\mathbf{e}_\mathbf{z}}$, where $\omega = -\nabla^2 \psi$. Then this flow satisfies the equation:

$$\omega = \frac{\partial^2 \psi}{\partial x} + \frac{\partial^2 \psi}{\partial y} \tag{2.15}$$

with F an arbitrary function of ψ and if

$$F(\psi) = -k^2 \psi \tag{2.16}$$

where k is a constant(for coherent structures $F(\psi) = \omega(\psi)$). Then switching to 2D polar coordinates r and θ as follows

$$x = r\cos(\theta), y = r\sin(\theta) \tag{2.17}$$

the following equation is obtained

$$\frac{\partial^2 \psi}{\partial r^2} + \frac{1}{r}\frac{\partial^2 \psi}{\partial \theta^2} + k^2 \psi = 0. \tag{2.18}$$

Meleshko & van Heijst [14] solved equation (2.18) which then results in the CL-dipole solution for two regions. One region is the inside of the circular

domain (separatrix) with radius a and the other region is the outside of this circular domain:

$$\psi = CB_1(kr)\sin(\theta), r < a \tag{2.19}$$

$$\psi = U(r - \frac{a^2}{r})\sin(\theta), r > a \tag{2.20}$$

with B_1 a Bessel function (of the first kind).

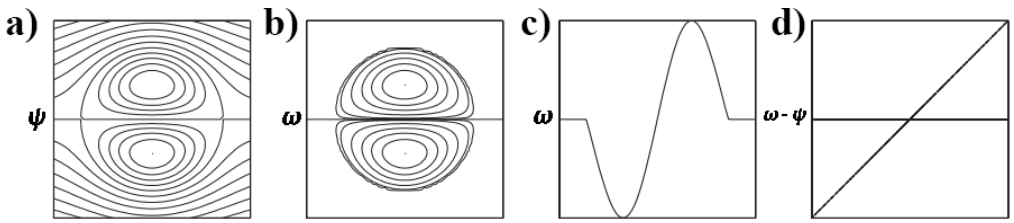

Figure 2.1: A figure showing the a) The iso-ψ lines, b) the vorticity distribution, c) the vorticity cross-section and d) the ω-ψ relation corresponding to the Chaplygin-Lamb dipolar vortex solution. Image taken from Kizner et al. [15]

Figure 2.1 illustrates the Chaplygin-Lamb dipole. In numerous experimental studies, dipoles have been observed that show close similarity with the theoretical Chaplygin-Lamb dipole solution.

2.2.2 The super-smooth dipolar vortex

Dipoles with elliptical boundaries represent a family of dipole solutions, with the CL-dipole being a particular case. A relevant dipolar vortex with such an elliptical boundary is the super-smooth (SS) dipolar vortex. The SS-dipole has been found and named by Kvholes & Kizner [15][16][17]. The name super-smooth was used as this dipole has a relatively smooth transition of vorticity at the vortex separatrix, in contrast to the Chaplygin-Lamb dipole.

The SS-dipole and CL-dipole have more differences besides the smooth transition of vorticity at the separatrix. One such difference is the separatrix eccentricity ϵ which is an important parameter for distinguishing different elliptical dipoles:

$$\epsilon = \frac{r_y}{r_x} \tag{2.21}$$

with r_x and r_y the minor and major axis of the elliptical boundary (separatrix), respectively. Kvholes & Kizner calculated that the eccentricity of the SS dipole $\epsilon = 1.162$.

Kvholes & Kizner [16] derived the SS-dipole using steady-state solutions of an ideal 2D Euler flow, similar to the derivation of the CL-dipole. However instead of using a circular separatrix they also enabled elliptical separatrices. Furthermore, instead of the linear relation (CL-dipole) shown in equation (2.16), they proposed a 7th order polynomial ω-ψ relation:

$$\omega = c_1\psi + c_3\psi^3 + c_5\psi^5 + c_7\psi^7 \tag{2.22}$$

They calculated the exterior solution $\psi'^{(ex)}$ analytically and subsequently used $\psi'^{(ex)}$ to obtain the interior solution $\psi'^{(in)}$ by adopting an iterative method and a polynomial approximation of $\psi'^{(in)}$ described in equation (2.22). The 7th order polynomial approximation was used by Kizner et al. for studying elliptical dipolar vortices, however the SS-dipole is approximated with only the 3rd order($\omega = c_3\psi^3$).

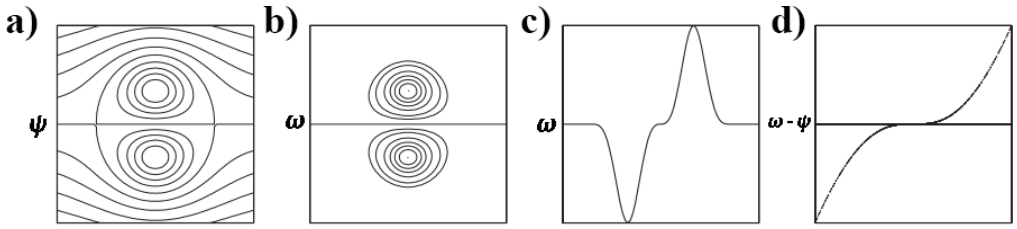

Figure 2.2: A figure showing the a) The iso-ψ lines, b) the vorticity distribution, c) the vorticity cross-section and d) the ω-ψ relation corresponding to the super-smooth dipolar vortex solution. Image taken from Kizner et al. [15]

Figure 2.2 illustrates the super-smooth dipole. Kizner et al. [15] numerically compared the evolution of symmetric 2D dipolar structures of three different types: the squeezed dipole, the CL-dipole and the SS-dipole.

Furthermore, Trieling et al. [18] considered barotropic elliptical dipoles experimentally in a rotating fluid. The dipolar vortices in the experiment matched the SS-dipole better than the CL-dipole solution.

2.2.3 The point-dipolar vortex

The point-dipolar vortex (PD) is set of two closely packed point vortices, which is based on potential theory. The point vortex has a singular vorticity distribution described by a Dirac-delta function in 2D polar coordinates as:

$$\omega(r) = \gamma\delta(r) \tag{2.23}$$

with γ the strength of the point vortex. The azimuthal flow induced by the point vortex is irrotational and described by:

$$v_\theta(r) = \frac{\gamma}{2\pi r}. \tag{2.24}$$

The point-vortex can never be observed experimentally but PD-like dipoles with two closely packed concentrated vorticity patches are relevant which are a kind of in between a PD and SS-dipole.

Chapter 3

Experimental and numerical methods

3.1 Experimental setup

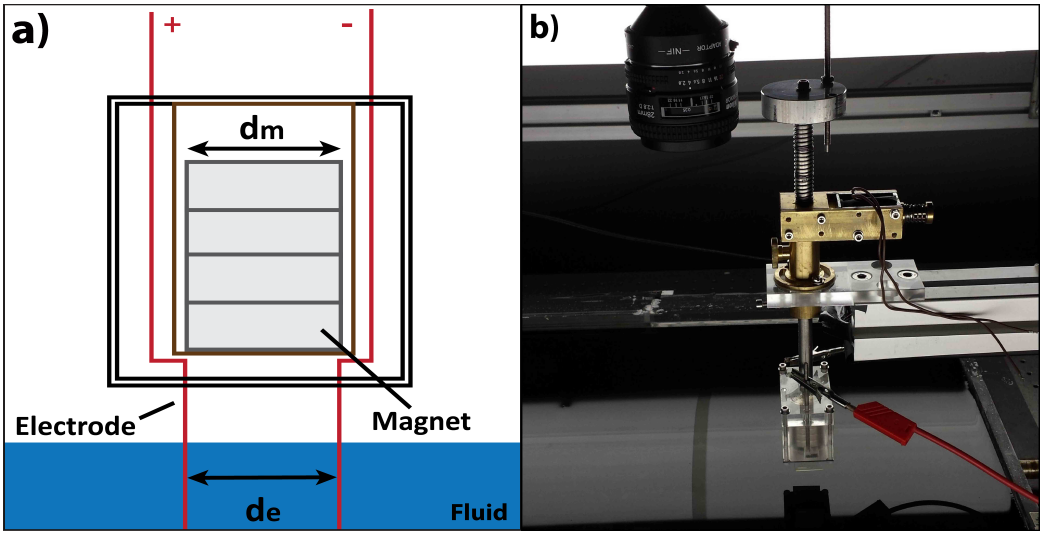

Figure 3.1: a) A sketch showing the front-view of the electromagnetic generator. The red lines indicate the two electrodes, while the gray rectangles illustrate the individual permanent magnets. The electrode gap distance is d_e and the magnet size is indicated with d_m. b) A photograph showing the side-view of the electromagnetic generator, the small transparent casing is visible at the bottom of the image where two power cables are connected to the electrodes. The four magnets residing in the transparent casing are also visible.

The electromagnetic dipole generator is illustrated in Figure 3.1. Figure 3.1a shows a sketch of the front-view and Figure 3.1b depicts a photograph of the generator. The perspex casing contains platinum coated electrodes that are passing through the casing. The platinum coating is used to minimize oxidation and other chemical reactions. Additionally, the electrodes are insulated to prevent any electrical interaction with surrounding components. The electrodes are connected to an external power source. When the electrodes are (partially) submerged into an electrolytic fluid, a current can be driven through the fluid.

Figure 3.1 shows another important component: the cylindrically shaped magnet. The magnet is not a single magnet but a combination of smaller magnets stacked together with identical diameter d_m of 2.5 cm. The center of each magnet coincides with the center of the casing and the electrodes are placed in symmetric fashion. The combined effect of driving current through a fluid and the magnetic field induces a Lorentz force. The Lorentz force is a volume force acting on the fluid, which can generate a dipolar vortex.

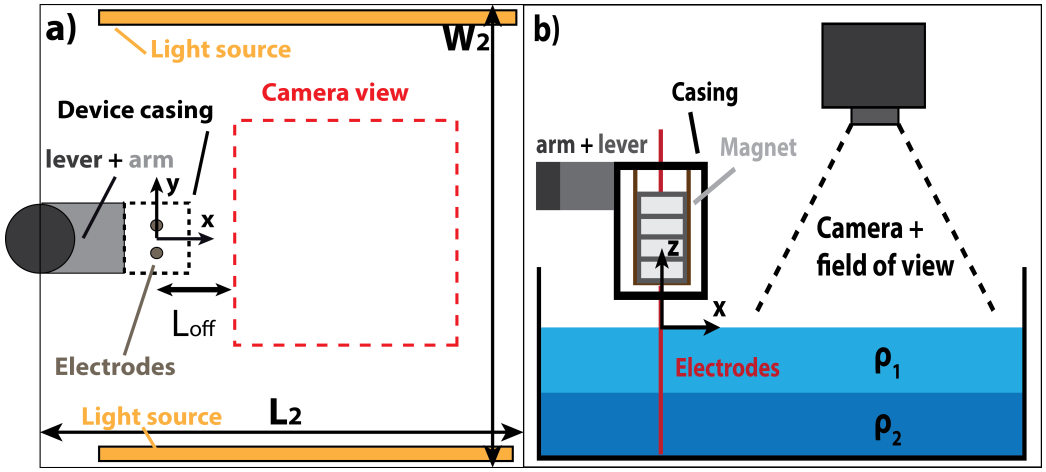

Figure 3.2: a) Top-view of the experimental setup. The casing around the magnets is depicted with a dashed black lines, the camera field of view is indicated with dashed red lines and the electrode pair is depicted as two gray circles. The length of the fluid tank L_2 and the width W_2 are also illustrated. $L_{off} = 7$ cm which is the offset between the electrodes and the field of view. The x and y-axes are also indicated, with $x = 0$ and $y = 0$ at the center of the magnet(during forcing). b) Side-view of the experimental setup showing the stratification with lower density ρ_1 and higher density ρ_2. The dashed black lines indicate the camera field of view. The device with electrodes, magnets, casing, arm and lever are also sketched. The x and z-axes are also indicated, with $z = 0$ at the water and air interface (the free surface).

Figure 3.2a,b shows a sketch of the top-view and side-view of the experimental setup, respectively. Figure 3.2a illustrates the dipole generator and a water tank with: length $L_2 = 52$ cm, width $W_2 = 52$ cm and depth $H_2 = 2$ cm. The fluid in the tank has a depth H of 0.8 cm. In addition, the fluid has two layers of salt solution (electrolytic) with different salt concentration, sketched in Figure 3.2b. The upper layer has a lower density salt solution than that of the bottom layer. The upper layer thickness is approximately 0.4 cm and the bottom layer 0.4 cm. The upper layer has a density ρ_1 of 1.03 kg/L and the lower layer has a density ρ_2 of 1.15 kg/L. The two-layer stratification is to reduce bottom friction effects. In the top-view sketch, L_{off} is shown which is the offset between position of the electrodes and the camera field of view with $L_{off} = 7$ cm.
Figure 3.2 also indicates the x,y and z-axes. The x = 0 and y = 0 is defined as the center of the magnet (during forcing). The z = 0 as defined as the interface of the water and air interface (the free-surface).

The vortex dipole generator is positioned above the tank at a certain position. Subsequently, the generator and it's electrodes are lowered and fixed at this position by an electrical clamping system. When lowered, the two electrodes submerge into the fluid. A Kepco power source that supplies the current I during forcing.

After forcing, the clamping mechanism releases and the generator and electrodes retract back to the original position. This setup is used during the study of the characterization of the generated dipolar vortex. For the dipole collisions, the same setup is used but with the addition of another generator. The experimental setup used for generating vortices in a shearing background flow is different and is discussed later.

3.2 Experimental methods

In this study, dye is used to visualize the flow and the structure of dipolar vortices. To obtain quantitative data, particle image velocimetry (PIV) is used. In PIV, tracer particles are used to visualize the flow. The tracer particles in the fluid are then illuminated by a light source (Fluorescent light tubes). The fluid flow is recorded with a camera and these images are then processed with PIV software (PIVtec). Properties of the flow can be extracted by correlating 'image pairs' taken consecutively with a very short time interval. The extracted flow properties from PIV are for example, the velocity and the vorticity field. The obtained velocity and vorticity field are then smoothed with a Gaussian filter and plotted with software (MATLAB).

3.2.1 Experimental procedure

The first step is to fill the tank with fluid of higher density ρ_2. Afterwards the lower density fluid with the particles is added into the tank.
Poly-amid particles are mixed into the fluid with the lower density ρ_1 with a diameter of 20 μm or 50 μm. In addition to the poly-amid particles, a surfactant solution is added. Surfactants reduce the surface tension and keeps the tracer particles from clumping at the free surface. The mixing of particles into fluid, instead of adding them afterwards, reduces their reflectivity but significantly reduces the 'particle clumping'. Particle clumping inhibits particles to follow the fluid motion adequately.

To get reliable data from PIV measurements, there should be an adequate amount of particles in the PIV 'investigation area'. The 'investigation area' is in this case the camera field of view, which is divided into tiny 'interrogation' areas. As a rule of thumb, there should be 6-10 particles in each 'interrogation area'. This has been confirmed by manually analyzing captured camera images before PIV processing starts.

3.3 Numerical methods

The numerical simulations are performed using Comsol Multiphysics, a direct numerical simulation (DNS) and finite element method. In order to model the experiments, three models are used in Comsol:

1. the 2D electric model, to obtain the current density field $J(x, y)$
2. the 3D magnetic field model, to obtain the magnetic field $B(x, y, z)$
3. the (laminar) 2D fluid model, the actual model that represents the experimental setup. where data from the electric and magnetic model are imported into to model the Lorentz Force $J(x, y) \times B(x, y, z = 0)$.

The electric and fluid model are both strictly 2D. The magnetic field model is 3D but a 2D slice is taken at $z = 0$ which is the vertical position at the air and water interface(free-surface) and the magnetic is at position $z = 5$ cm, see Figure 3.2b. The Lorentz Force $J(x, y) \times B(x, y, z = 0)$ is pulsed using a smoothed rectangular function for a duration corresponding to a typical forcing time in experiments. In all three models, the length is non-dimensionalized in d_e and the time in t_f.
Figures 3.3 and 3.4a,b show the numerically obtained magnetic field B_z, electric current density J_x and J_y, respectively.

The 2D fluid model has four no-slip boundaries that act as the fluid tank walls. The fluid model itself has approximately half a million mesh elements. These are distributed with a significantly higher concentration in the close vicinity of the electrodes, where the vorticity is generated(dipole formation region). From the formation region into the propagation direction of the dipole there is also a higher concentration of mesh elements.

Two numerical fluid simulation methods were used to model the experimental generation method. In experiments, the electrodes are submerged during the forcing but after forcing these are retracted out of the fluid. Therefore two fluid models are used.
The first model simulating the forcing, with no slip electrodes. At the end of the forcing, the velocity field is exported to the second model.
The second model uses the velocity field as initialization. The electrodes are not present to model the retraction of the electrodes after forcing. The space previously occupied by the electrodes is replaces with fluid having initial values with zero velocity.

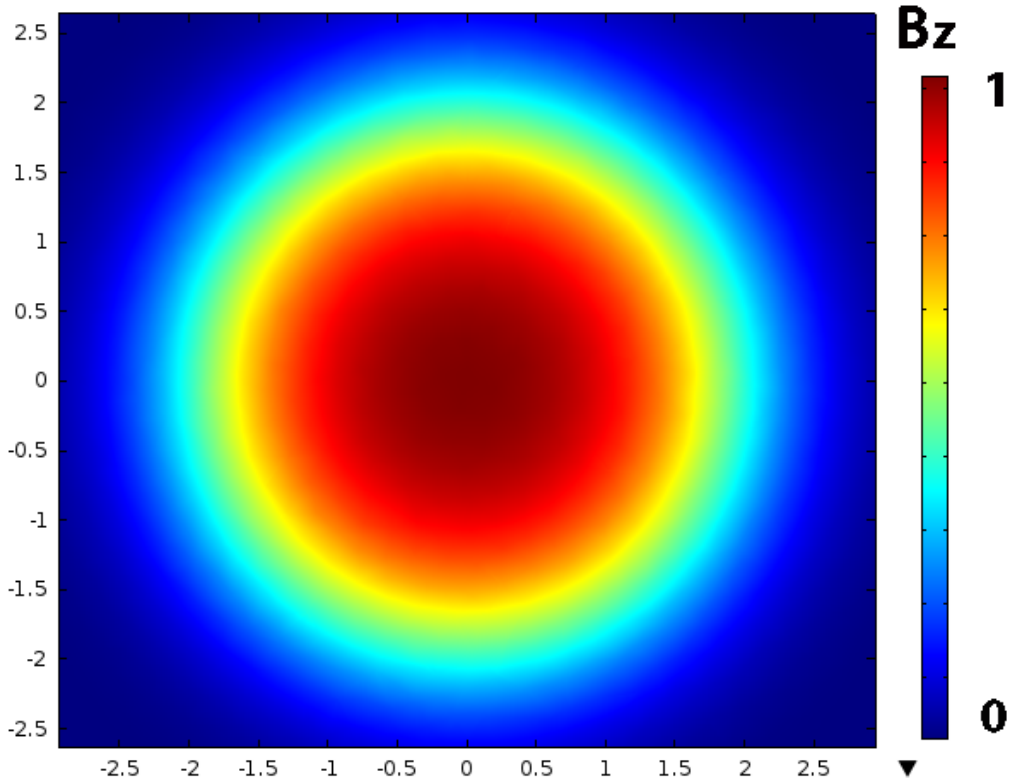

Figure 3.3: Figure showing a snapshot of a typical numerically obtained z-component of the magnetic field B_z, normalized with B_0.

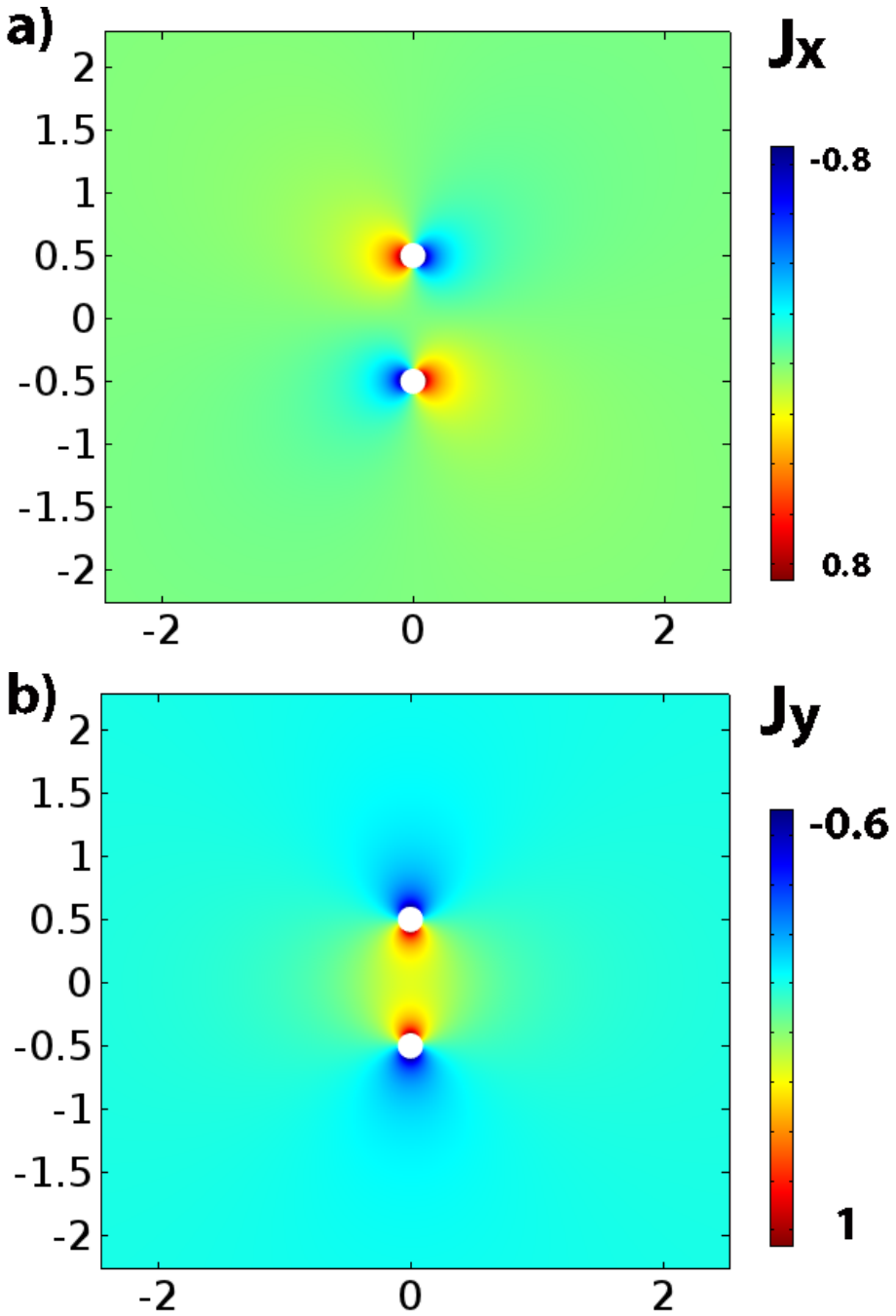

Figure 3.4: Figure showing a snapshot of a typical numerically obtained electric current density J normalized with J_0. The a) the x component J_x and b) the y component J_y. The J_0 is defined as J_{ymax} which is larger than J_{xmax} which results in the displayed values for J_{xmax} as 0.8 instead of 1.

Chapter 4

Characterization of the electromagnetically forced dipolar vortex

4.1 Important forcing parameters and vortex characteristics

The first goal is to characterize the generated dipolar vortices. The important parameters for the generation and evolution for the dipolar vortex are:

1. the electric current strength I
2. the strength of the magnetic field B
3. the forcing time t_f
4. the electrode gap distance d_e

The (dynamical) characteristics of the vortex and the dependence on the various forcing parameters is investigated by varying one specific (forcing) parameters while keeping the other parameters constant.
Vortex characteristics such as the velocity field of the vortex structure are studied by implementing PIV. From the velocity field of the dipolar vortex and the surrounding ambient fluid, relevant properties can be investigated. These properties include the vorticity field and the vorticity cross-section through the vortex cores. A vortex core corresponds to the vorticity center of magnitude from one of the individual vorticity patches. The center of vorticity intensity is analogous to the center of mass principle but instead of mass density, the vorticity magnitude is utilized. Other quantities are the

propagation velocity of the dipolar vortex center v_c, the separation distance between the vortex cores d_c and the $\omega - \psi$ relation of the dipolar structure.

Table 4.1 shows the values of the forcing parameters used in each individual experiment. These values are used to calculate the dimensionless numbers C and Re, which are used as input parameters for the numerical simulations.

I_0 (A)	B_0 (T)	d_e (cm)	Forcing time t_f (s)	C	Re
1.0	0.25	2.5	0.4	7.0	1560
1.0	0.50	2.5	0.4	14	1560
0.4	0.50	2.5	0.5	8.7	1250
1.0	0.50	2.5	0.5	22	1250
0.6	0.50	1.0	0.5	82	200
0.6	0.50	2.5	0.5	13	1250
1.0	0.50	2.5	0.4	14	1560
1.0	0.50	2.5	1.0	87	625

Table 4.1: Table giving an overview of the experimental forcing parameters with the corresponding electromagnetic forcing coefficient and Reynolds number.

4.2 General behaviour of the generated dipolar vortex

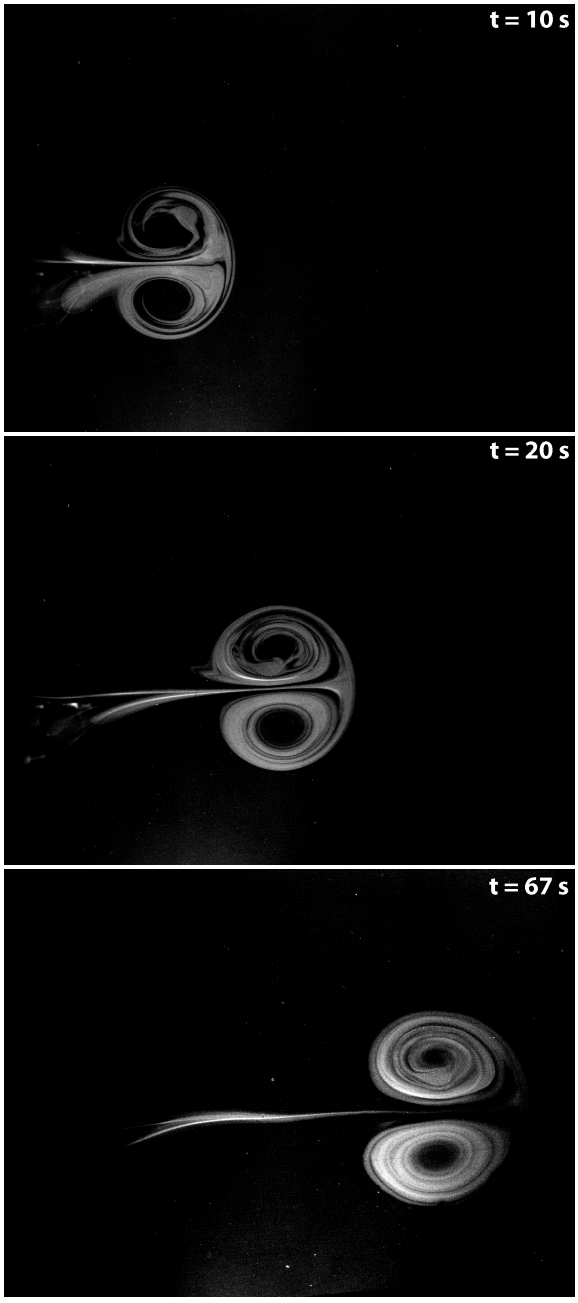

Figure 4.1: Set of snapshots showing the time evolution of a vortex dipole generated through electromagnetic forcing and visualized with dye.

The general behaviour of the generated dipolar vortices is studied. One set of forcing parameters with typical values has been considered, which is: $I = 1.0$ A, $B = 0.51$ T, $t_f = 0.4$ s and $d_e = 2.5$ cm. Figure 4.1 shows the qualitative behaviour of a generated vortex propagating through a shallow stratified fluid-layer and is being visualized using fluorescent dye (Fluorescein). Data from PIV measurements is presented in order to attain a quantitative characterization of the flow using the following properties:

1. the vorticity field ω
2. the vorticity cross-section
3. the vortex eccentricity ϵ
4. the $\omega - \psi$ relation

Figure 4.2 shows three experimentally obtained snapshots illustrating the time evolution of the vorticity field taken at t =14 s, 24 s and 34 s, respectively. Note that the camera field of view is positioned 7 cm away from the dipole formation region.

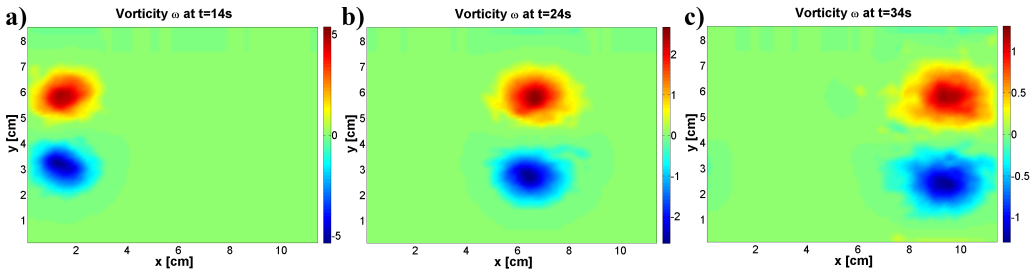

Figure 4.2: A figure showing three experimentally obtained snapshots of the experimentally obtained time evolution of the vorticity field with typical forcing parameters: $I = 1.0$ A, $B = 0.51$ T, $t_f = 0.4$ s and $d_e = 2.5$ cm. The colour-bar indicates the value of the vorticity ω.

4.3 Comparison of the generated dipolar vortex with the super-smooth and Chaplygin-Lamb dipole

4.3.1 Comparison of vorticity fields

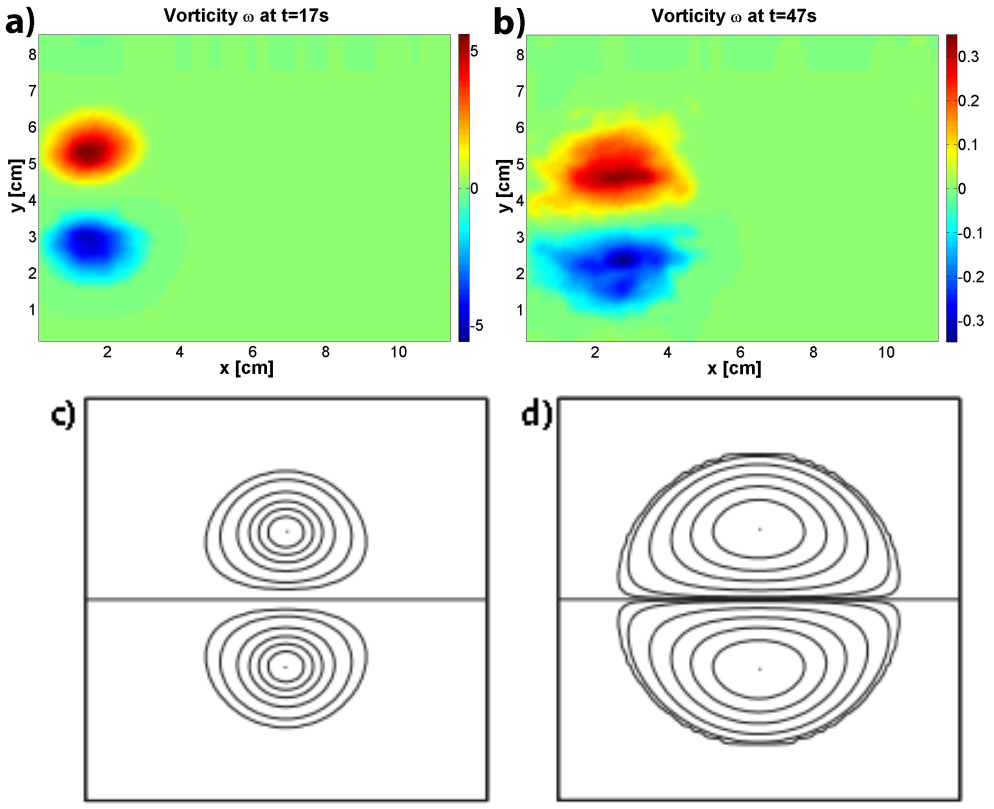

Figure 4.3: Experimentally obtained vorticity fields at a) an early time stage and b) later time stage. The colour-bar indicates the value of the vorticity ω. The vorticity (field) visualized with iso-lines of c) the SS-dipole and d) the CL-dipole. c),d): image courtesy of Kizner et al. [15].

The early propagation stage is shown in Figure 4.3a. This experimentally obtained snapshot shows a vorticity field with two slightly separated and circular vorticity patches of oppositely signed vorticity. This shows similarity with the vorticity field of the SS-dipole depicted in Figure 4.3c.
The later propagation stage illustrated by Figure 4.3b shows a dipole consisting of two semi-circular vorticity patches. This shows similarity with the CL-dipole illustrated in Figure 4.3d.

In numerically obtained figures, the vorticity is normalized with the maximum vorticity ω^* found in that specific snapshot and is defined as:

$$\omega^* = \frac{\omega}{\omega_{max}} \tag{4.1}$$

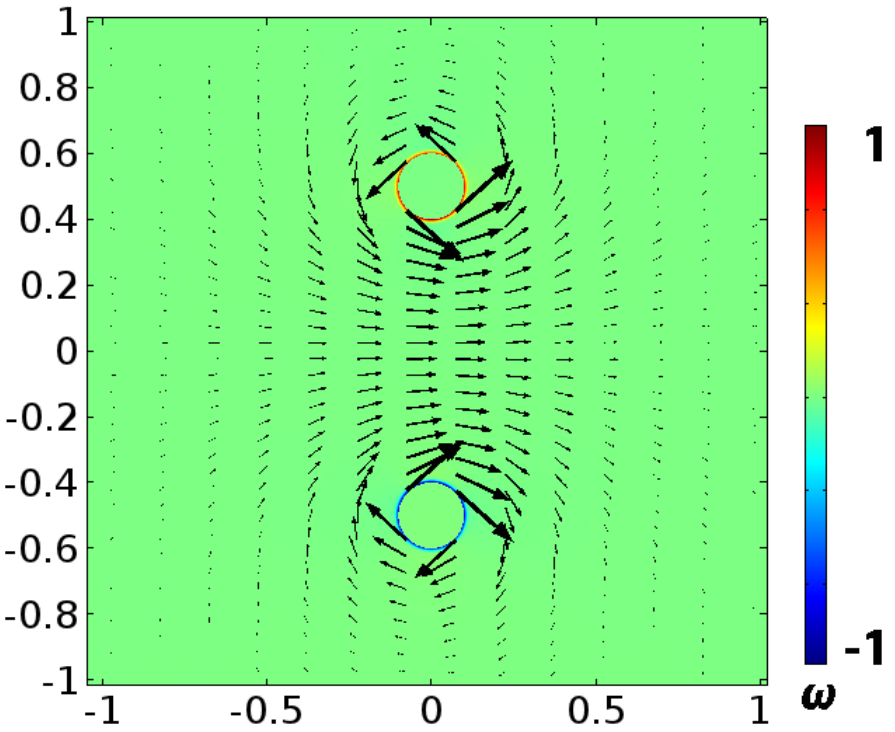

Figure 4.4: Numerically obtained vorticity field indicated with a colour bar and the volume force indicated with black arrows. The volume force and resulting vorticity field indicate that this method of generating dipoles initializes a point-dipole-like structure. The snapshot is taken at $t = 0.2\ t_f$ (after forcing). The vorticity is normalized with ω_{max} found in that snapshot.

The induced Lorentz volume force is investigated numerically. The typical volume force is shown in Figure 4.4, where the volume force is indicated with black arrows with the size indicating the magnitude and the generated vorticity is indicated with a colour bar. The snapshot is taken at $t = 0.1\ t_f$.

The vorticity equation describes the generation of vorticity shown in equation (2.4). In the previous electromagnetic generation methods, the vorticity is generated by the Lorentz volume force i.e. $\nabla \times (J \times B) \neq 0$, with current density distribution $\bar{J}_{other} = J_0 \bar{e_x}$.

The novel generation method has a different J distribution which is similar as shown in Figure 3.4. The $\nabla \times (J \times B)$ was calculated analytically in a simplified case. The simplified case considered a single electrode in a fluid with an electric potential relative to infinity. The J in polar coordinates then has a profile with $\bar{J} = \frac{J_0}{r}$. From this J, the resulting $\nabla \times (J \times B) = 0$.

Therefore, the novel method induces a Lorentz force that plays a lesser role in generating vorticity. The vorticity is instead generated by the electrodes imposing the no-slip condition. As a result, a PD-like structure emerges with the novel generation method whereas this is not the case with previous electromagnetic generation methods.

This can explain the experimentally observed relatively short 3D turbulent formation stage and thus relatively fast transition into a more laminar Q2D flow. Consequently, the novel method generates symmetric dipoles with improved control and predictability of the propagation trajectory.

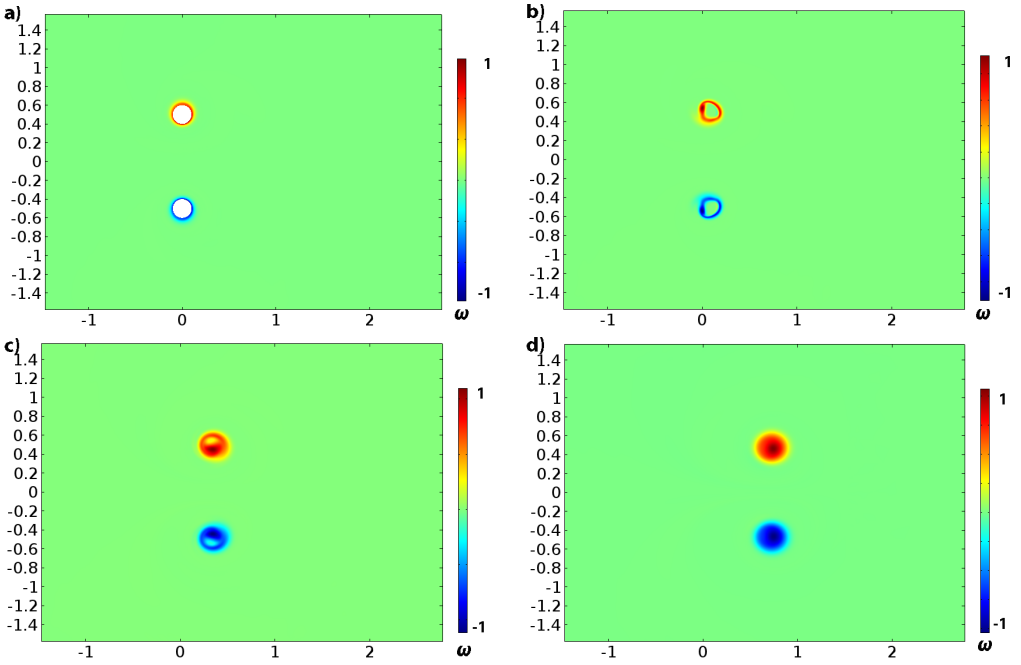

Figure 4.5: Figure showing a numerically obtained time evolution of the vorticity field during the formation phase: a) the vorticity field just after the forcing duration t_f ends. A ring of vorticity is visible around the no-slip electrodes, b) the vorticity field 0.1 t_f after forcing, initialized with the velocity field of a) showing the ring of vorticity without the electrodes, c) the vorticity field 0.5 t_f after forcing showing that the vorticity ring is deforming and d) the vorticity field 1.0 t_f after forcing, showing that the vorticity ring deformed to a PD-like structure. With $C = 7$ and $Re = 1560$ which corresponds to the experiment shown in Figure 4.3. The vorticity in each snapshot is normalized with the ω_{max} in that specific snapshot.

The formation phase is investigated which is the phase just after forcing. Figure 4.5 shows numerically obtained snapshots of the vorticity field during, a) t = 0 after forcing(first model with no-slip electrodes), b) t = 0.1 t_f after forcing where two rings of oppositely signed vorticity are visible(second model without no-slip electrodes), c) t = 0.5 t_f after forcing where the two vorticity rings are deformed significantly and d) t = 1.0 t_f after forcing where a PD-like structure emerges, respectively.

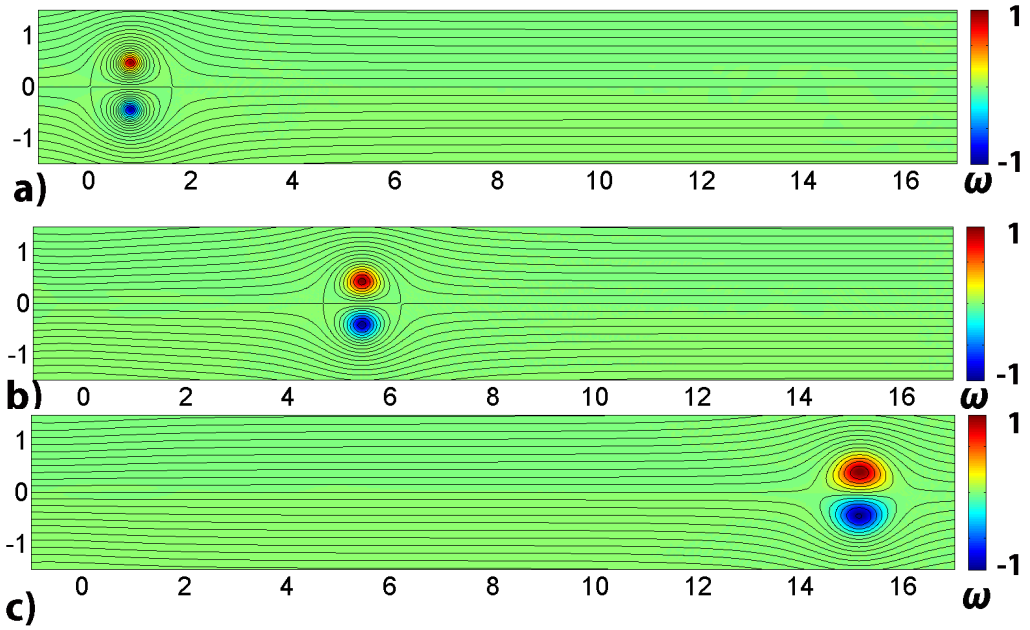

Figure 4.6: Figure showing numerically obtained time evolution of the vorticity and stream-function field. a) The vorticity and stream-function field during forcing showing a PD-like structure, b) the vorticity and stream-function field at a early propagation stage showing a SS-dipole-like structure and c) the vorticity and stream-function field at a later stage showing a transition into a more CL-dipole-like structure. With C = 7 and Re = 1560, which corresponds to the experiment shown in Figure 4.3. The vorticity in each snapshot is normalized with the ω_{max} in that specific snapshot.

The time evolution of the vorticity field is also numerically investigated in a larger time interval. Figure 4.6a,b,c shows the vorticity and stream-function field field right after formation, early and later stage of the propagation, respectively.
Figure 4.6a shows a more PD-like structure. Figure 4.6b shows a SS-dipole-like structure and Figure 4.6c shows a CL-dipole-like structure.
The dimensionless numbers are C = 7 and Re = 1560, corresponding to the first experiment listed in Table 4.1.

4.3.2 Comparison of vorticity cross-sections

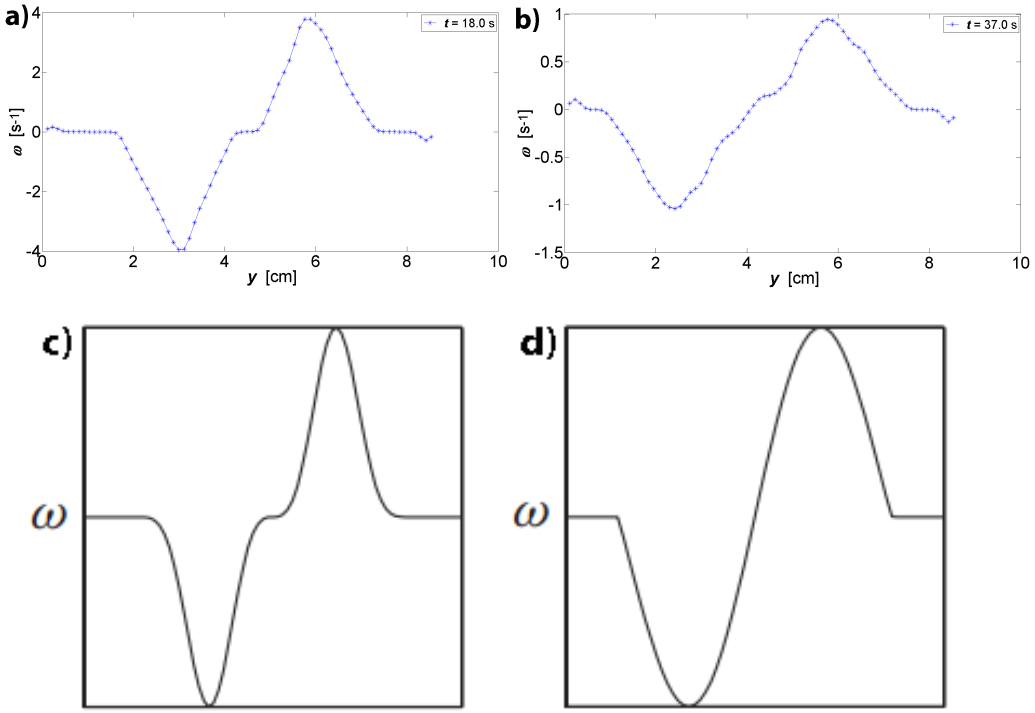

Figure 4.7: Experimentally obtained vorticity cross-sections at a) an early time step and b) a later time step. Experimental forcing parameters I = 1.0 A, B = 0.51 T, t_f = 0.4 s and d_e = 2.5 cm. c) and d) show the vorticity cross-section of the SS and CL-dipole, respectively. c),d): image taken from Kizner et al. [15].

The vorticity cross-section is defined as the intersecting line of the two centers of positive and negative vorticity. Figure 4.7a,b show experimentally obtained vorticity cross-sections at an early and later time step, respectively. Figure 4.7c,d show the vorticity cross-sections of the SS and CL-dipole, respectively.

In some cross-sections a 'vorticity plateau' is visible, this is defined as a relatively large region with zero or close to zero vorticity. The vorticity cross-sections of PD-like and SS-dipoles have a plateau.
In Figure 4.7a,c it is visible that the cross-section at an early time stage (experimental) is similar to the SS-dipole. In Figure 4.7b,d it is visible that at a later time stage the vorticity plateau has reduced in size significantly, similar to the CL-dipole.

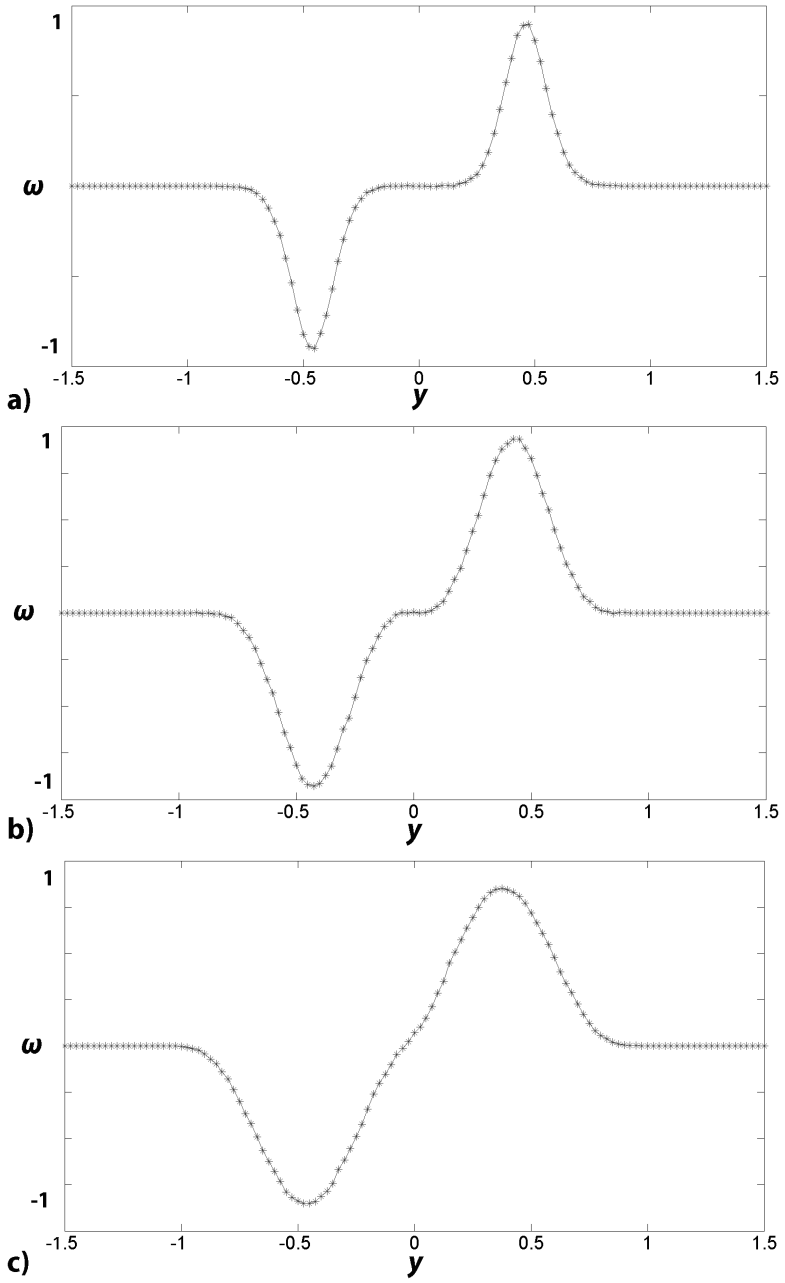

Figure 4.8: Figure showing numerically obtained time evolution of the vorticity cross-section: a) the vorticity cross-section field during forcing showing a PD-like structure, b) the ω cross-section at a early propagation stage showing a SS-dipole-like structure c) the vorticity cross-section at a later stage showing a transition into a more CL-dipole-like structure. With $C = 7$ and $Re = 1560$ which corresponds to the experiment shown in Figure 4.3. The vorticity in each snapshot is normalized with the ω_{max} in that specific snapshot.

Figure 4.8 shows three vorticity cross-sections at different times which are obtained numerically from the same simulation and time-steps/snapshots as Figure 4.6.
Figure 4.8a,b,c shows the ω cross-section just after formation, the early and later propagation stage, respectively. The three snapshots in Figure 4.8a,b,c show similarities with the PD, SS-dipole and CL-dipole respectively. The vorticity plateau is relatively large just after formation and subsequently reduces in size significantly at the later stages.

4.3.3 Comparison of vortex eccentricities ϵ

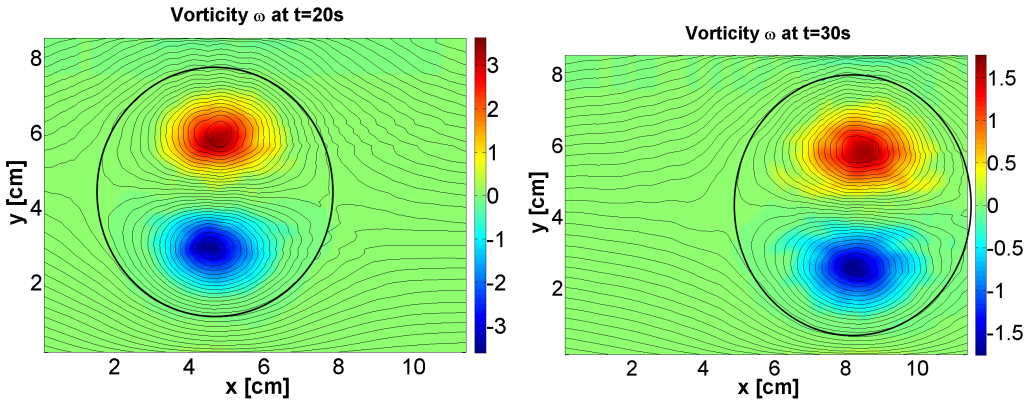

Figure 4.9: Figure illustrating the experimentally obtained vorticity distribution, corresponding stream function iso-lines in the co-moving frame and the manually computed approximation of the separatrix indicated by the black ellipse. a) $\epsilon = 1.06$ b) $\epsilon = 1.10$. The forcing parameters are: $I = 1.0$ A, $d_e = 2.5$ cm, $t_f = 0.5$ s and $B = 0.51$ T.

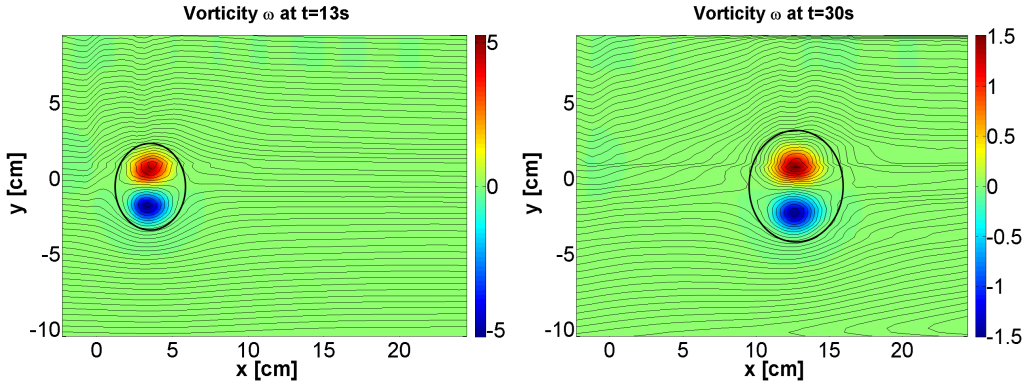

Figure 4.10: Figure illustrating the experimentally obtained vorticity distribution and corresponding streamfunction iso-lines in the co-moving frame with forcing parameters: $I = 1.0$ A, $d_e = 2.5$ cm, $t_f = 0.5$ s and $B = 0.51$ T. The black ellipse approximates the vortex separatrix.a)$\epsilon = 1.24$, b) $\epsilon = 1.15$.

Another important parameter is the vortex separatrix eccentricity ϵ. The ϵ is defined as the ratio between the axis length perpendicular to the propagation direction and the axis length parallel to the propagation direction. The eccentricity of the SS-dipole has value of $\epsilon = 1.162$, while the CL-dipole has an eccentricity of 1.

The vortex separatrix is computed by utilizing PIV data. First ψ is calculated by integrating the velocity field numerically in a co-moving frame. The co-moving frame 'speed' is computed using the velocity of the dipole center. This is done by calculating the average velocity of the dipole center in a time interval of $\delta t = 1$ s around the specific snapshot. Subsequently, the black elliptical line indicates the manually computed separatrix.

In Figure 4.9 and 4.10, the vortex separatrix eccentricity has been computed for two different experimental measurements. The separatrices are constructed manually using the ψ-function. However, small deviations can result in significant deviations of ϵ values with this method of computing the separatrix. This is due to estimating the separatrix by using the iso-ψ lines as they are not well-defined enough for accurate ϵ measurements.
The calculated values for ϵ range from 1.06 to 1.24. These ϵ values are larger than the value of 1 which is the value for the Chaplygin-Lamb dipole.

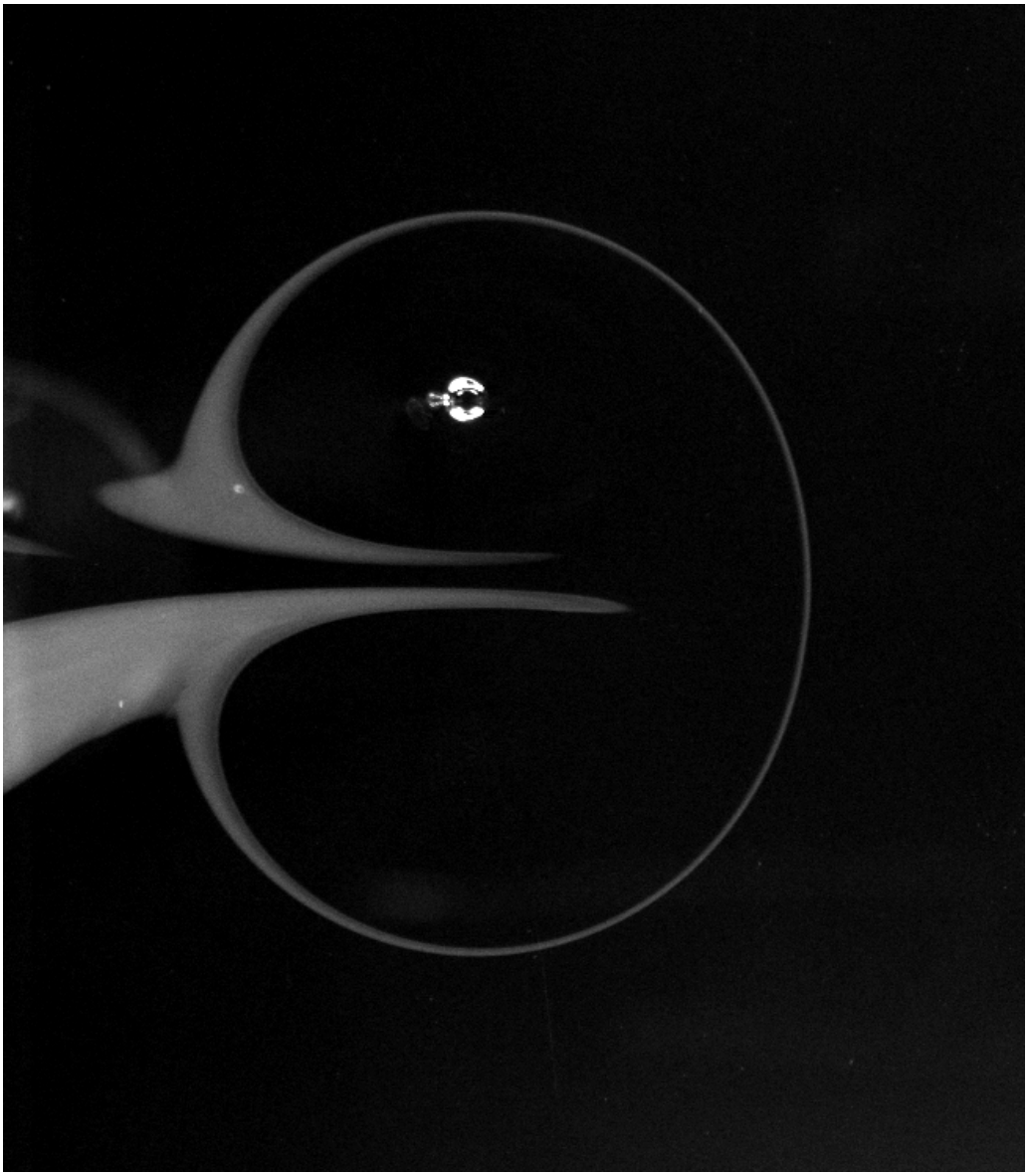

Figure 4.11: Figure illustrating an experiment using dye visualization where the vortex separatrix is made visible. The calculated eccentricity: $\epsilon = 1.16$ *which matches the value* $\epsilon = 1.162$ *of the super-smooth dipole sufficiently*

The ϵ is computed more accurately with an alternative method is using an experiment with dye visualization as shown in Figure 4.11. The eccentricity is derived from Figure 4.11 with a value of $\epsilon = 1.16$ which matches the SS-dipole value $\epsilon = 1.162$ sufficiently.

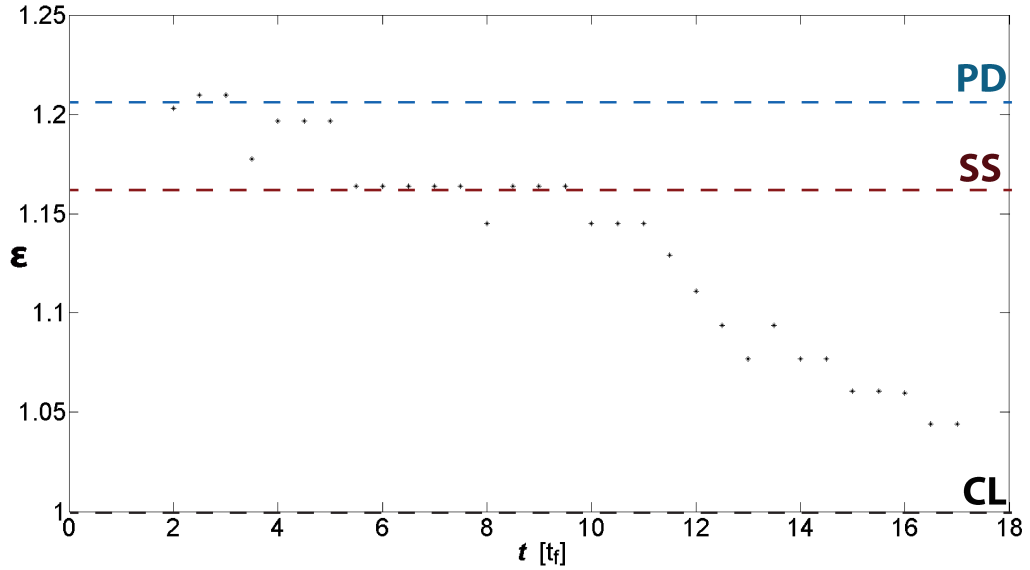

Figure 4.12: Figure showing a numerically obtained time evolution of the eccentricity ϵ. The dashed lines: blue represents the PD predicted value $\epsilon = 1.21$, red represents the SS-dipole predicted value $\epsilon = 1.16$ and black represents the CL-dipole predicted value $\epsilon = 1$.

The estimation of ϵ from experimental data can be difficult, therefore ϵ is also estimated numerically. The numerically obtained values of ϵ are plotted versus the time (in t_f) shown in Figure 4.12. In this Figure three dashed lines are visible. The blue, red and black dashed lines correspond to the PD, SS and CL-dipole predicted values for ϵ, respectively.

The $\epsilon(t_f)$ found for the (numerically) generated dipole again show the same trend. First the dipole is PD-like, subsequently an intermediate structure similar to the SS-dipole and then transitions into a CL-dipole-like structure later on.
Notable in Figure 4.12 is the 'plateau' where the dipole holds the SS-dipole eccentricity of 1.16 for a relatively long time.

4.3.4 Comparison of the ω-ψ scatter plots

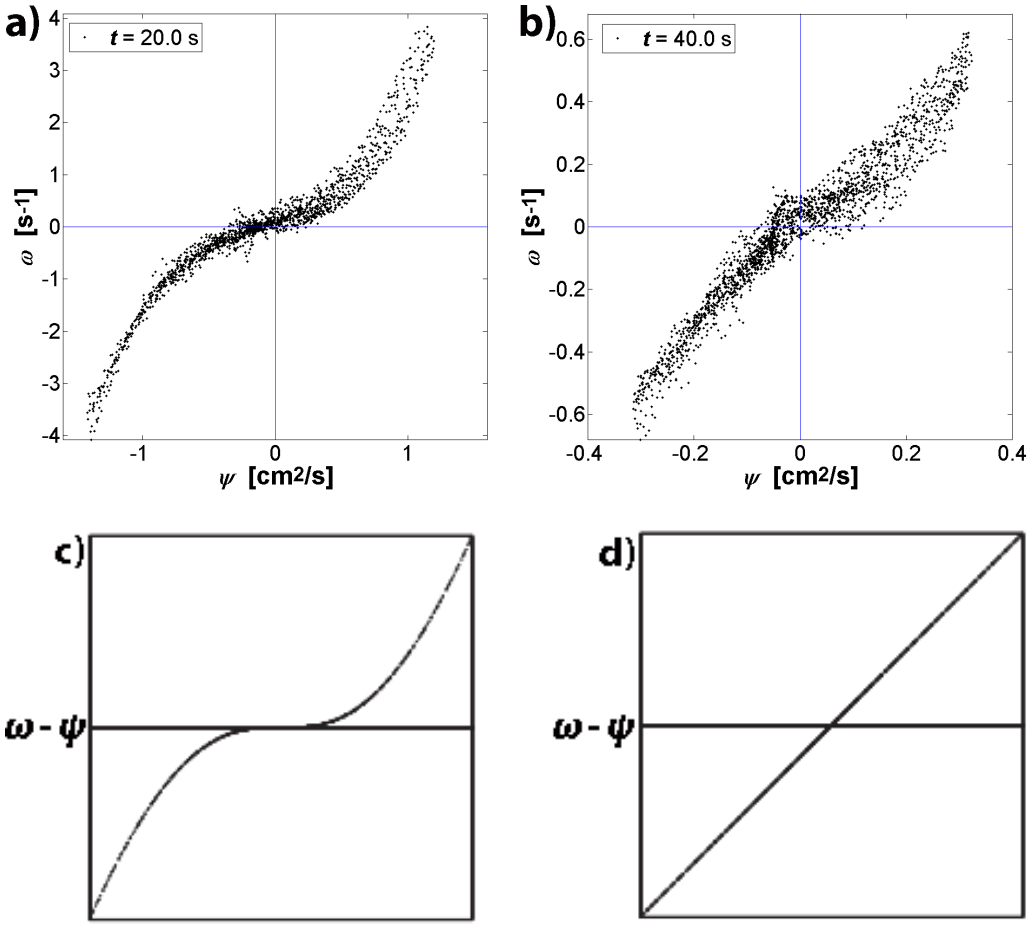

Figure 4.13: Experimentally obtained ω-ψ scatter plot: a) at an early time stage and b) at a later time stage. c),d) The (analytical) ω-ψ relations of the SS and CL-dipole, respectively. c),d): image courtesy of Kizner et al. [15].

Figure 4.13a,b shows the ω-ψ scatter plot computed from experimental data at early and a later time step, respectively. The ω-ψ scatter plot of the SS-dipole and CL-dipole are shown in Figure 4.13c,d respectively.

At early stages the ω-ψ shows a 'curved' shape, visible in Figure 4.13a. This shape is similar to results found by Flór and van Heijst [7] whom compared ω-ψ scatter plots of dipolar vortices in a stratified fluid obtained from experiments with two different ω-ψ relations(analytical):

$$\omega = k^2\psi + \beta\psi^3 \tag{4.2}$$

$$\omega = C\sinh(k^2\psi) \tag{4.3}$$

Equation (4.2) describes a third order polynomial and equation (4.3) describes a sinh-function. Although slightly different, the two functions seem to be similar to the shape of the ω-ψ scatter plot in the early stages of the dipole illustrated in Figure 4.13a. The scatter plot shape at early time stages is similar to the SS-dipole shown in Figure 4.13c.

At later stages, the ω-ψ scatter plot has significantly less 'curved' shaped(more linear-like), shown in Figure 4.13b. This is more comparable to the ω-ψ of the CL-dipole shown in Figure 4.13d.

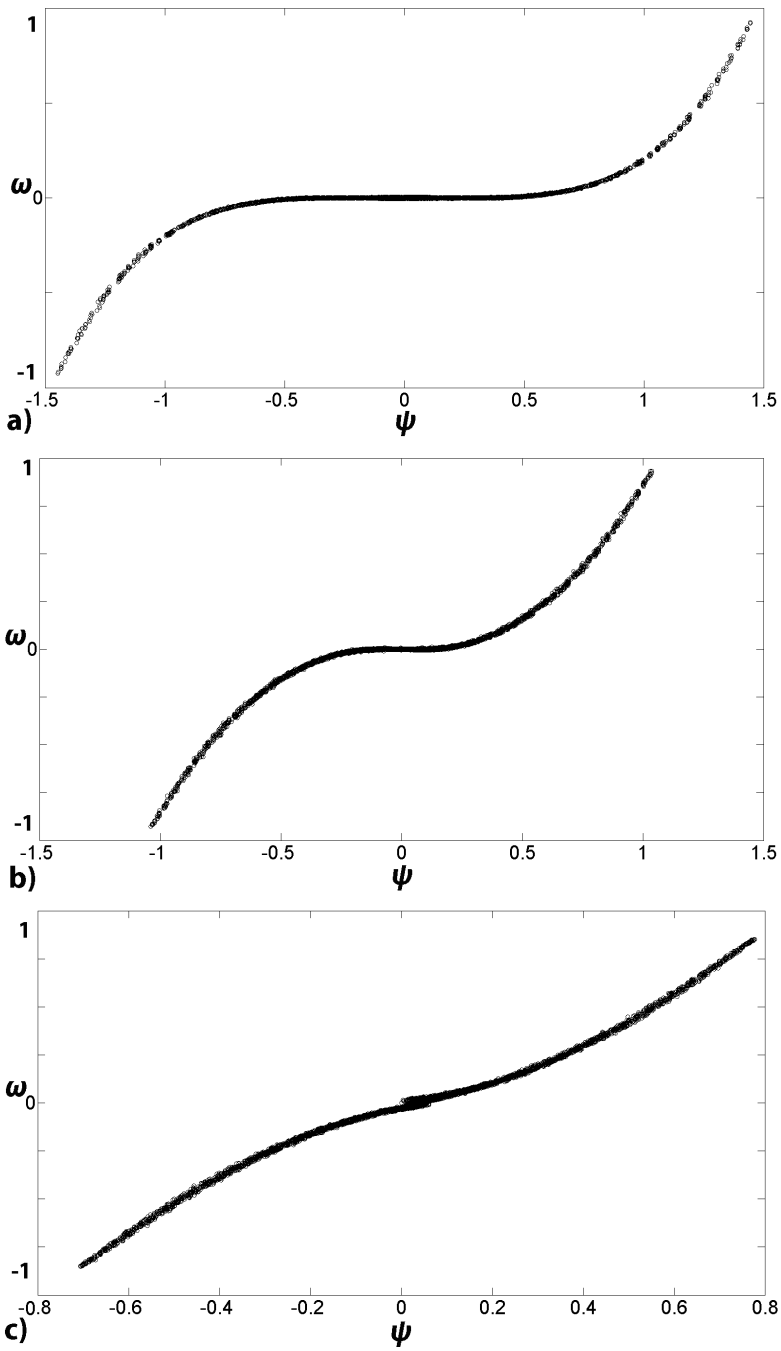

Figure 4.14: Numerically obtained time evolution of the ω-ψ scatter plot. a) ω-ψ scatter plot at an early time stage similar to the PD-case, b) ω-ψ scatter plot at a later time stage similar to the SS-dipole and c) ω-ψ at the final stages which is similar to the CL-dipole.

Figure 4.14 depicts three numerically obtained ω-ψ scatter plots computed from the three snapshots/data corresponding to the simulation shown in Figure 4.6.
Figure 4.14a,b,c shows the time evolution of ω-ψ scatter plots just after formation, the early and later stage. Figure 4.14a,b,c also shows similarity with the PD-like, SS and CL-dipole.

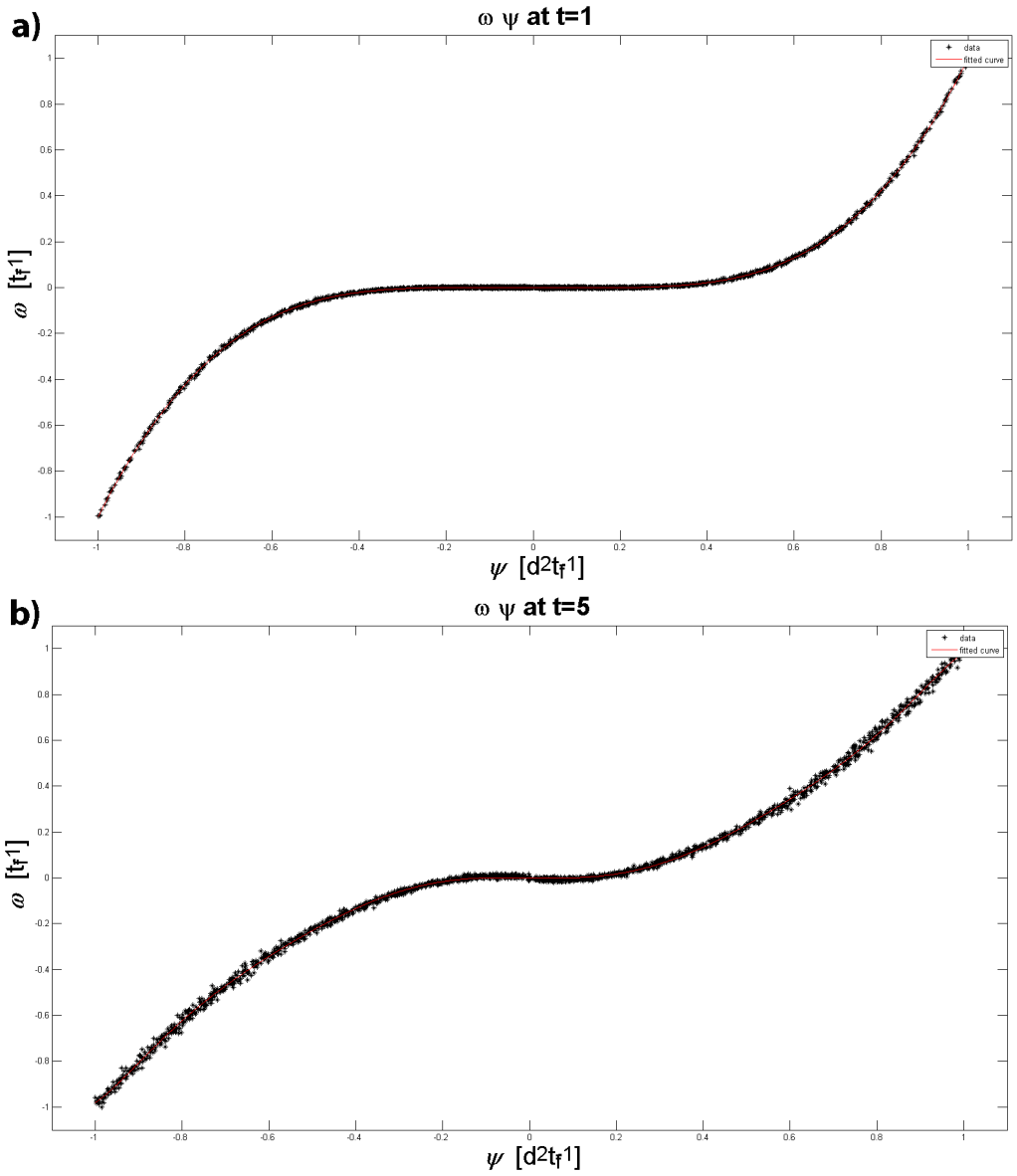

Figure 4.15: Numerically obtained time evolution of the ω-ψ scatter plot. a) ω-ψ scatter plot at $t = 1\ t_f$, b) ω-ψ scatter plot at $t = 5\ t_f$. The scatter plots have been fitted with a 7th order polynomial as described by equation (2.22), indicated by a red line. The ω and ψ are normalized with ω_{max} and ψ_{max}.

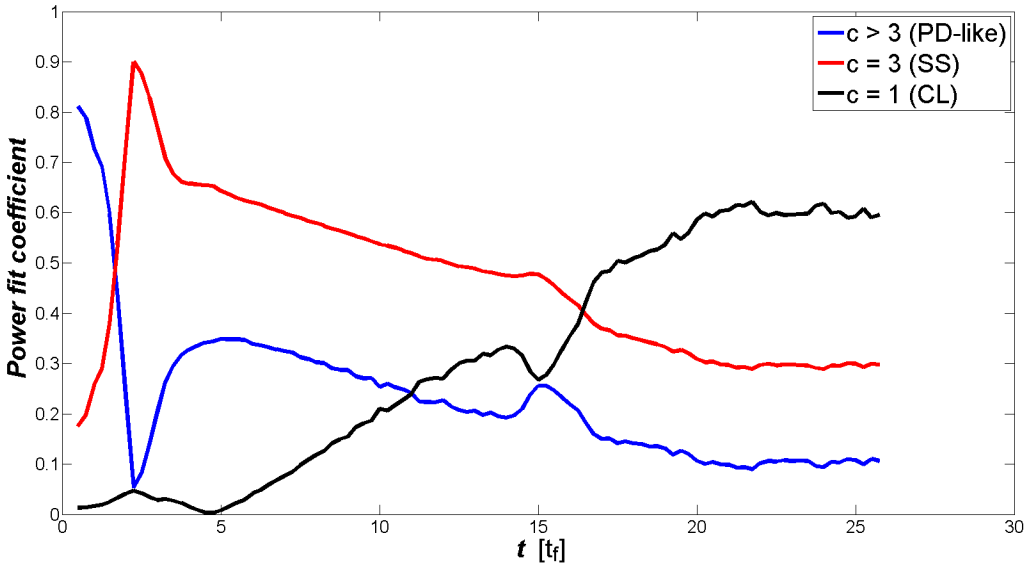

Figure 4.16: Numerically obtained time evolution of the power fit coefficients c_1, c_3, c_5 and c_7. These are normalized with the sum of all the coefficients. The blue line indicates the value of $c_5 + c_7$(PD-like), the red line indicates the value of c_3(SS-like) and the black line indicates the value of c_1(CL-dipole).

Numerically obtained ω-ψ scatter plots are fitted over time. The fit curve is a 7th order polynomial approximation as described by $\omega = c_1\psi + c_3\psi^3 + c_5\psi^5 + c_7\psi^7$(equation (2.22)). Two snapshots of the fitting are shown in Figure 4.15.

The CL, SS and PD-like dipoles are estimated as follows:

1. CL-dipole: $\omega = c_1\psi$
2. SS-dipole: $\omega = c_3\psi^3$
3. PD-like: $\omega = c_5\psi^5 + c_7\psi^7$

The c coefficients are the power fit coefficients and these are normalized with the sum of all the coefficients. The (normalized) coefficients are then plotted over time as shown in Figure 4.16. The blue line indicates the value of $c_5 + c_7$(PD-like), the red line indicates the value of c_3(SS-like) and the black line indicates the value of c_1(CL-dipole).

Figure 4.16 illustrates that the time evolution of the ω-ψ scatter plot shows the trend of being similar to PD-like, then becomes similar to the SS-dipole and then transitioning into a CL-dipole-like shape.

4.3.5 Summary of comparison

The experimental and numerical results of a typical propagating vortex generated by the proposed device have been analyzed by utilizing the vorticity field, vorticity cross-section, the vortex separatrix eccentricity ϵ and the ω-ψ scatter plots.

Typically, the generated dipolar vortex right after formation shows similarity with the point-dipole, at early time stages it is similar to the super-smooth dipole and evolves into a more Chaplygin-Lamb-like dipole at later time stages.

Chapter 5

The dipolar vortex behaviour with varied forcing parameters

The effect of individual forcing parameters on the behaviour of the dipole is investigated. This is again done by considering experiments where a single forcing parameter is varied while the other parameters are kept constant. The investigated properties include:

1. the vorticity field ω
2. the enstrophy Z
3. the vorticity cross-section
4. the vortex core distance d_c
5. the vortex centre propagation speed v_c
6. the $\omega - \psi$ scatter plot

5.1 The effect of varied parameters I and B

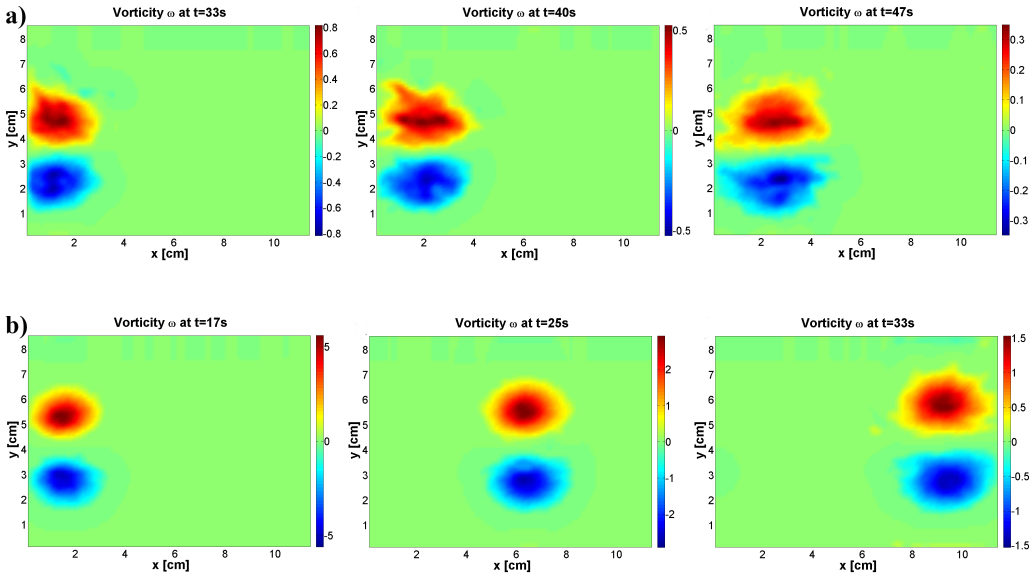

Figure 5.1: Experimentally obtained time evolution of the dipole with forcing parameters: $t_f = 0.5$ s, $d_e = 2.5$ cm, $B = 0.51$ T, but with varying electric current strength I: a) $I = 0.4$ A, b) $I = 1.0$ A. The colour-bar indicates the value of the vorticity ω.

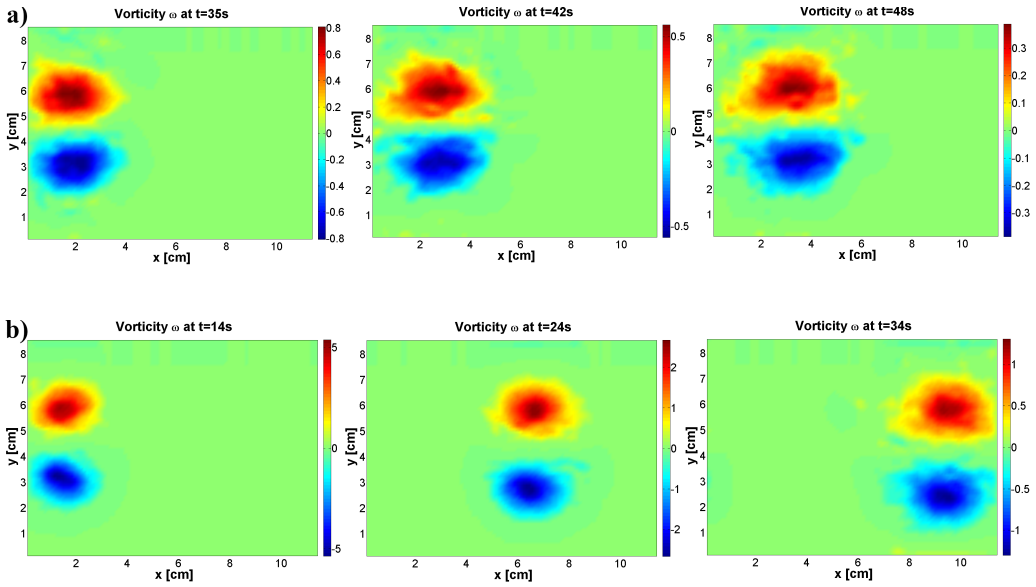

Figure 5.2: Experimentally obtained time evolution of the dipole with parameters: t_f = 0.4 s, I = 1.0 A, d_e=2.5 cm, but with varying B: a) B = 0.25 T, b) B = 0.51 T. The colour-bar indicates the value of the vorticity ω.

The vorticity fields are utilized to visualize the change in the dipolar vortex behaviour when varying the four forcing parameters. The vorticity fields are also used to quantify the change in the absolute maximum vorticity ω_{max} i.e. the highest value of maximum or minimum vorticity.

Experimentally obtained vorticity fields are shown in Figures 5.1 and 5.2 with varied I and B, respectively. These two figures show snapshots of the vorticity fields of a propagating vortex dipole at two different time steps. The first time step corresponds to an early propagation stage and the second time step corresponds to a later stage.
Note that the field of view of the camera is shifted L_{off} = 7cm in the propagation direction (denoted as the x-direction in the figures) with respect to the origin of formation as shown in Figure 3.2a.

The increase in the current I and magnetic field B results in a stronger Lorentz force and consequently the ω_{max} is expected to be higher. Figures 5.1a,b and 5.2a,b show the vorticity fields with I = 0.4 A and I = 1.0 A, B = 0.25 T and B = 0.50 T, respectively.
At around t = 33 s, the vorticity fields in Figures 5.1 and 5.2b with 2.5 times as high I and B have a 2 times as high ω_{max} than Figures 5.1 and 5.2a, respectively.

5.2 The effect of varying t_f

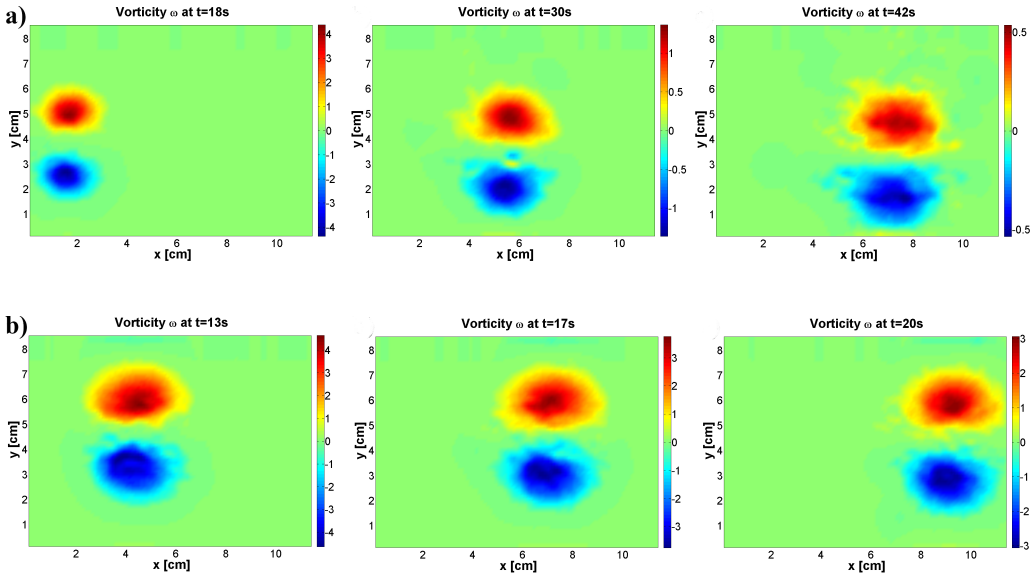

Figure 5.3: Experimentally obtained time evolution of the dipole with parameters: $I = 1.0$ A, $d_e = 2.5$ cm, $B = 0.51$ T, but with varied forcing time t_f: a) $t_f = 0.4$ s, b) $t_f = 1.0$ s. The colourbar indicates the value of the vorticity ω.

Figure 5.3a,b show the vorticity fields with $t_f = 0.4$ s and $t_f = 1.0$ s, respectively. The observation of Figure 5.3a,b at $t = 18$ s or $t = 17$ s, respectively shows that for higher t_f, slightly higher values of ω_{max} are observed.

Between Figure 5.3a,b at $t = 18$ s or $t = 17$ s, respectively the difference in vortex size d_v is the most notable. The dipole in Figure 5.3a with $t_f = 0.4$ s results in $d_v = 4.0$ cm and in Figure 5.3b with $t_f = 1.0$ s results in $d_v = 5.5$ cm.

5.3 The effect of varying d_e

The fourth and last studied forcing parameter is the electrode gap distance d_e. It is expected that varying the d_e affects the density current J. For example bringing the electrodes closer together should lead to an increased J, assuming that the current I with smaller d_e is then effectively driven through a smaller cross-sectional surface. The cross-sectional surface A as function of d_e is defined as follows:

$$A(d_e) = HL_J(d_e) \tag{5.1}$$

with H the fluid depth and $L_J(d_e)$ the electric current cross-sectional length which is numerically obtained defined as when the integral of J over L_J encompasses 95% of the total current I running through the fluid.

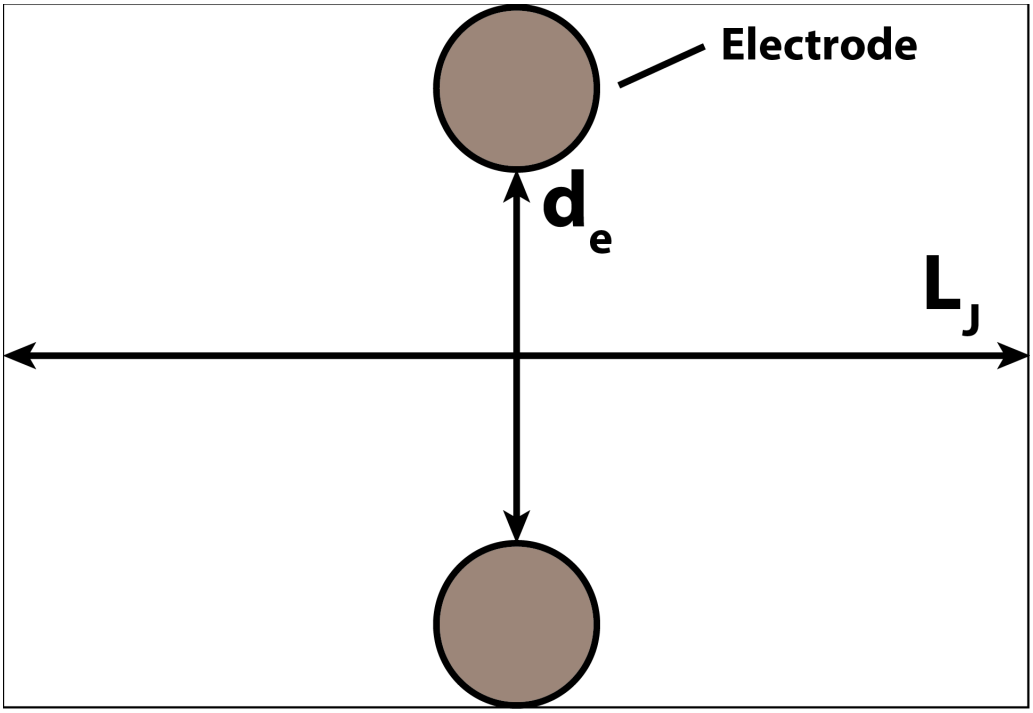

Figure 5.4: A figure showing a sketch of d_e, L_J and the two electrodes. L_J is the cross-sectional length in the 2-D electric numerical model that is is determined when the line integral of J over L_J encompasses 95% of the total current running through the fluid.

Figure 5.4 illustrates a sketch of d_e, L_J and the two electrodes.

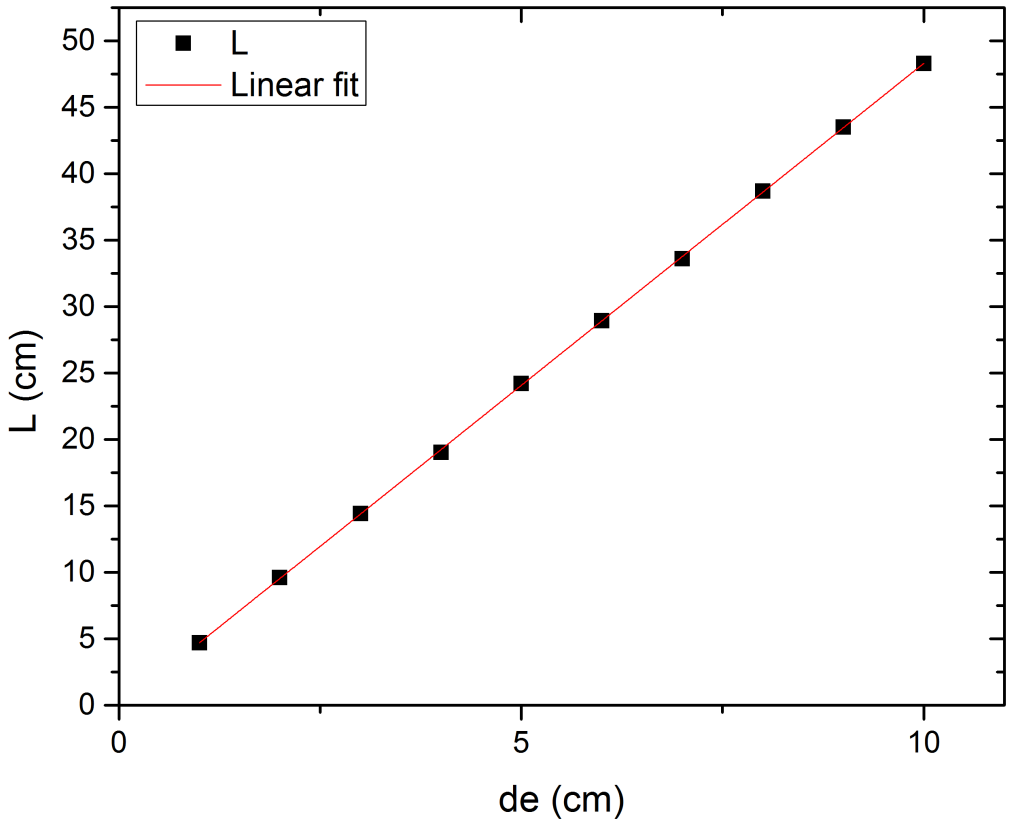

Figure 5.5: Figure depicting the numerically obtained L_J as a function of d_e. The graph shows a linear relation between $L_J(d_e)$ and d_e. Where L_J is the cross-sectional length that encompasses 95 % of the electric current running through the fluid. The linear fit has a slope of $\alpha = 4.84 \pm 0.01$.

Figure 5.5 shows L_J as a function of d_e computed using the numerical (2D) electric model. The d_e is varied from 1 cm to 10 cm with increments of 1 cm. The measurements points are indicated by black markers and a linear fit is applied, which matches sufficiently. The linear fit has a slope of $\alpha = 4.84 \pm 0.01$ and using the found value of α results in:

$$A(d_e) = \alpha H d_e = 4.84 H d_e \tag{5.2}$$

Then using equation (5.2), the current density can be defined as follows

$$J = \frac{I}{4.84 H d_e} \tag{5.3}$$

where I is the electric current, H the fluid depth and d_e the electrode gap distance.

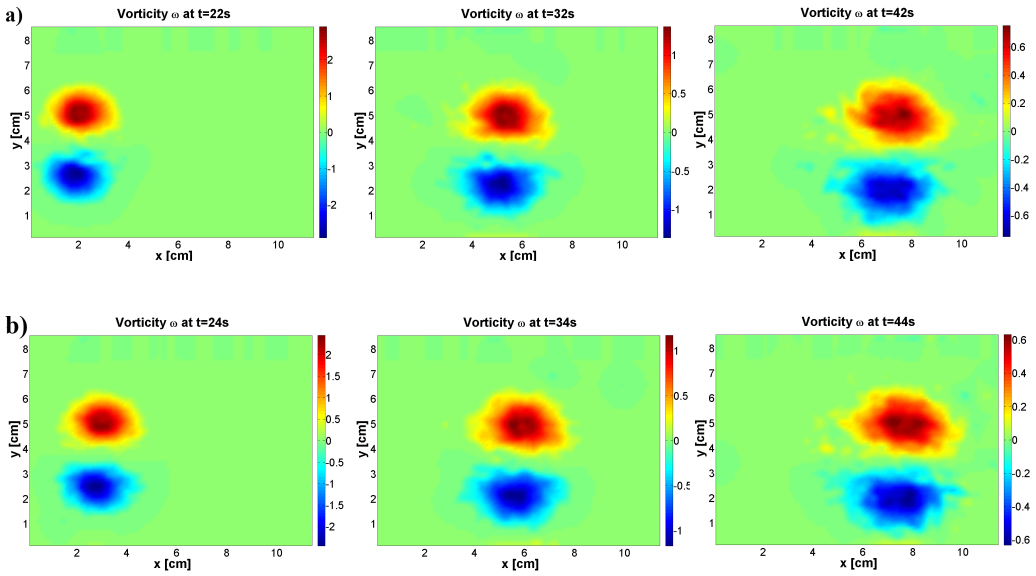

Figure 5.6: Experimentally obtained time evolution of the dipole with parameters: $t_f = 0.5$ s, $I = 0.6$ A, $B = 0.51$ T, but with varying electrode gap distance d_e: a) $d_e = 1.0$ cm, b) $d_e = 2.5$ cm. The colourbar indicates the value of the vorticity ω.

Figure 5.6a,b shows experimentally obtained vorticity fields, with d_e being varied from 1.0 cm to 2.5 cm, respectively.
At around $t = 22$ s, the difference in d_e results in relatively constant values ω_{max} and the dipole size d_v also stays relatively constant.

Equation (5.3) shows that an increase in electrode distance d_e results in a decrease in J. Therefore, it is expected that increasing d_e results in a weaker Lorentz force and consequently in a lower ω_{max}. However, there is only a relatively small decrease in ω_{max} observable in Figure 5.6a,b.

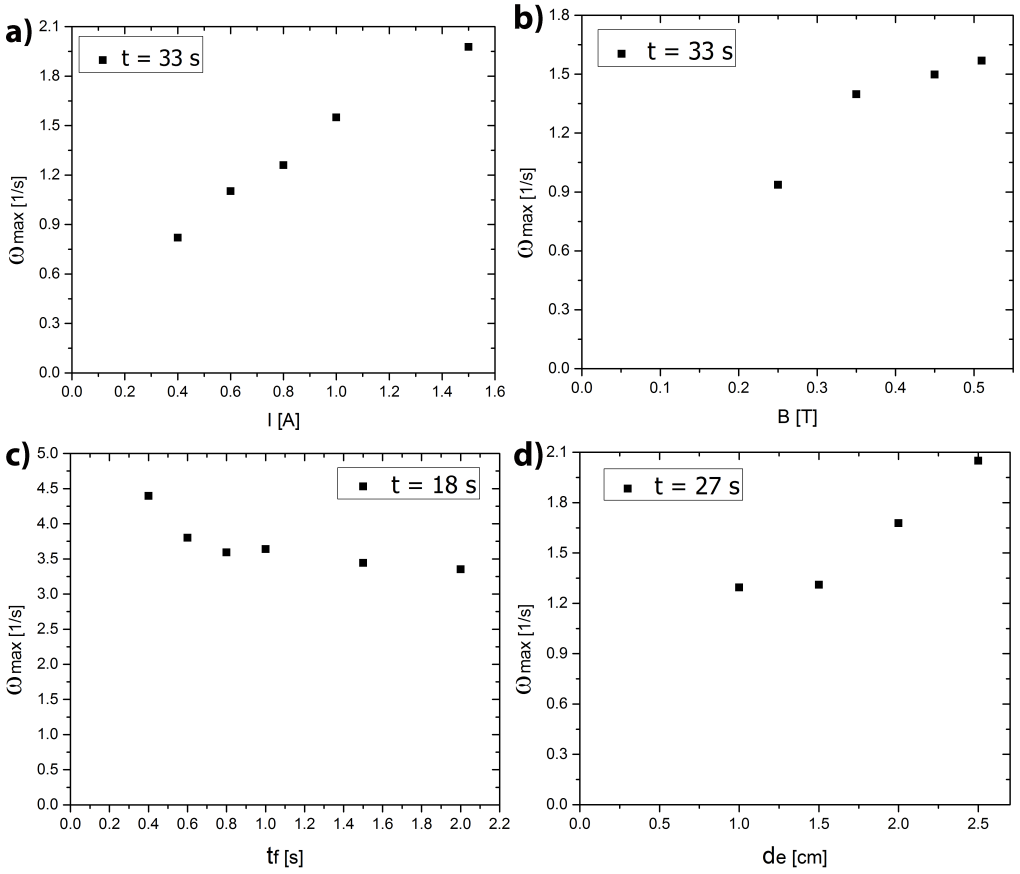

Figure 5.7: Experimentally obtained figure giving an overview of the effect of varying forcing parameters on the absolute maximum vorticity ω_{max}.

Figure 5.7a-d gives an overview of ω_{max} as a function of the forcing parameters I, B , t_f and d_e, respectively. For increased values of I and B results in higher values of ω_{max}. For higher values t_f shows slightly lower values for $omega_{max}$. Figure 5.7d shows a different trend than observed in Figure 5.6, where increasing d_e does not result in a lower ω_{max}, but instead results in a higher ω_{max}.

5.4 The enstrophy decay time t_d

The enstrophy Z is defined as:

$$Z = \frac{1}{2} \iint_S \omega^2 dS \tag{5.4}$$

where the integration of ω^2 is over a surface S, which is the camera field of view. Z is the enstrophy and ω is the vorticity.

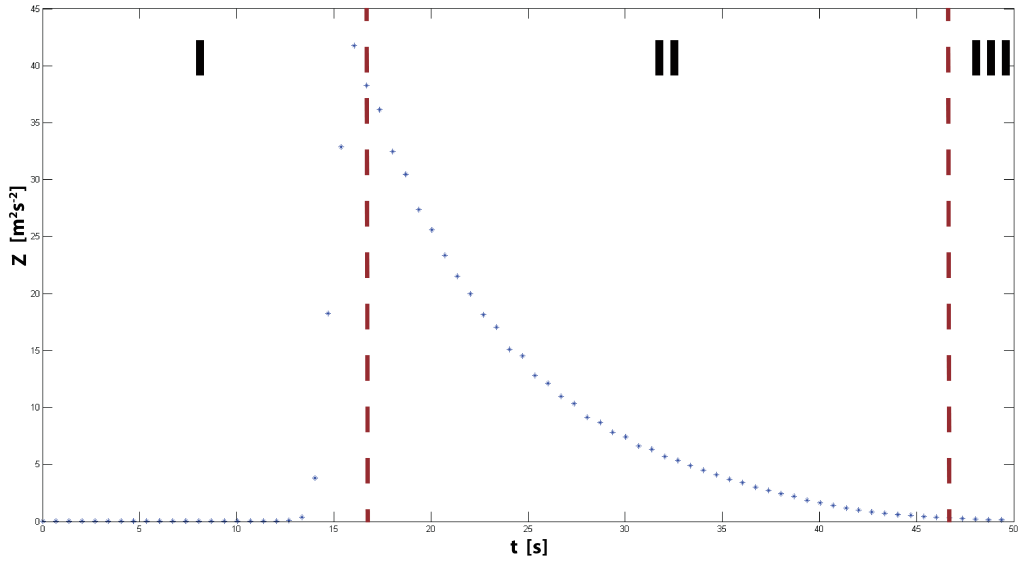

Figure 5.8: Experimentally obtained time evolution of the enstrophy Z with (forcing) parameters: $I = 1.0$ A, $B = 0.51$ T, $t_f = 0.5$ s s and $d_e = 2.5$ cm. The two dashed red lines indicate the time interval where the graph is fitted as shown in Figure 5.9

The property enstrophy measured over a larger time scale is utilized for estimating the enstrophy decay time t_d. Figure 5.8 shows the time evolution of the enstrophy Z for parameters: $I = 1.0$ A, $B = 0.51$ T, $t_f = 0.5$ s and $d_e = 2.5$ cm.

In order to estimate the decay time of the enstrophy, Figure 5.8 is fitted with the function $ae^{-t/b}$. Swaters et al. [19] and Flór et al. [20] also used an exponential function to describe viscous decay of dipoles (in stratified fluid). The fitted graph is shown in Figure 5.9.

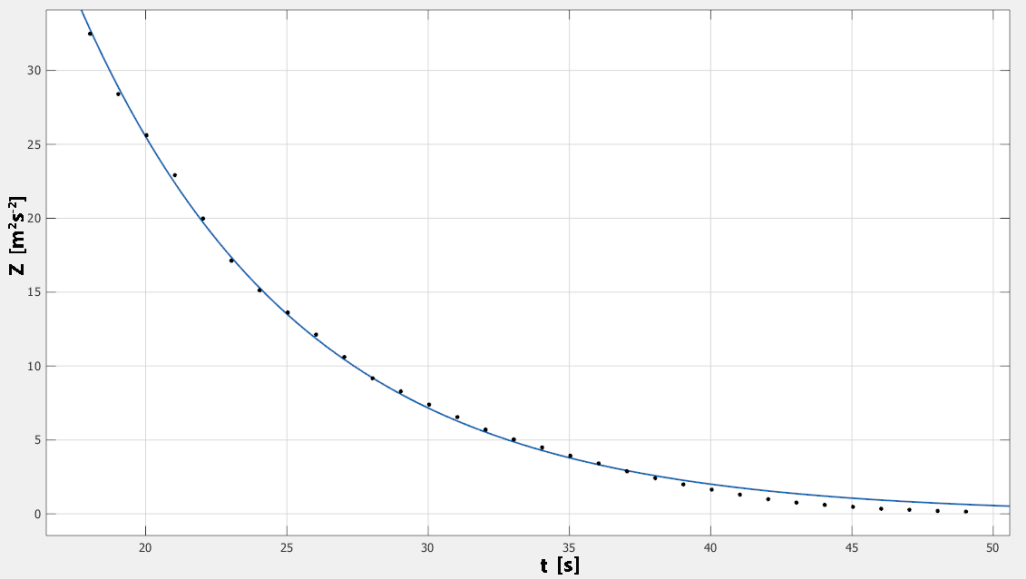

Figure 5.9: Experimentally obtained time evolution of the enstrophy that is fitted with an exponential function $ae^{-t/b}$ which models the enstrophy decay rate. The region that is shown corresponds to the one indicated by the two dashed red lines, e.g. in Figure 5.8.

The enstrophy is modeled with:

$$Z(t) = Z_0 \, e^{-\frac{t}{t_d}} \tag{5.5}$$

The two dashed lines in Figure 5.8 indicate the fit time interval and splits the graph into three time intervals i.e. I, II and III. Time interval I corresponds to the dipole coming into the field of view so enstrophy Z keeps increasing until the dashed line on the left-hand side. Time interval II is the fit time interval. Time interval III is the interval where the dipole is either starting to move out of the field of view and/or has very low vorticity values, which decreases the accuracy of PIV measurements.

Experiment #	Z_0 $[m^2s^{-2}]$	Decay time t_d $[s]$
$I_{0.4A}$	54	8.8
$I_{1.0A}$	320	7.9
$B_{0.25T}$	41	10.6
$B_{0.51T}$	187	8.5
$t_{f_{0.4s}}$	290	6.7
$t_{f_{1.0s}}$	274	7.8
$d_{e1.0cm}$	125	6.9
$d_{e2.5cm}$	125	9.1

Table 5.1: Table giving an overview of the experimentally obtained fit coefficients $a(Z_0)$ and $b(t_d)$ with the fit function $ae^{-\frac{t}{b}}$ with varied forcing parameters.

The fit coefficient a estimates the enstrophy at $t = 0$ (Z_0), the fit coefficient b estimates the enstrophy decay time t_d. The two fit coefficients a and b are computed for different measurements (with varying various forcing parameters). The results are summarized in Table 5.1.

The values presented in Table 5.1 show that increasing I and B increases the value found for Z_0. This is expected as an increase in I and B results in a stronger Lorentz force.

This is in contrast to varying t_f and d_e where Z_0 remains relatively unchanged. This can be linked to ω_{max} which also stays relatively constant for varied t_f and d_e. For t_f, this can be explained as with longer forcing times where typically $t_f > 1.0s$ starts to induce a more turbulent dipole formation. During this turbulent formation, the flow can no longer be approximated as 3D effects become more dominant. The transition to a more turbulent flow can possibly cause decay and energy loss during the formation phase. This means that increasing t_f above a certain critical t_{fc} value, the formation phase is relatively more turbulent. Possibly, the generation of vorticity is less efficient as energy is lost through 3-D effects. Therefore increasing t_f after t_{fc} has a relatively small effect on the resulting Z_0.

The found decay times t_d are calculated over a large time interval where the most of the time the flow can be considered Q2D. Then the bottom friction and thus viscosity is the important factor in the decay of the dipole. As the viscosity is constant in all experimental measurements, the t_d is expected to be relatively constant.

The experimentally found t_d in various measurements seems to be relatively constant, indicating that t_d is independent of the forcing parameters, as expected.

The effect of bottom friction in shallow fluid layers on the decay of dipolar vortices (Q2D turbulence) was investigated numerically (2D-simulation) by Clercx et al. [21].

Clercx et al. modeled the enstrophy Z as follows:

$$Z(t) = Z_0 \, e^{-2\lambda t} \tag{5.6}$$

with $Z(t)$ the total enstrophy, $Z(0)$ the enstrophy at t =0 and λ the bottom-friction coefficient. Using equation (5.5) and equation (5.6) then conversion of λ to the enstrophy decay time $t_d = 1/2\lambda$. The results from the study of Clercx et al. and the from λ converted decay times t_d are then:

H [mm]	λ [s^{-1}]	t_d [s]	Re
4	0.15	3.3	1500
6	0.07	7.1	2000
8	0.038	13.2	3000

Table 5.2: Table giving an overview the results of Clercx et al. [21] of bottom friction decay rates λ in fluid with different fluid depth H and the from λ converted t_d. The corresponding Re-values are also given.

Table 5.1 shows that increasing t_f and d_e does not affect the calculated Z_0 significantly. To confirm this, the dependency of Z_0 and t_d on t_f is investigated. Ten measurements have been performed with I = 1.0 A, B = 0.51 T, d_e = 2.5 cm with t_f = 0.2, 0.3, 0.4, 0.5, 0.7, 1.0, 1.2, 1.5, 2.0, 3.0 s.

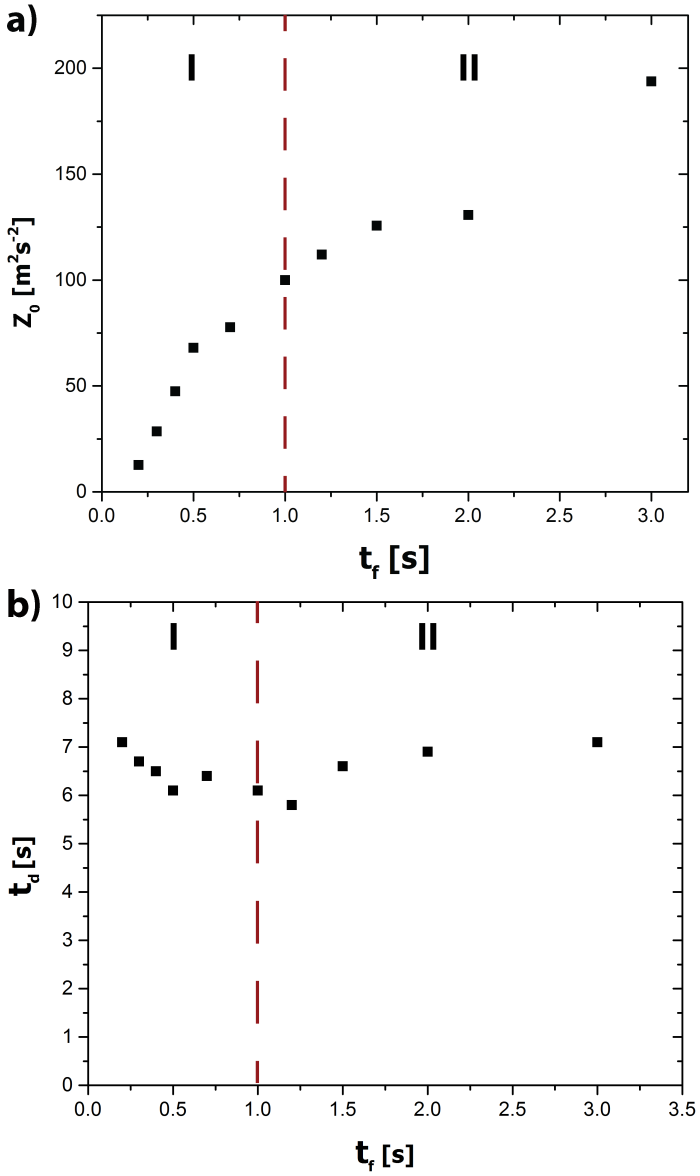

Figure 5.10: A figure showing experimentally obtained a) Z_0 and b) t_d versus forcing time t_f from different experiments. The forcing parameters are: I = 1.0 A, B = 0.51 T, d_e = 2.5 cm with varied t_f = 0.2, 0.3, 0.4, 0.5, 0.7, 1.0, 1.2, 1.5, 2.0, 3.0 s. The dashed line indicates the separates two regimes: I) laminar formation phase and II) transition to a more turbulent formation phase.

The parameters Z_0 and t_d are then plotted versus t_f and shown in Figure 5.10a,b respectively. The dashed line in Figure 5.10 indicates two regimes: I) laminar formation phase and II) transition to a more turbulent formation

phase. The transition to a more turbulent phase occurs with longer forcing times $t_f \geq 1.0$ s.

The result of Clercx et al. [21] for a fluid depth of H= 8 mm is $t_{d_{clercx}} = 13.2$ s and the experimentally obtained decay time in this study is $t_d = 7.5$ s. Note that Clercx et al. used a one-layer shallow fluid layer while in this study a two-layer stratified shallow layer is used. Therefore, $t_d \geq t_{d_{clercx}}$ is expected as stratification results in longer decay times. But the found results have shorter decay times instead.

This can be explained as the numerical study of Clercx et al. [21] was a 2D simulation but the flow in experiments is Q2D. Thus 3D effects can have a role in causing the found discrepancy. Furthermore, the decay times are fitted not from $t = 0$ but from a later time ($t \simeq 20$ s) which can lead to errors in estimating t_d.

5.5 The effect of stronger forcing on the generated dipolar vortex.

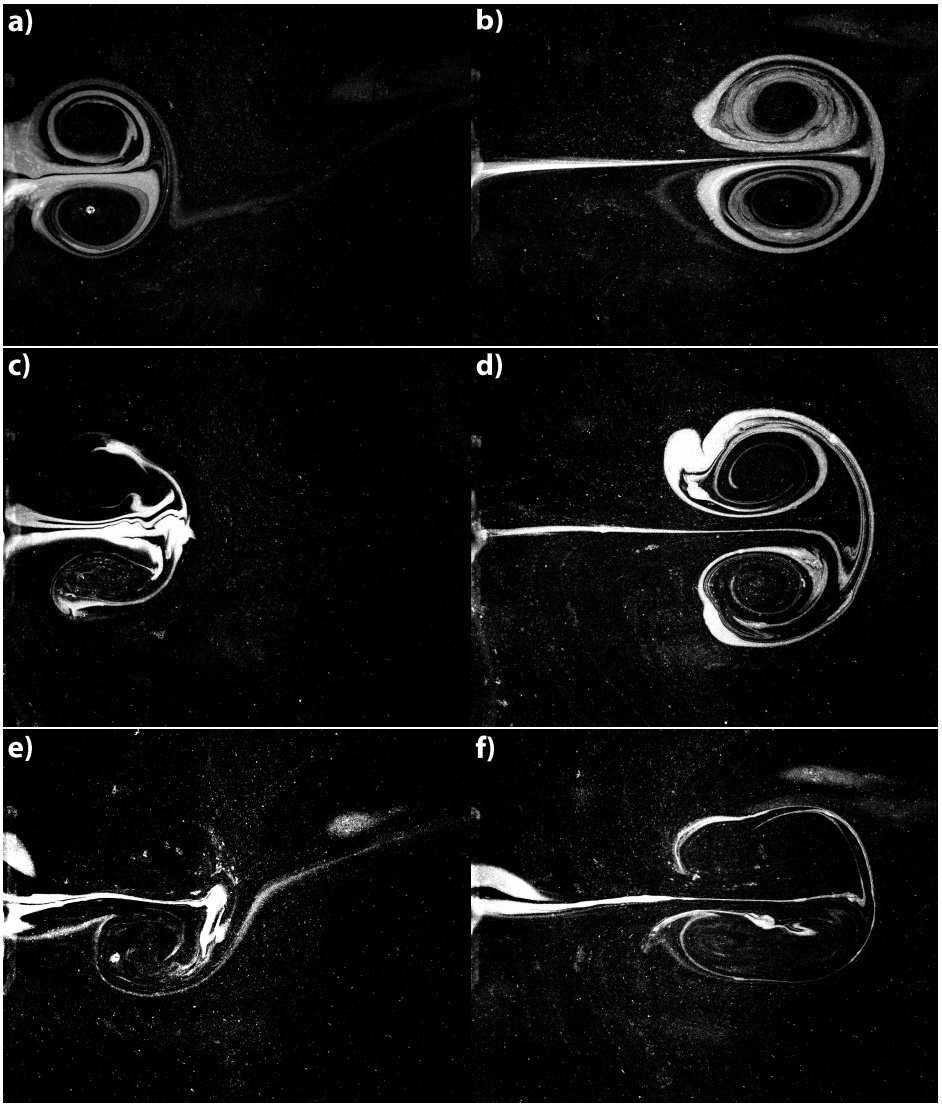

Figure 5.11: Figure showing three experiments with $B = 0.51$ T, $t_f = 0.5$ s and $d_e = 2.5$ cm but with three values for I: a,b) 1.0 A, c,d) 2.0 A and e,f) 3.0 A. a,b) show a laminar flow, c) shows a deformed dipole cause by the relatively turbulent formation but in d) the flow becomes laminar and a dipole emerges. e,f) both show a deformed dipole because of the relative turbulent formation and a dipole emerges out significantly later, out of the field of view.

The transition to a more turbulent formation phase occurs when $t_f >$ 1.0 s but also when I or B are increased to a certain value. This is because increasing I, B and t_f effectively increases the energy/momentum generated into the fluid.

To visualize this transition, three measurements are performed with $B =$ 0.51 T, $t_f = 0.5$ s and $d_e = 2.5$ cm but with three values for I: 1.0, 2.0 and 3.0A. These are shown in Figure 5.11a+b,c+d,e+f respectively.
Figure 5.11a,b shows the measurement with $I = 1.0$ A where the flow is laminar in both snapshots. For $I = 2.0$ A, the fluid jet is not laminar in Figure 5.11c and transitions to a more laminar flow in Figure 5.11d. For $I = 3.0$ A, both snapshots Figure 5.11e,f show a transition to a relatively turbulent flow.

The more turbulent formation phase results in unpredictable propagation trajectories and symmetry of the dipolar vortex. To counteract this, the optimal forcing time t_f is set at $t_f \leq 1.0$ s.

5.6 The behaviour of the vortex size d_v with varied forcing parameters

The vortex size d_v is defined as the size of the vortex separatrix. The vorticity cross-sections can be utilized to estimate d_v and thus the time evolution of the vorticity cross-section can be used to determine the time evolution of d_v.

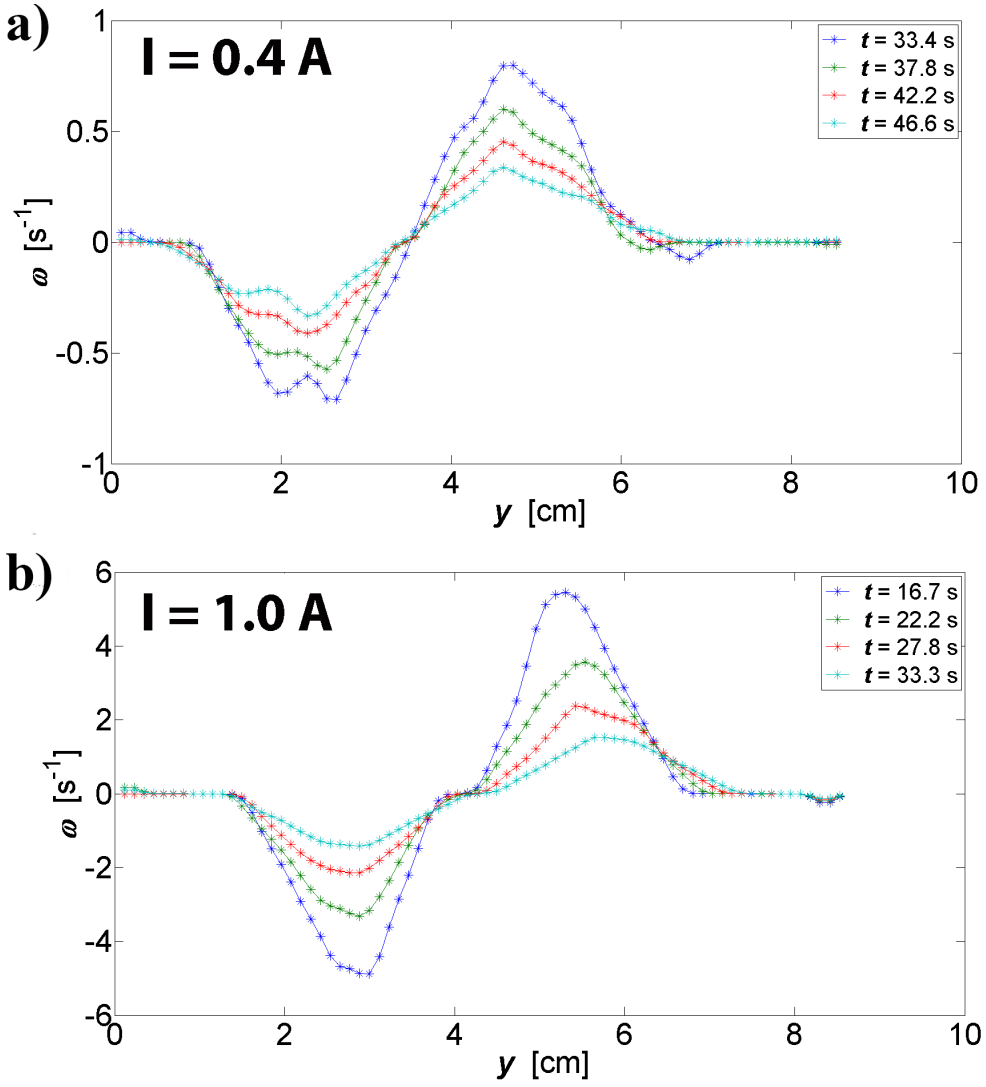

Figure 5.12: Experimentally obtained vorticity cross-sections with constant forcing parameters $B = 0.51$ T and $d_e = 2.5$ cm, $t_f = 0.5$ s but for different values of I: a) $I = 0.4$ A, b) $I = 1.0$ A.

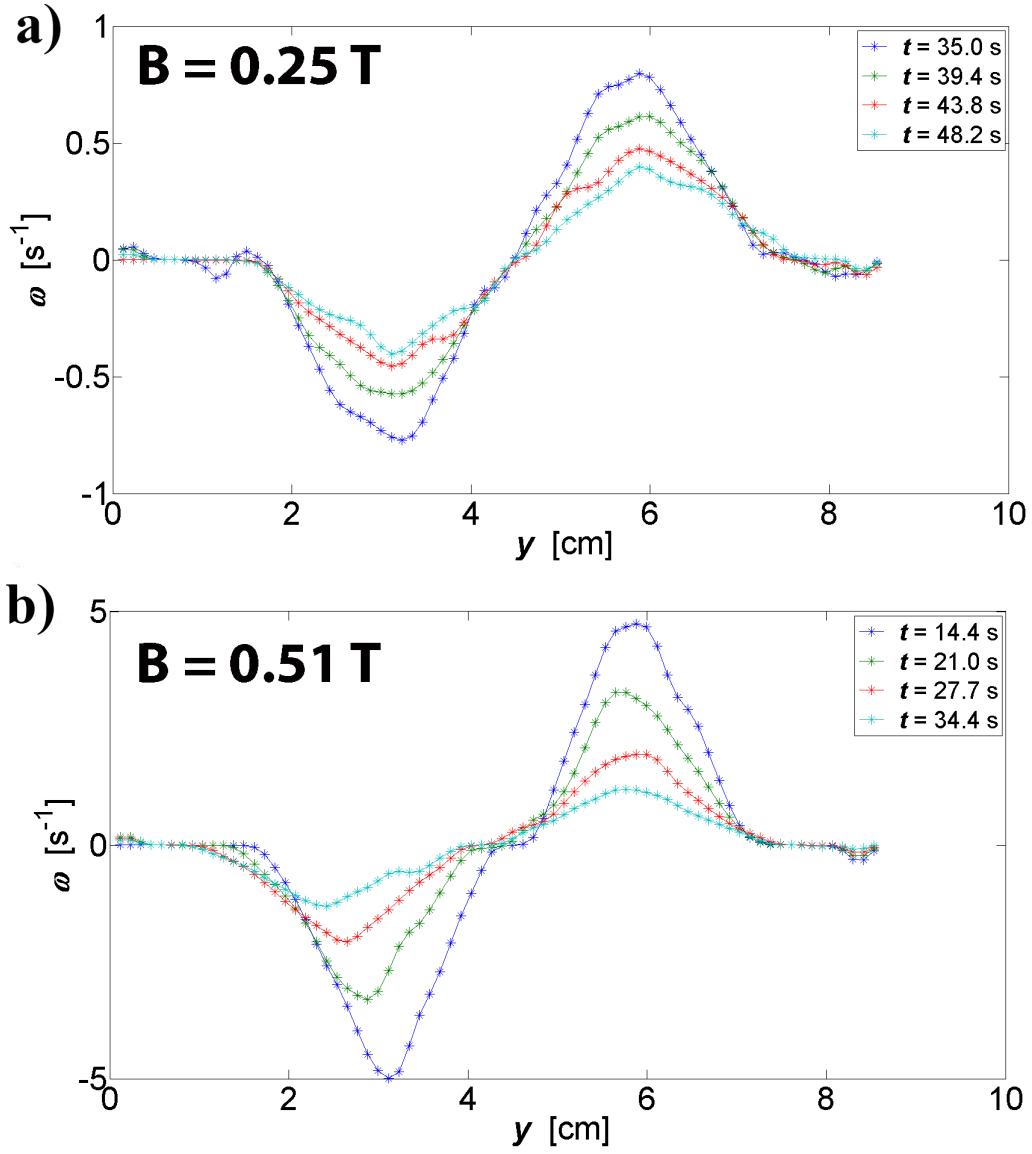

Figure 5.13: Experimentally obtained vorticity cross-sections with constant forcing parameters $I = 1.0\ A$, $d_e = 2.5\ cm$ and $t_f = 0.5\ s$ for different values of B: a) $B = 0.25\ T$, b) $B = 0.51\ T$.

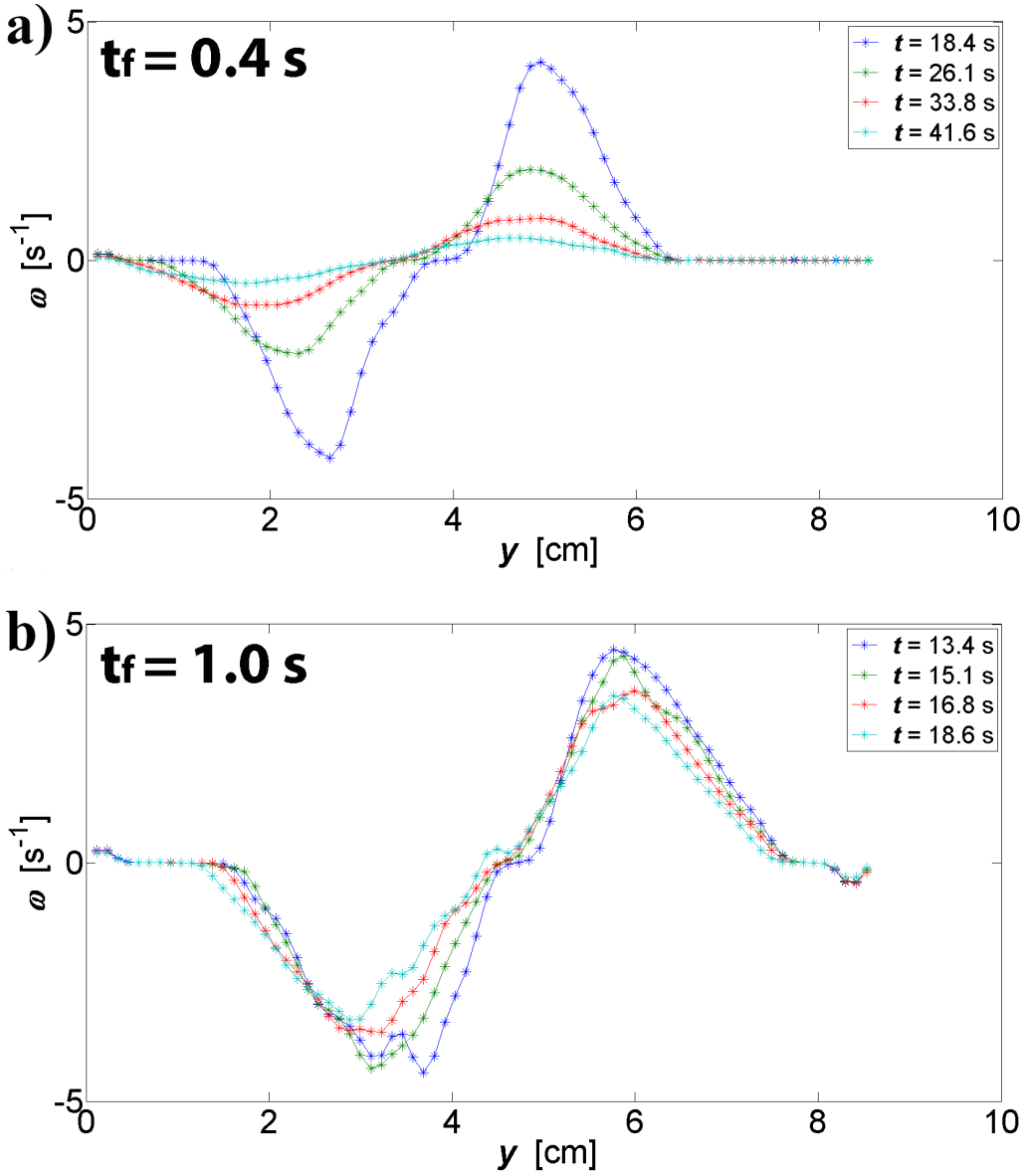

Figure 5.14: Experimentally obtained vorticity cross-sections with constant forcing parameters $I = 1.0$ A, $B = 0.51$ T and $d_e = 2.5$ cm but for different values of t_f: a) $t_f = 0.4$ s, b) $t_f = 1.0$ s.

Figures 5.12, 5.13 and 5.14 show the vorticity cross-sections with varied I, B and t_f, respectively.
The increase in I and B does not affect the total size of the vortex d_v significantly which stays 7 cm. The increase in t_f affects d_v slightly. The measurements with $t_f = 0.4$ s and $t_f = 1.0$ s show values of $d_v = 5$ cm and $L_v = 6$ cm, respectively.

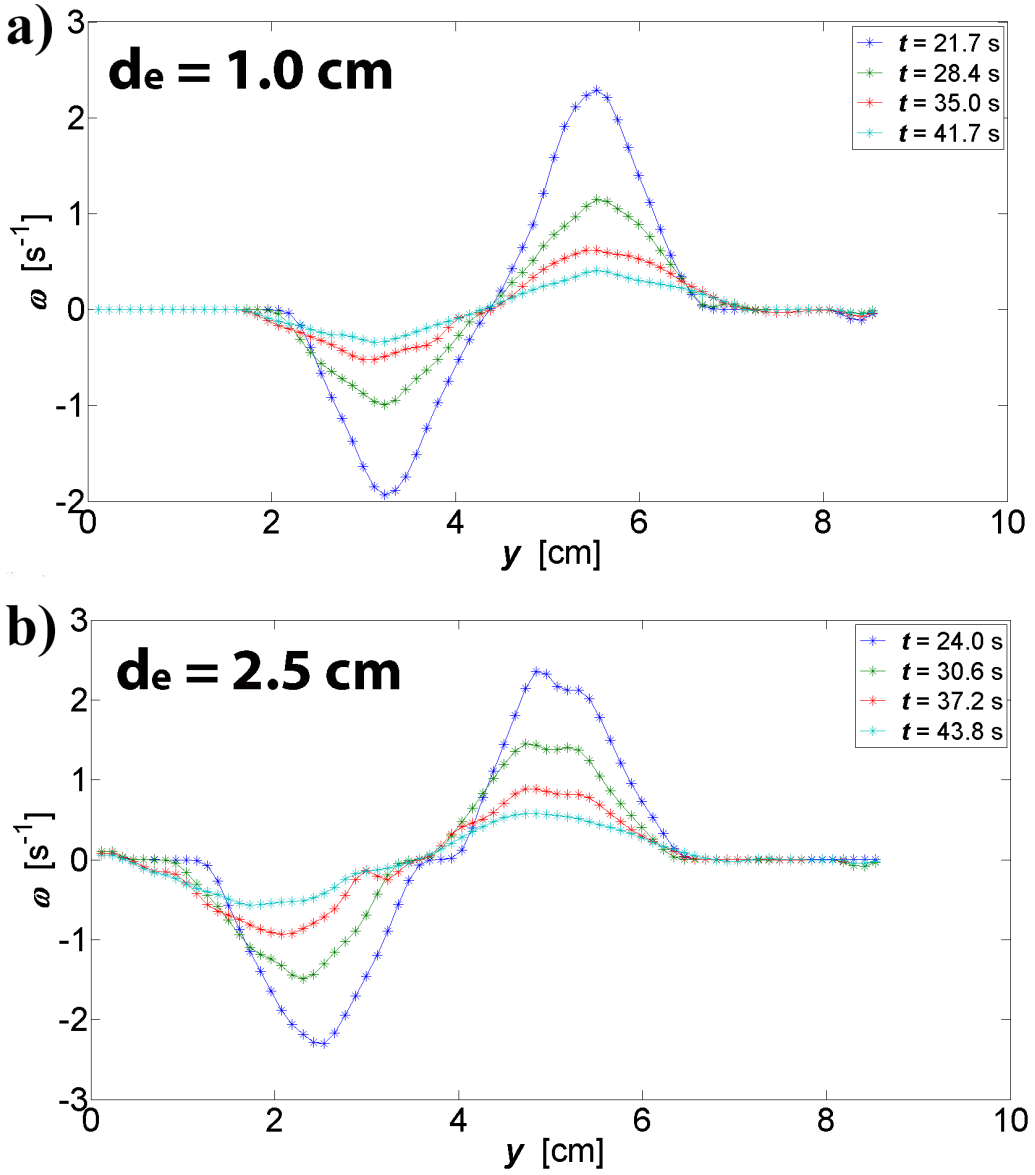

Figure 5.15: Experimentally obtained vorticity cross-sections with constant forcing parameters $I = 1.0\ A$, $B = 0.51\ T$ and $t_f = 0.5\ s$ but for different values of d_e: a) $d_e = 1.0\ cm$, b) $d_e = 2.5\ cm$.

Figure 5.15 shows the cross-sections for varied d_e. Figure 5.15a,b shows the cross-sections with $d_e = 1.0$ cm and $d_e = 2.5$ cm, which show a slight increase with $d_v = 4.5$ cm and $d_v = 5$ cm, respectively.
These measurements were performed after $t = 22$ s. The effect of varied d_e on the vortex size might be more notable during an earlier time stage.

5.7 Vortex core separation distance d_c as a function of time

The alternative method of determining the vortex size is using the vortex core separation distance d_c. The vortex core separation distance d_c is defined as the distance between the positive and negative vortex core.

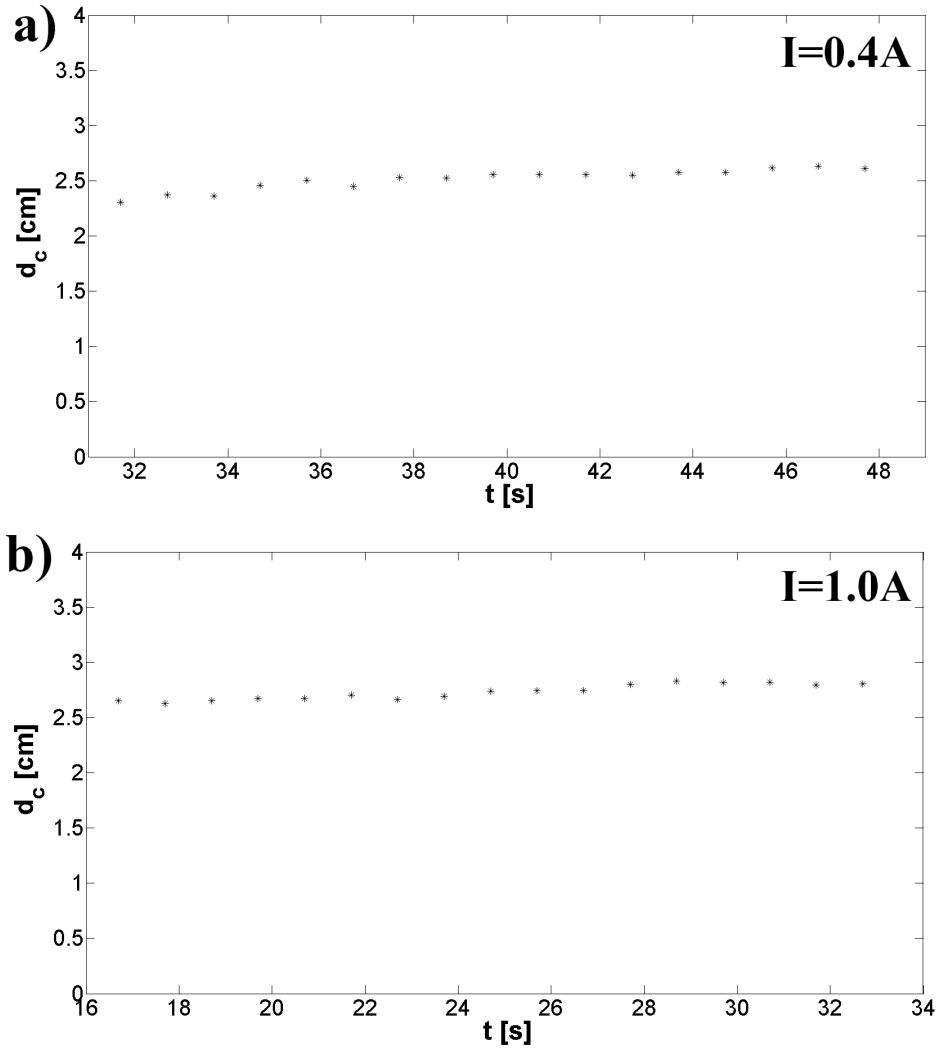

Figure 5.16: Experimentally obtained time evolution of d_c with constant forcing parameters $B = 0.51$ T, $d_e = 2.5$ cm and $t_f = 0.5$ s but for different values of I: a) $I = 0.4$ A, b) $I = 1.0$ A.

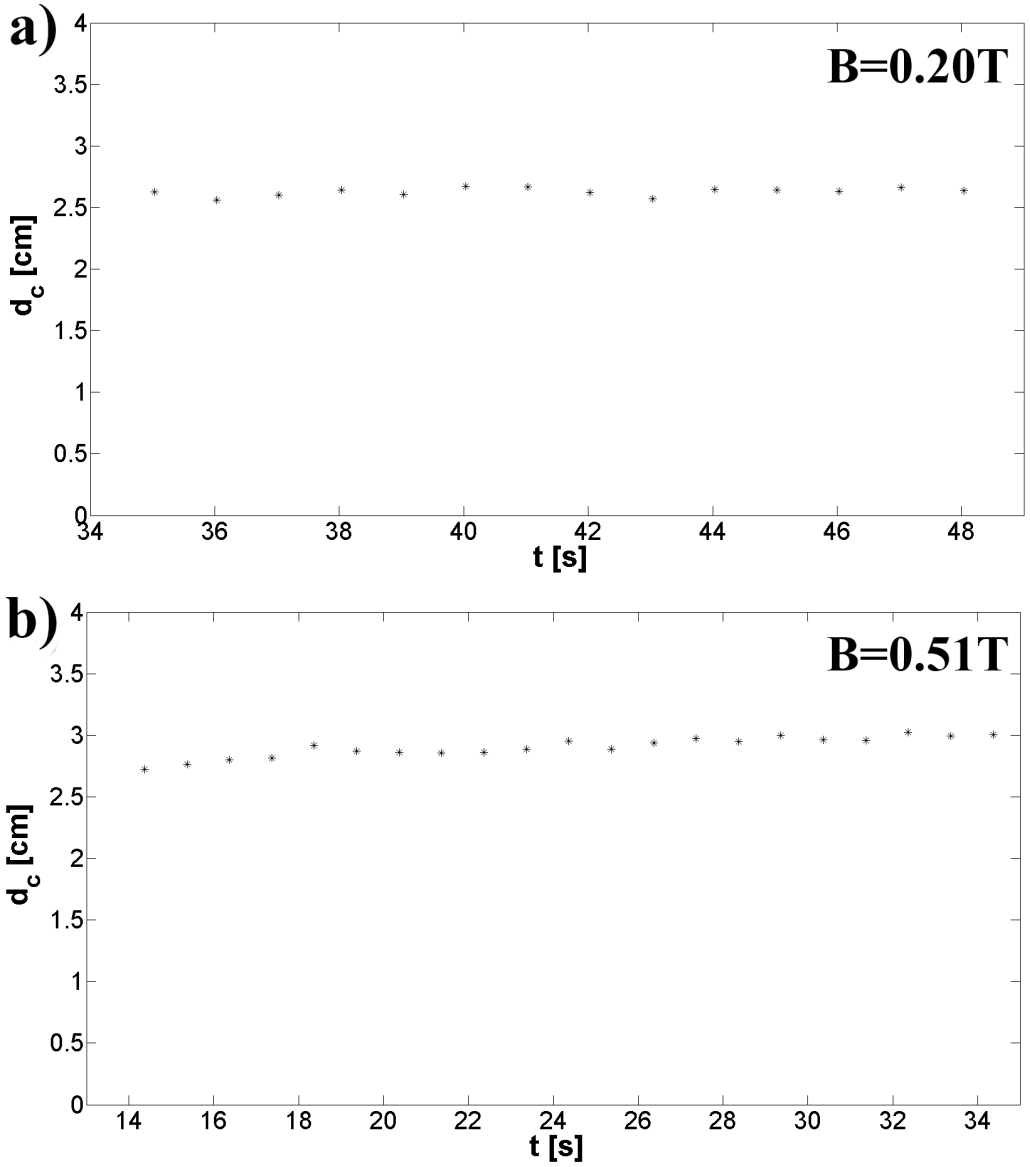

Figure 5.17: Experimentally obtained time evolution of d_c with constant forcing parameters $I = 1.0\ A$, $d_e = 2.5\ cm$ and $t_f = 0.5\ s$ but for different values of B: a) $B = 0.20\ T$, b) $B = 0.51\ T$.

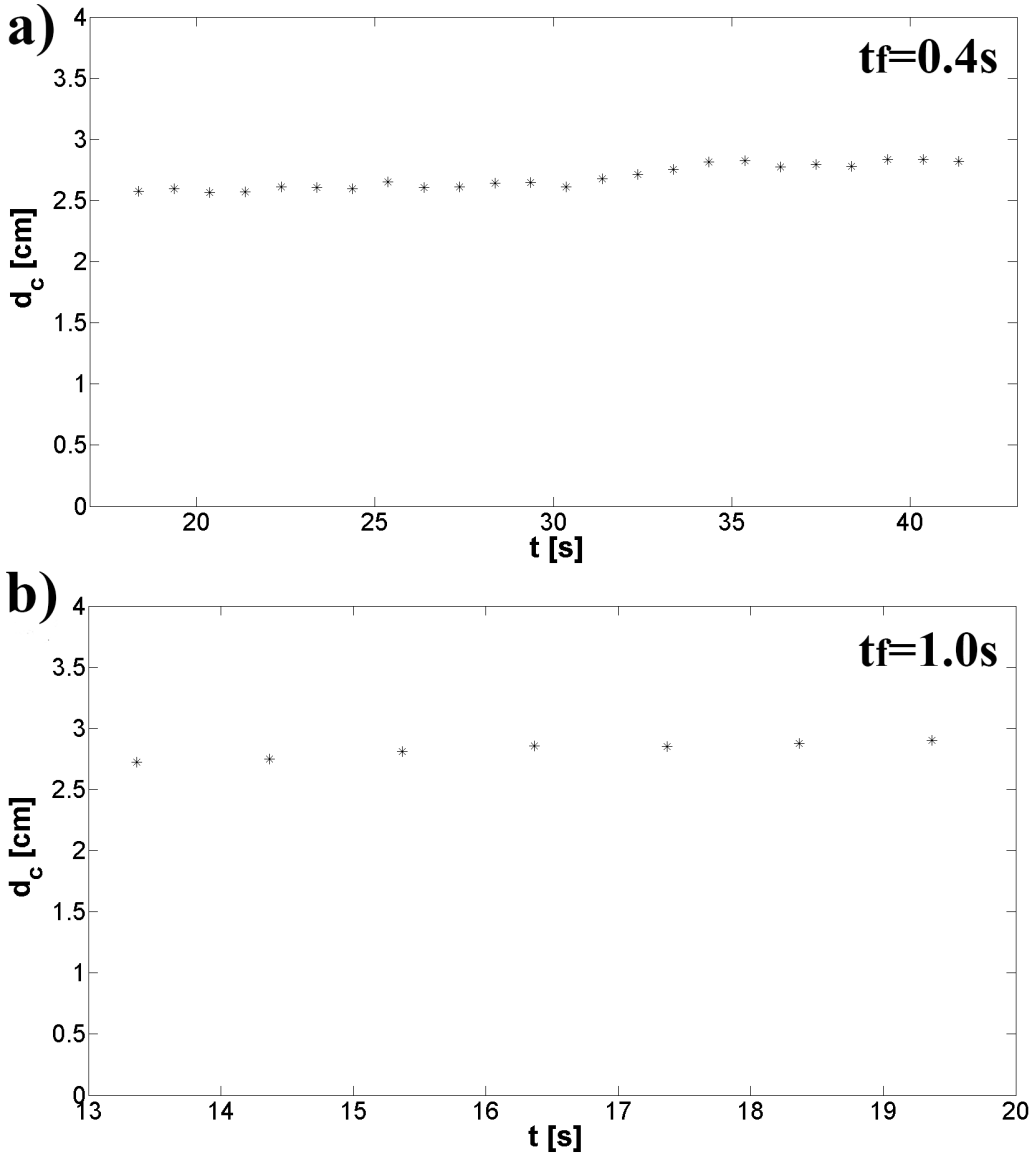

Figure 5.18: Experimentally obtained time evolution of d_c with constant forcing parameters $I = 1.0\ A$, $B = 0.51\ T$ and $d_e = 2.5\ cm$ but with different values of t_f: a) $t_f = 0.4\ s$, b) $t_f = 1.0\ s$.

5.7.1 The effect of varied parameters I, B and t_f on d_c

Figures 5.16, 5.17 and 5.18 show the experimentally obtained d_c as a function of time with varied I, B and t_f, respectively.

Measurement	d_c [cm]
$I_{t=32} = 0.4$ A	2.4
$I_{t=32} = 1.0$ A	2.7
$B_{t=35} = 0.25$ T	2.6
$B_{t=35} = 0.51$ T	3.0
$t_{f_{t=19}} = 0.4$ s	2.6
$t_{f_{t=19}} = 1.0$ s	2.9

Table 5.3: Experimentally obtained overview of d_c with varied forcing parameters I, B and t_f, respectively but compared at an identical time step.

The d_c has been calculated from Figures5.16, 5.17 and 5.18 and table 5.3 gives an overview of the results. The table shows small increases in d_c with higher values of I, B and t_f.

5.7.2 The effect of varied parameters d_e on d_c

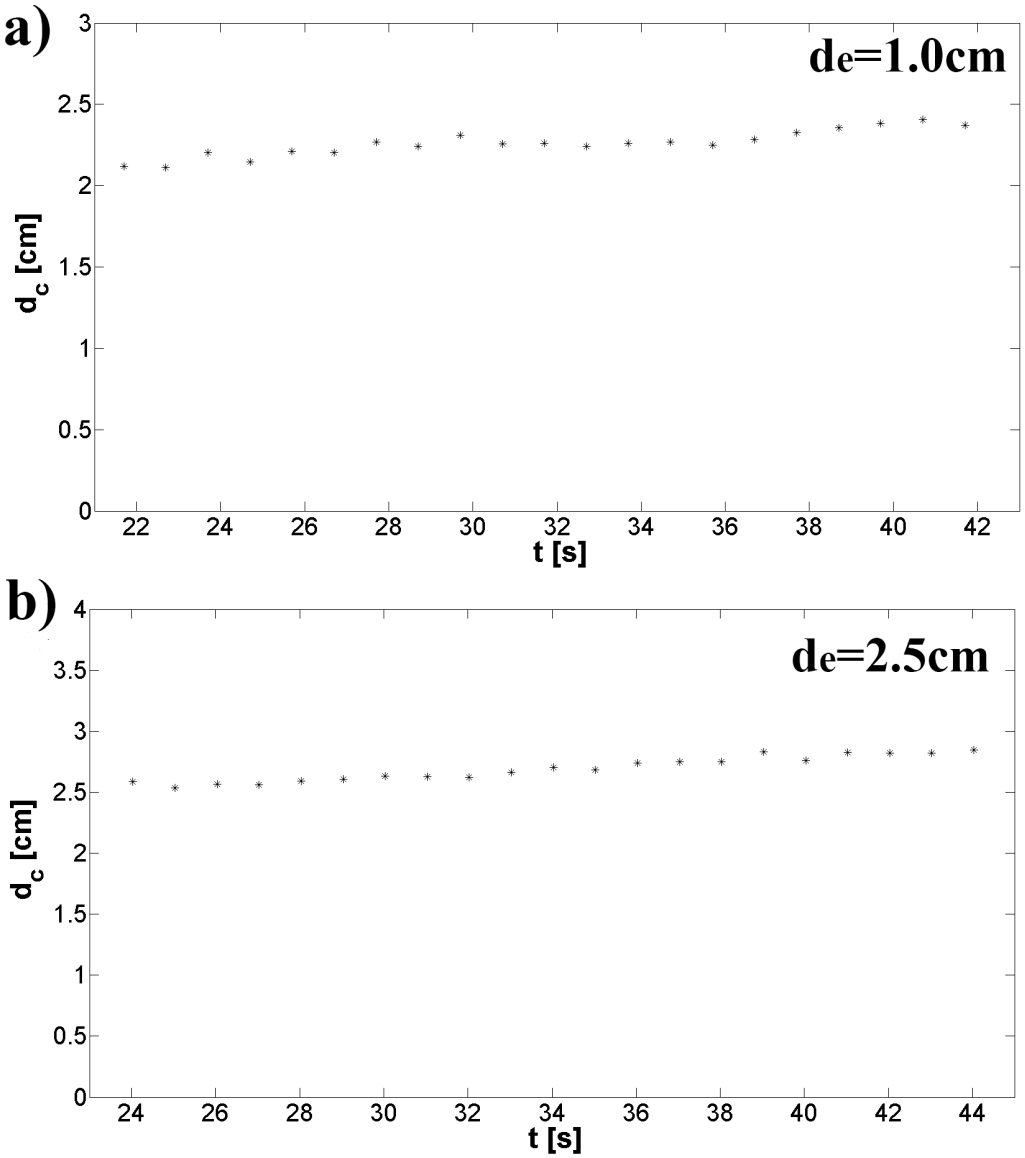

Figure 5.19: Experimentally obtained time evolution of d_c with constant forcing parameters $I = 1.0\ A$, $B = 0.51\ T$ and $t_f = 0.5\ s$ but for different values of d_e: a) $d_e = 1.0\ cm$, b) $d_e = 2.5\ cm$.

Figure 5.19a,b shows the experimentally obtained time evolution of $d_c(t)$ with $d_e = 1.0$ cm and $d_e = 2.5$ cm, respectively. Note that $d_c(t = 0) = d_e$ which is shown numerically in Figure 4.5.

d_e [cm]	$d_c(t=0)$ [cm]	$d_c(t=22)$ [cm]
1.0	1.0	2.1
2.5	2.5	2.6

Table 5.4: Table showing values of $d_c(t)$ corresponding to a specific measurement with d_e.

The d_c is measured with varied d_e at $t = 22$ s. Table 5.4 gives an overview of the results.

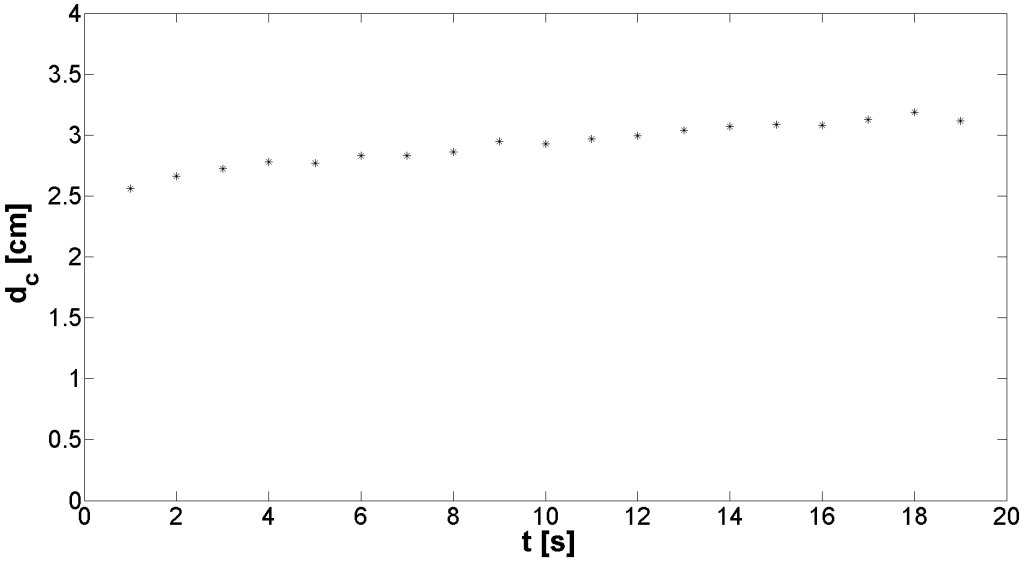

Figure 5.20: a) Graph illustrating the vortex core separation distance d_c with a large field of view. The electrode distance d_e is 2.5 cm.

Subsequently, another measurement is performed for d_e with a larger field of view to capture the time interval between $t = 0$ and $t = 22$ s. Figure 5.20 shows this measurement. Note that $d_c(t = 0) \simeq 2.5$ cm which is the electrode distance $d_e = 2.5$ cm.

Batchelor [11] found that by forcing fluid (Q2D) with a certain amount of linear momentum, a dipolar vortex will emerge with a specific 'equilibrium' size L_{eq}, depending on the linear momentum put into the fluid. This can be a possible explanation for the difference in d_c 'growth' as the equilibrium size L_{eq} corresponding to generated linear momentum ($(J \times B)t_f$) with forcing parameters $I = 1.0$ A, $B = 0.51$ T and $t_f = 0.5$ s can be close to 2.5 cm.

Therefore there are two factors that restrict the vortex size d_v (or d_c) which is:

1. the vortex size restriction due to d_e
2. The 'equilibrium' size L_{eq}.

In the interval between $t = 0$ and $t = 22$ s. For $d_e = 2.5$ cm the dipole already has a size close to the L_{eq} but for $d_e = 1.0$ cm this is not the case. Consequently, for $d_e = 1.0$ cm, the d_c starts to increase significantly more until it reaches the size L_{eq}.

To prove that for $L_{eq} \leq d_e$, d_e instead dominates the behaviour of d_c, a measurement with a decrease in linear momentum which decreases the corresponding L_{eq} is considered.
Figure 5.18a shows an experiment with lower generated linear momentum as there is a shorter t_f, comparatively. At $t = 18$ s, the d_c is about 2.6 cm which only deviates 0.1 cm from d_e.

Thus, if L_{eq} d_e then L_{eq}(linear momentum input) is important for the behaviour of d_c at early time stages.
If $L_{eq} \leq d_e$ then d_e is the important factor for d_c.

After a certain time, the horizontal (and vertical) diffusion of vorticity caused by viscous effects becomes dominant. This causes a relatively slow increase of d_c over time.

The diffusion of vorticity was investigated by Swaters [19] and Flór&van Heijst [7]. The diffusion of vorticity was caused by fluid entrainment at early time stages while at later timescales viscous effects become dominant. They suggested a linear time-dependency of d_c at later timescales.

5.8 The propagation speed of the vortex centre v_c as a function of time

The generated dipole propagates with a certain velocity v_c. The v_c is defined as the propagation velocity of the vortex centre. This propagation velocity has a time dependance as it decays because of viscous effects(bottom friction).
To investigate the propagation velocity of the generated dipoles in experiments, the PD and CL-models and their predicted propagation velocities are compared with the experimentally measured v_c.

The velocities of the PD and CL-dipole have an analytical expression as function of the circulation Γ. The CL-dipole velocity v_{CL} found by Flór and Van Heijst [7] and the PD velocity v_{pd} are respectively defined as follows:

$$v_{CL} = \frac{\Gamma}{2.362\pi d_c} \tag{5.7}$$

$$v_{pd} = \frac{\Gamma}{2\pi d_c} \tag{5.8}$$

with circulation Γ and the vortex core separation distance d_c.

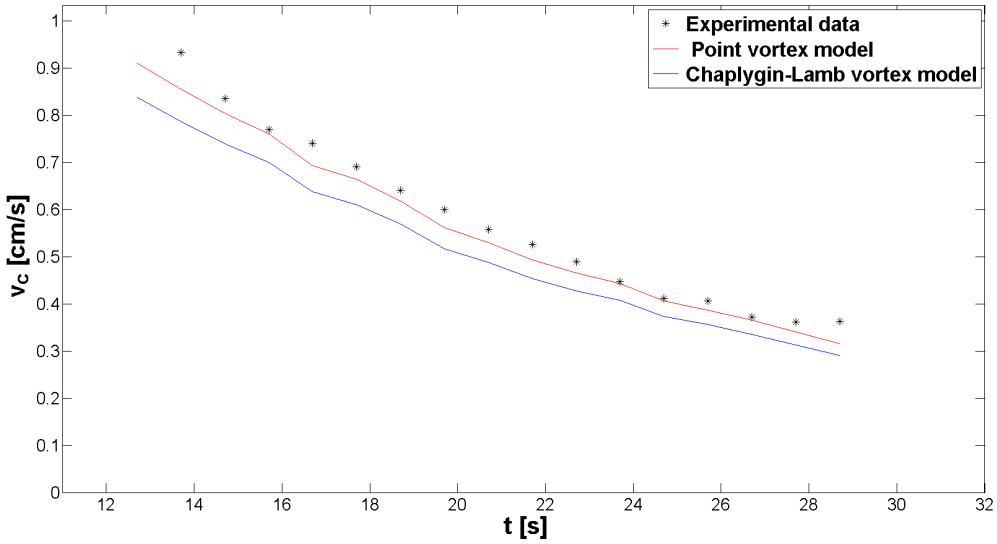

Figure 5.21: Experimentally obtained v_c over time. The red line indicates v_{pd} while the blue indicates v_{CL}. The forcing parameters are: $I = 0.5$ A, $B = 0.51$ T, $t_f = 1.0$ s and $d_e = 2.5$ cm.

The dipole propagation velocities of the PD v_{pd} and CL-dipole v_{CL}, are calculated through Γ the experimentally obtained circulation of the flow, using Equation (5.7) and 5.8). This done at each individual (experimental) measurement point indicated by the black markers as shown in Figure 5.21. The blue line and red-line represents the CL-dipole and PD, respectively. The velocity v_{pd} and v_{CL} are not obtained numerically.

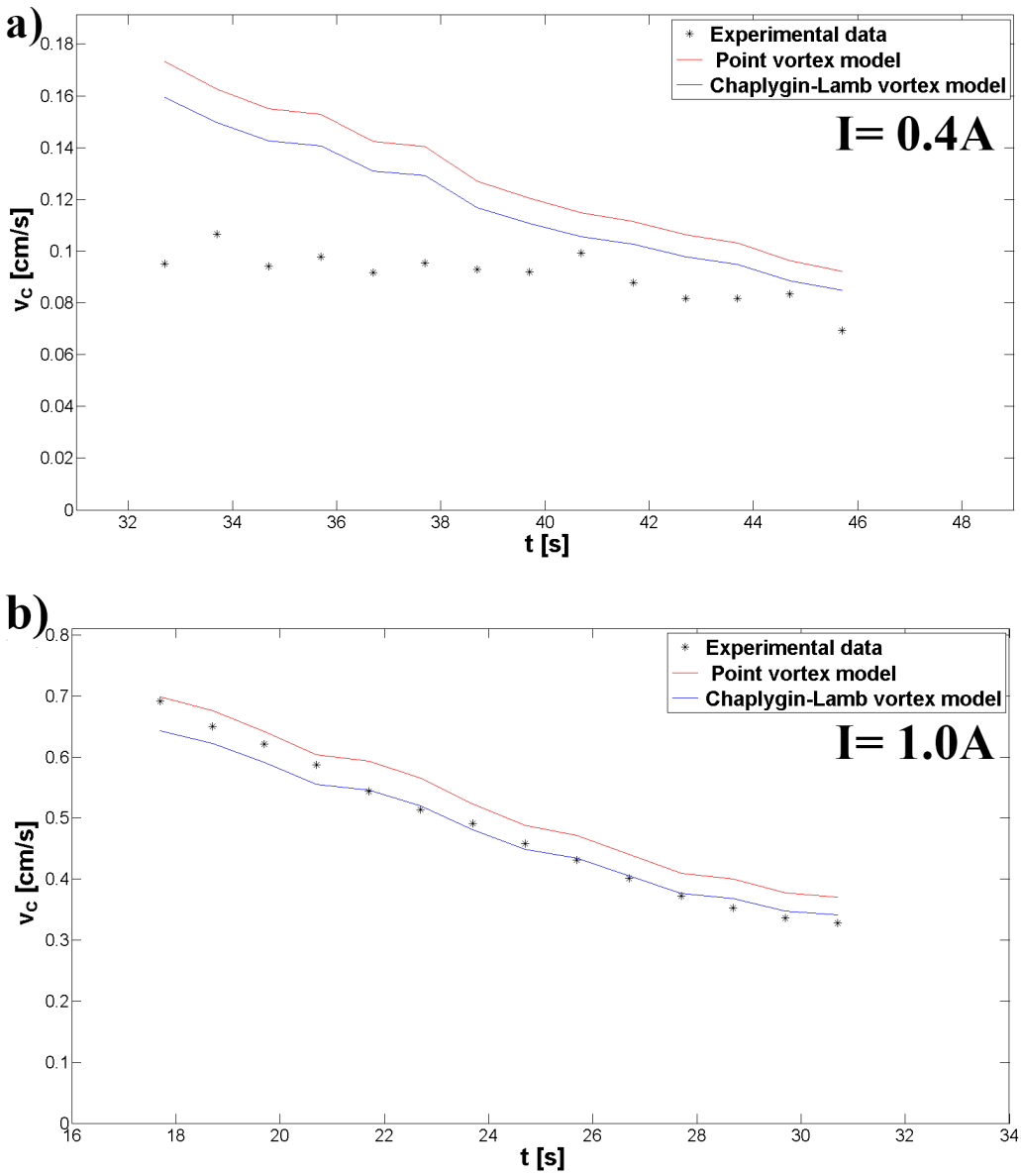

Figure 5.22: Experimentally obtained time evolution of v_c with forcing parameters $B = 0.51\ T$, $d_e = 2.5\ cm$ and $t_f = 0.5\ s$ but for different values of I: a) $I = 0.4\ A$, b) $I = 1.0\ A$. Additionally, the red line is the predicted propagation speed of the PD model while the blue line is the predicted propagation speed of the CL-dipole.

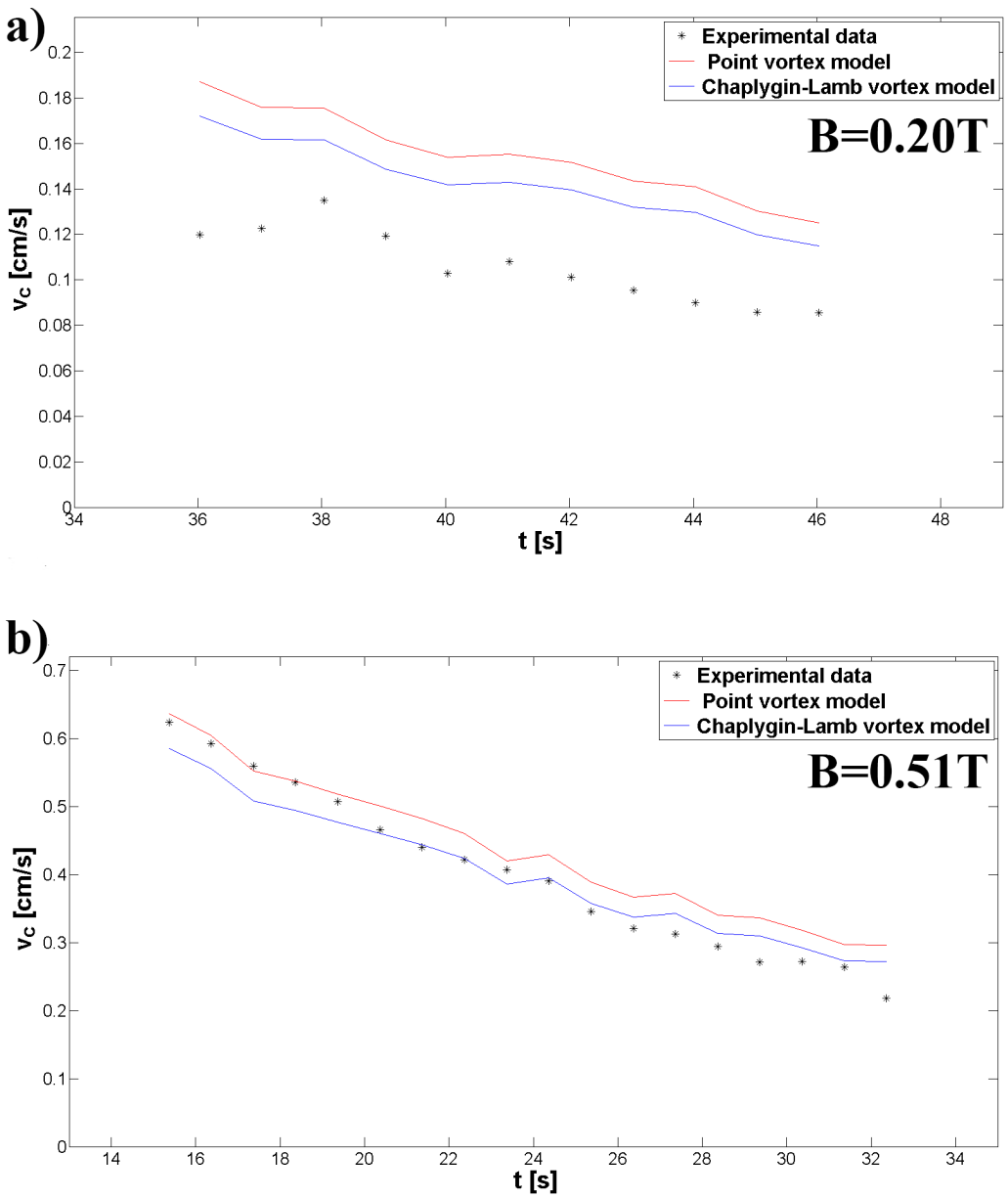

Figure 5.23: Experimentally obtained time evolution of v_c with forcing parameters $I = 1.0\ A$, $d_e = 2.5\ cm$ and $t_f = 0.5\ s$ but for different values of B: a) $B = 0.20\ T$, b) $B = 0.50\ T$. Additionally, the red line is the predicted propagation speed of the point vortex model while the blue line is the predicted propagation speed of the CL-dipole.

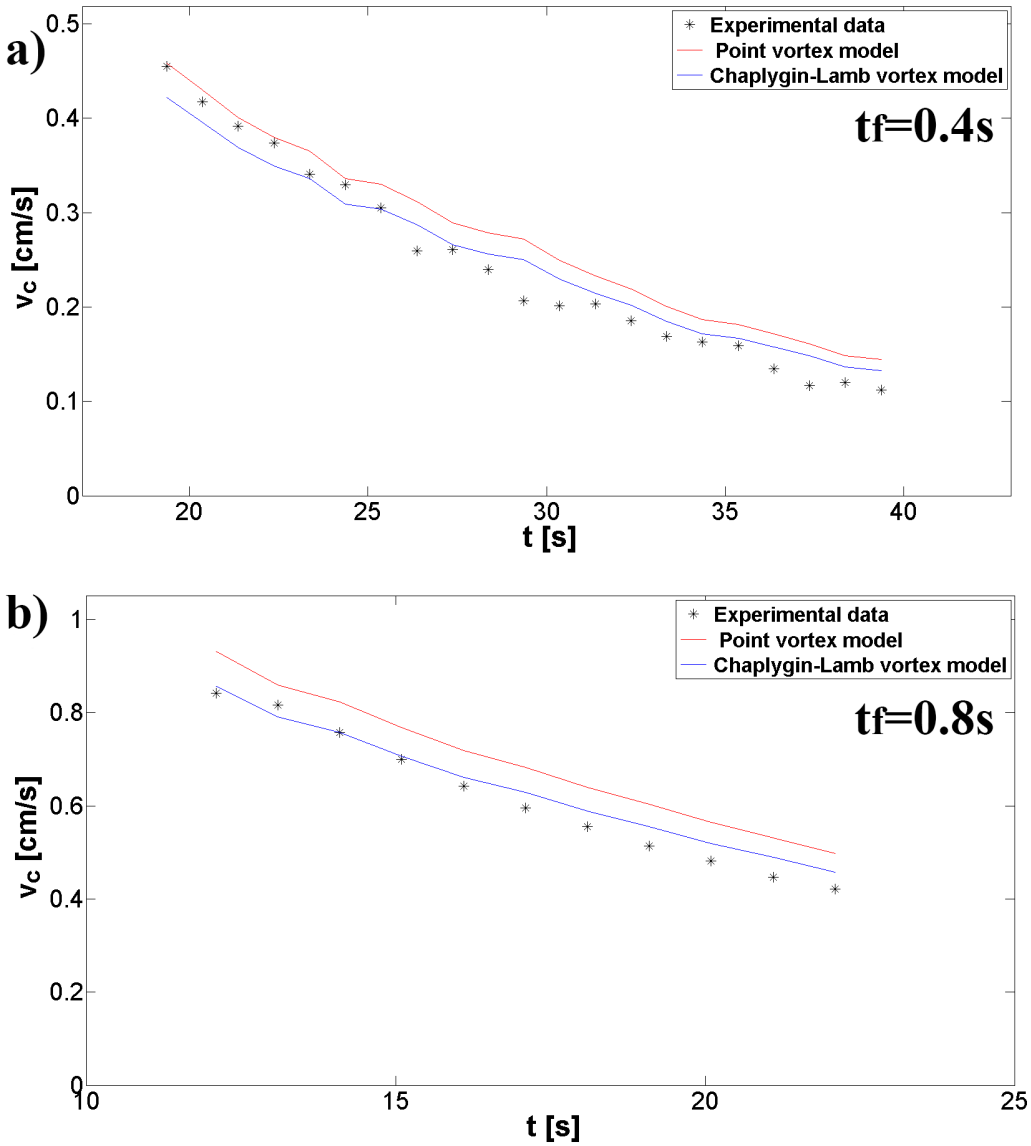

Figure 5.24: Experimentally obtained time evolution of v_c with forcing parameters $I = 1.0\ A$, $B = 0.51\ T$ and $d_e = 2.5\ cm$ but for different values of t_f: a) $t_f = 0.4\ s$, b) $t_f = 0.8\ s$. Additionally, the red line is the predicted propagation speed of the point vortex model while the blue line is the predicted propagation speed of the CL-dipole.

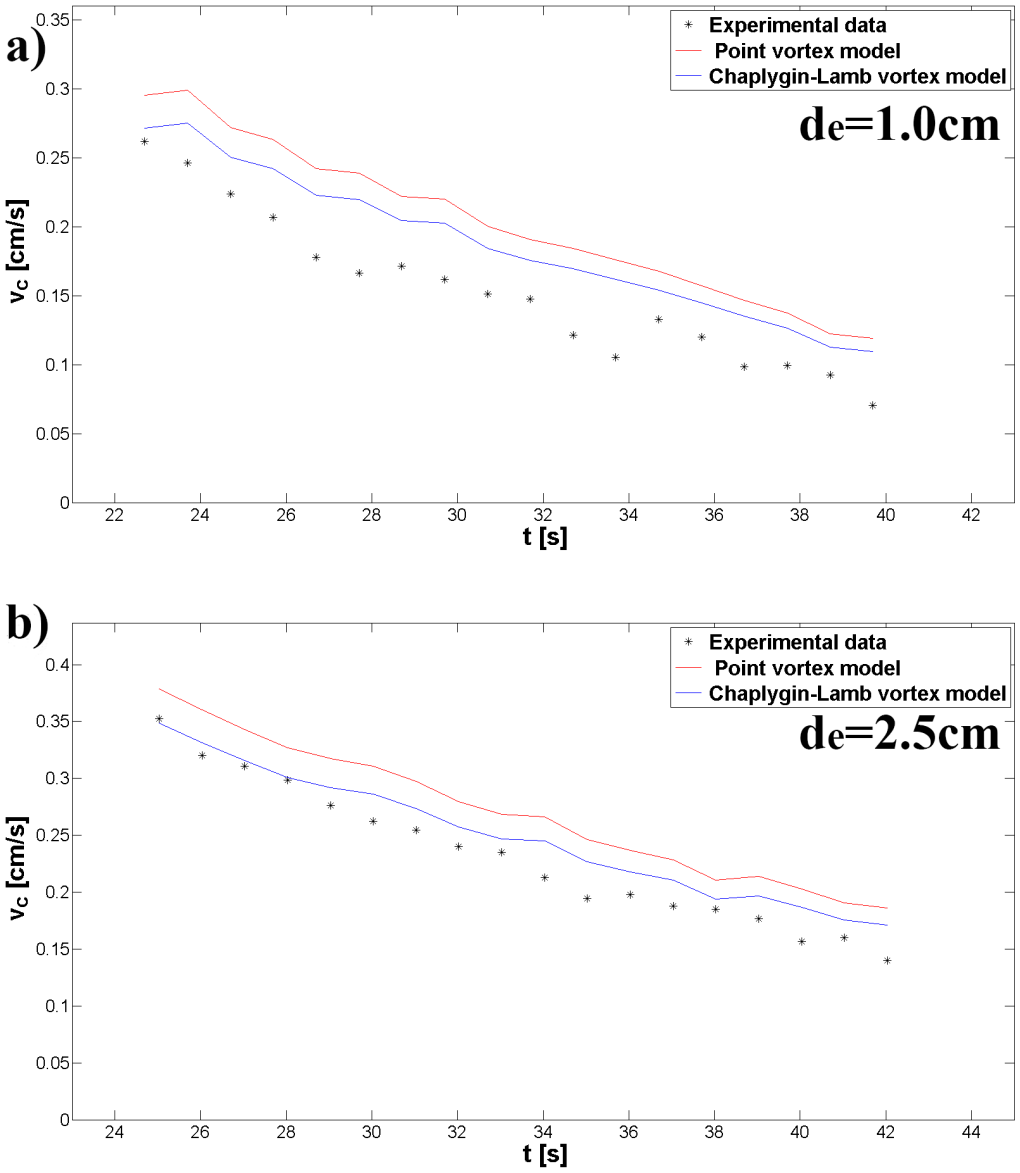

Figure 5.25: Experimentally obtained time evolution of v_c with forcing parameters $I = 1.0\ A$, $B = 0.51\ T$ and $t_f = 0.5\ s$ but for different values of d_e: a) $d_e = 1.0\ cm$, b) $d_e = 2.5\ cm$. Additionally, the red line is the predicted propagation speed of the PD model while the blue line is the predicted propagation speed of the CL-dipole.

The propagation velocity v_c over time is measured for various forcing parameters values. These are shown in Figures 5.22 (I), 5.23 (B), 5.24 (t_f) and 5.25 (d_e), respectively.

Figures 5.22 and 5.23 show a relatively large discrepancy between the experimental data and PD/CL predicted values. In contrast, the discrepancy is relatively small in Figures 5.24 and 5.25.

Figures 5.22a and 5.23a present measurements at a later time stage at $t \geq 32$ s. But the other measurements are performed earlier at $t \geq 15$ s.

The difference in discrepancy is due to the lower propagation velocities found at later time stages. Consequently, the flow at later time stages has a relatively low Reynolds number thus indicating that viscous effects are more dominant.
This explains the relatively larger discrepancy as the PD and the CL-dipole are inviscid models/solutions.

5.9 The ω-ψ scatter plots with varied forcing parameters

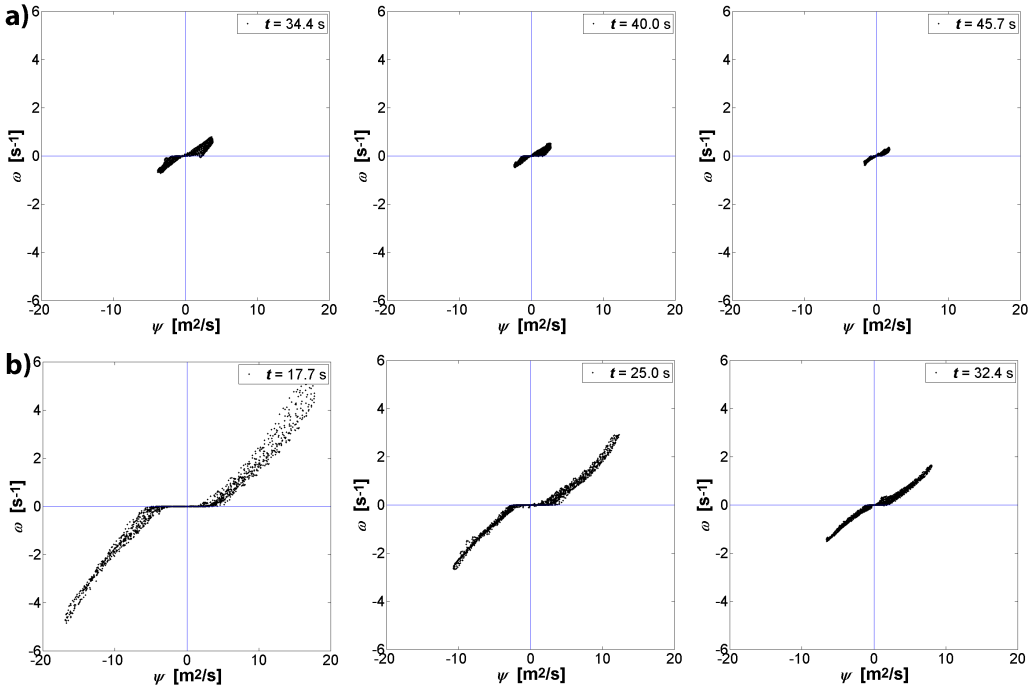

Figure 5.26: Experimentally obtained ω-ψ scatter plots with varied I: a) $I = 0.4\ A$ and b) $I = 1.0\ A$. The constant parameters are: $B = 0.51\ T$, $t_f = 0.5\ s$ and $d_e = 2.5\ cm$.

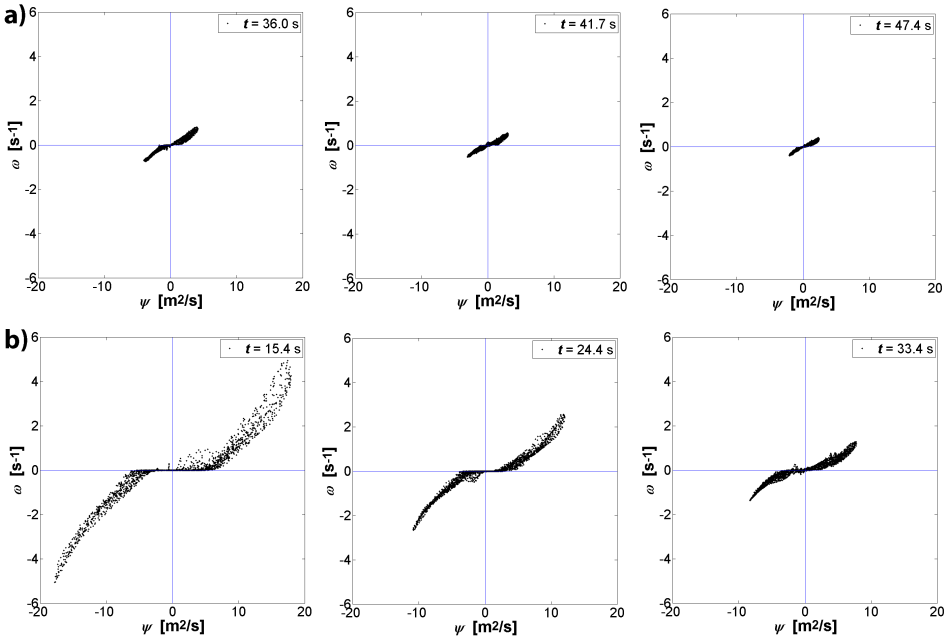

Figure 5.27: Experimentally obtained ω-ψ scatter plots with varied B: a) $B = 0.20\ T$, b) $B = 0.51\ T$. The constant parameters are: $I = 1.0\ A$, $t_f = 0.5\ s$ and $d_e = 2.5\ cm$.

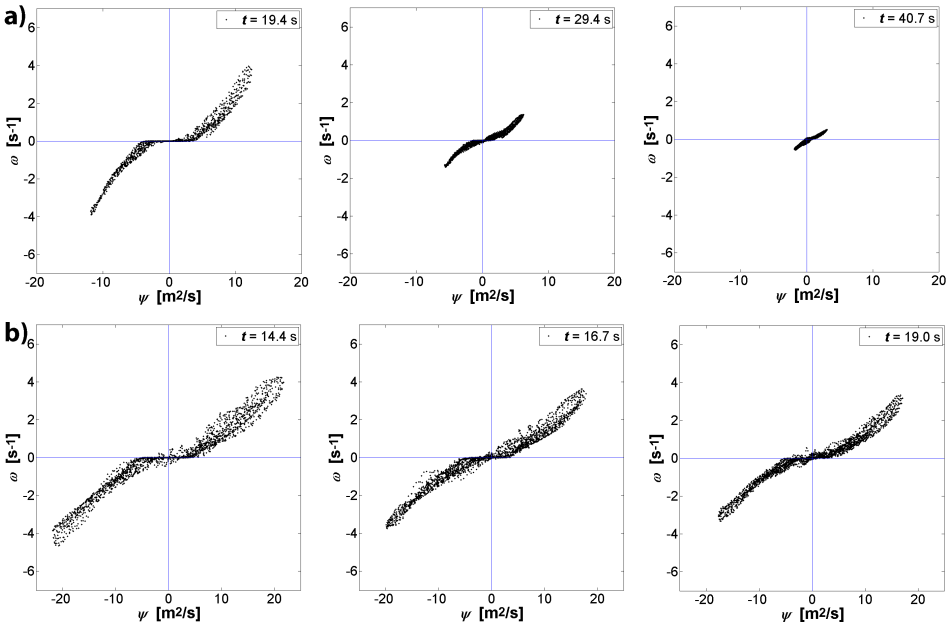

Figure 5.28: Experimentally obtained ω-ψ scatter plots with varied t_f: a) $t_f = 0.4\ s$, b) $t_f = 1.0\ s$. The constant parameters are: $I = 1.0\ A$, $B = 0.51\ T$ and $d_e = 2.5\ cm$.

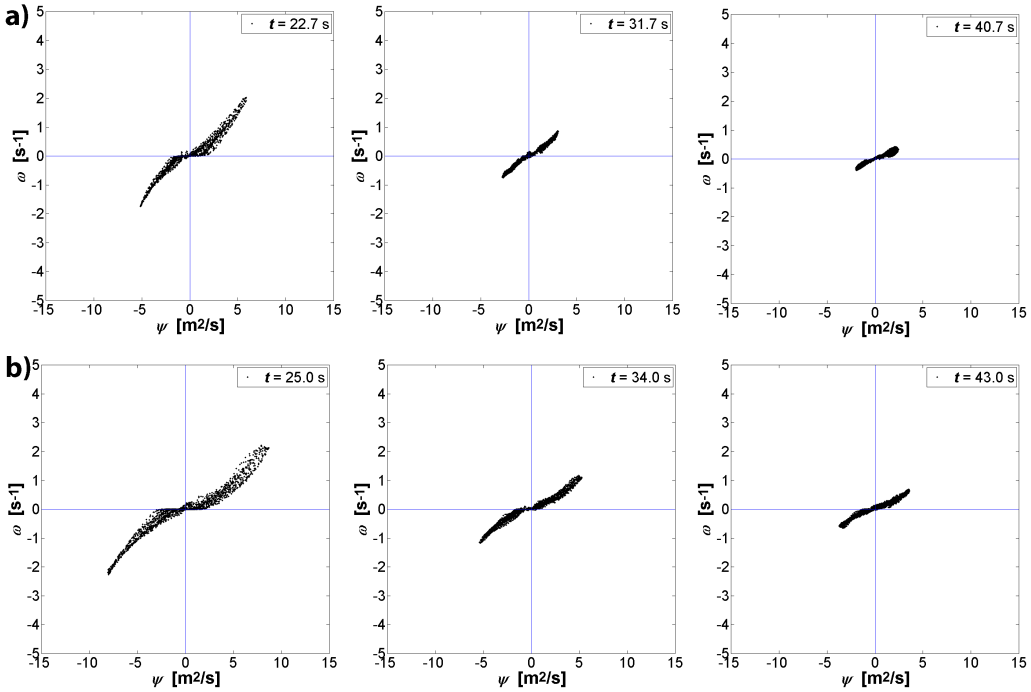

Figure 5.29: Experimentally obtained ω-ψ scatter plots with varied d_e and different point of time: a) $d_e = 1.0$ cm, b) $d_e = 2.5$ cm. The constant parameters are: $I = 1.0$ A, $B = 0.51$ T and $d_e = 2.5$ cm.

The vortex coherence can be analyzed using ω-ψ scatter plots in order to study the the dipolar vortex structure deformation over time.
Coherent vortices are vortex structures that do not deform over time. Analytically obtained ω-ψ relations generally have perfect vortex coherence as shown in Figures 2.1d and 2.1d. The experimentally obtained ω-ψ scatter plots are never perfectly coherent as experimentally generated dipoles exhibit time-dependent behavior.

The experimentally obtained ω-ψ scatter plots with varied forcing parameters are shown in Figures 5.26, 5.27, 5.28 and 5.29.
Although experimentally obtained ω-ψ scatter plots can never be perfectly coherent, however all the scatter plots show an asymmetry in coherence. The negative vorticity patch is relatively more coherent than the positive vorticity patch.

5.10 Asymmetry in coherence of the dipolar vortex cores

In Figures 5.26, 5.27, 5.28 and 5.29 one observes a recurring asymmetric coherence between the positive and negative vorticity patches. The negative vorticity patch is more coherent than the positive vorticity patch as it has less scattering. This asymmetry in coherence can be due to errors in PIV, asymmetric lighting of tracer particles resulting from data processing. The asymmetric situation can possibly be caused during the formation of the dipole or rather during the generation of vorticity as there is no known asymmetrical mechanism after forcing, which can be the cause of the measured asymmetry in the ω-ψ scatter plots.

5.10.1 The effect of the electric potential switch

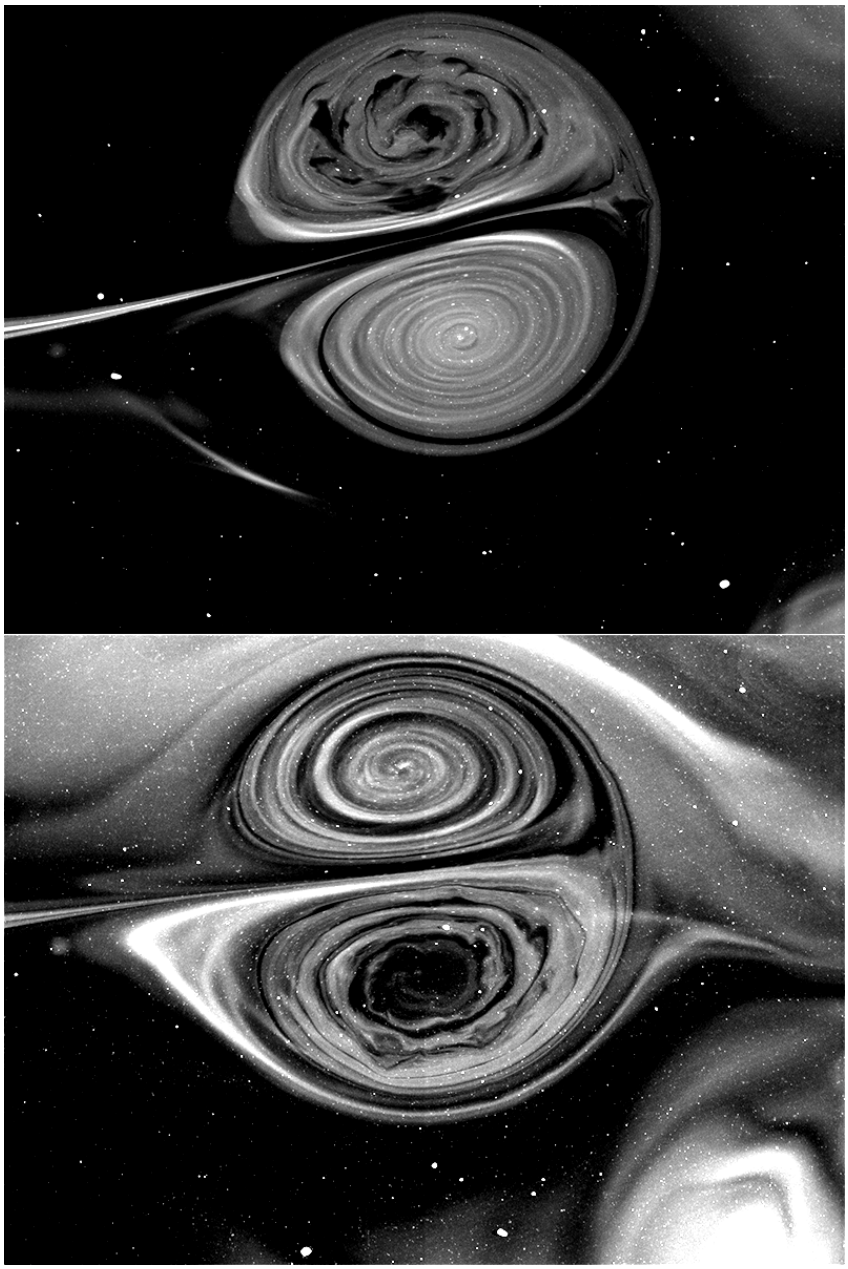

Figure 5.30: A pair of images which displays the difference when reversing the 'polarity' of the system. During the two experiments Fluorescein (yellow or green) is used to visualize the dipole. The darker spots in the 'disturbed' patch are red dye-particles.

The electrodes have opposite charge or polarity during forcing i.e. an electrode corresponding to the anode and the other to the cathode. Consequently there is an asymmetric distribution of chemical particles and possibly the occurrence of different chemical reactions locally.

Figure 5.30 shows two laminar dipolar vortices with disturbances in one vorticity patch while the opposite vorticity patch seems relatively undisturbed. The darker spots causing the disturbance are red coloured dye-particles at the free surface while the lighter dye are green coloured dye-particles. Because of gray-scale, the red particles can be confused with a region with no dye.

The red dye-particles are possibly a result of a chemical reaction that only occurs at one of the electrodes, thus only causing disturbances at the free surface of the vorticity patch generated at that specific electrode. This effect is not observed without the presence of (Fluorescein) dye in the vicinity of the electrodes during forcing.
This effect is also not observed when doing measurements with tracer particles instead of Fluorescein dye.

Orndorff and Hemmer [22] investigated Fluorescein and its derivatives where the yellow Fluorescein could be converted to red Fluorescein, which can be a possible candidate for the observed red dye-particles during this study. The chemical conditions for the conversion of the yellow Fluorescein into red Fluorescein were: a hot fluid with slightly acidic conditions. This might be a possible explanation of the effect of observing red particles, which affect the propagating dipolar vortex at the free surface as the current driven through the fluid can potentially raise the temperature and the salt solution: Na^+Cl^- and H_2O might provide H^+ (acidity).

5.11 Numerical simulations with varied dimensionless numbers C and Re

The numerical simulations are performed utilizing Comsol Multiphysics using the (laminar flow) 2-D fluid model.

The Reynolds number Re defined by equation (2.13) and electromagnetic forcing coefficient C defined by equation (2.12) play important roles in finding different parameter regimes. The numerical simulations are visualized using vorticity fields that are normalized as defined in equation (4.1).

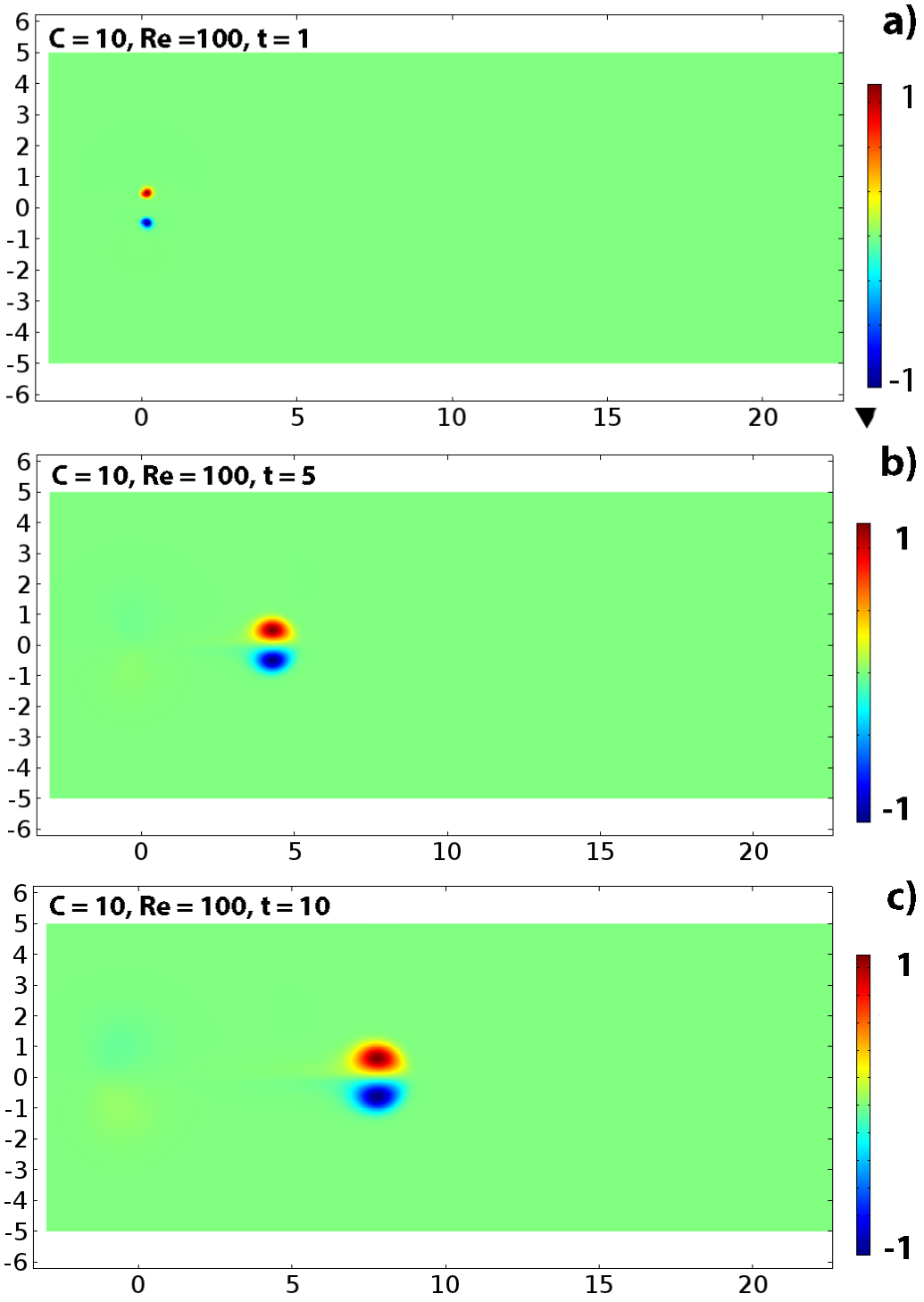

Figure 5.31: Numerically obtained snapshots of the dipole formation and propagation with $C = 10$ and $Re = 100$ at three time steps. The colour bar indicates the normalized vorticity ω^*. a) $t = 1$, b) $t = 5$ and c) $t = 10$ scaled in t_f.

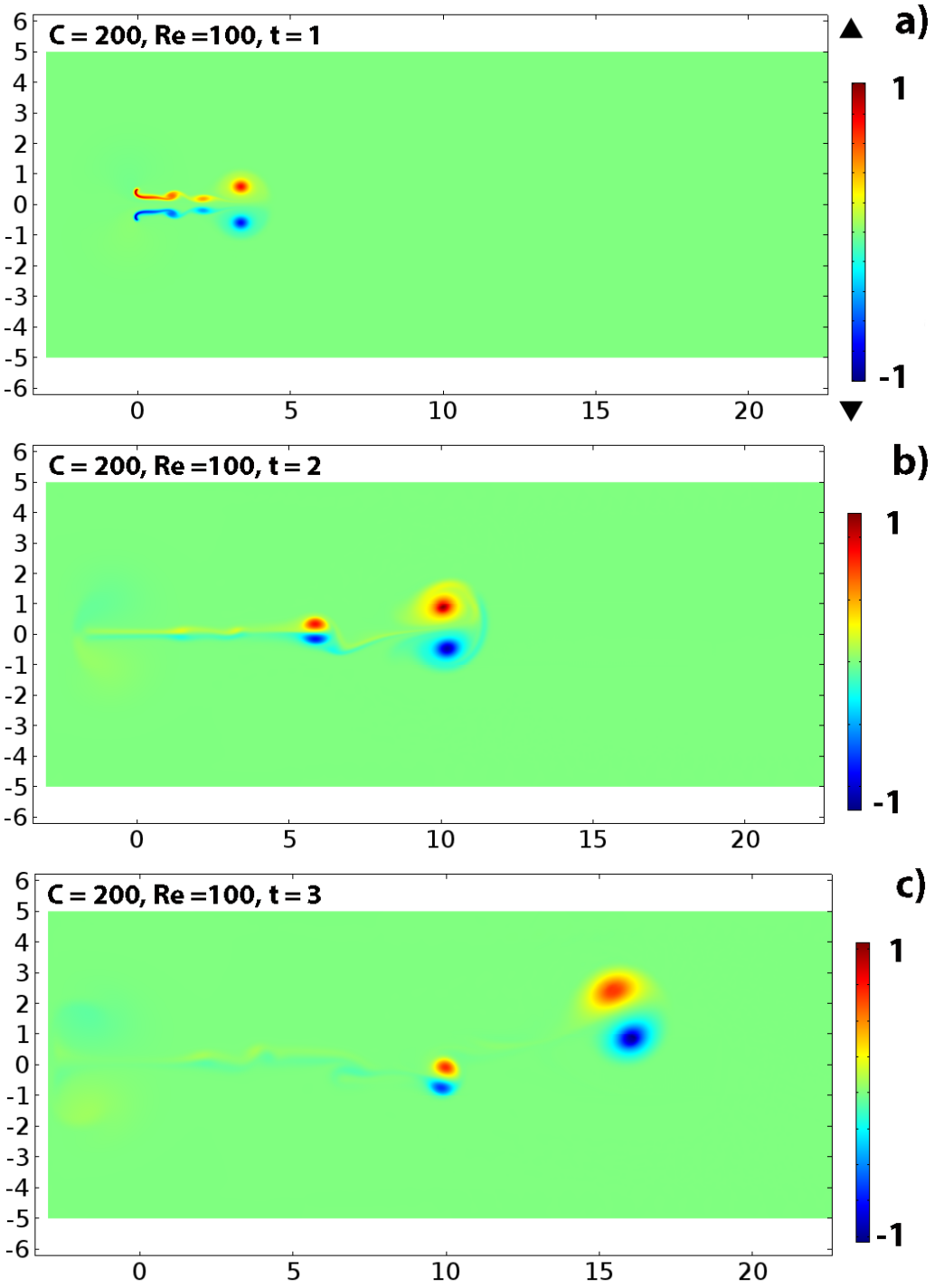

Figure 5.32: Numerically obtained snapshots of the dipole formation and propagation with $C = 200$ and $Re = 100$ at three time steps. The colour bar indicates the normalized vorticity ω^*. a) $t = 1$, b) $t = 2$ and c) $t = 3$ scaled in t_f.

5.11.1 The effect of varying C

The dimensionless electromagnetic forcing coefficient C is defined in equation (2.12): C= $I_0 B_0 t_f^2 . \rho H \alpha d_e^2$.

The coefficient C is varied in two simulations and vorticity fields are plotted at three time steps. These are shown in Figure 5.31 (C = 10) and Figure 5.32 (C = 200). At Re = 100 with C=10, the early propagation phase is relatively 'stable' while the early stage becomes unstable with C = 200. For C = 200 two dipoles are generated while for C = 10 only one is created.

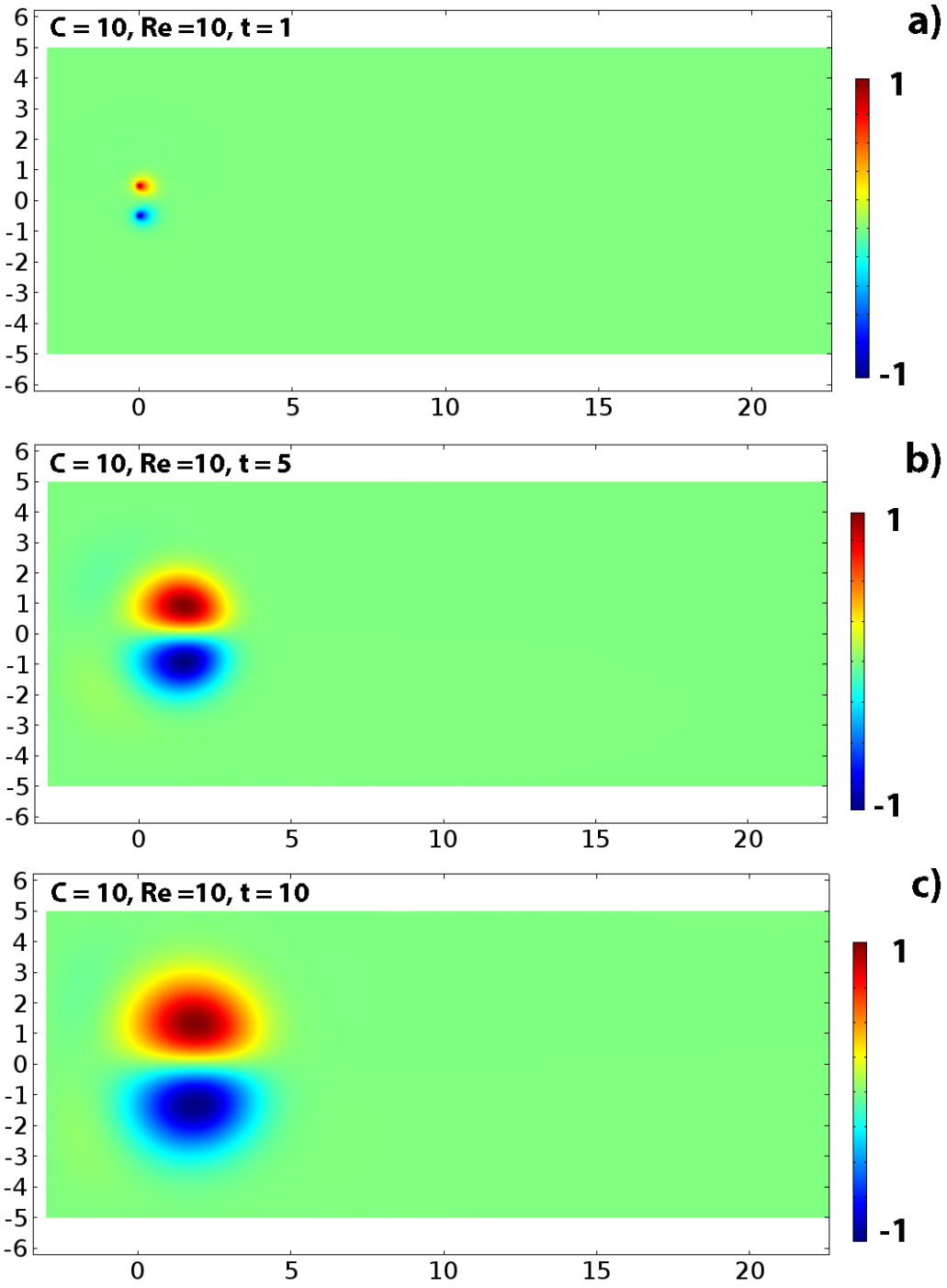

Figure 5.33: Numerically obtained snapshots of the dipole formation and propagation with $C = 10$ and $Re = 10$ at three time steps. The colour bar indicates the normalized vorticity ω^*. a) $t = 1$, b) $t = 5$ and c) $t = 10$ scaled in t_f.

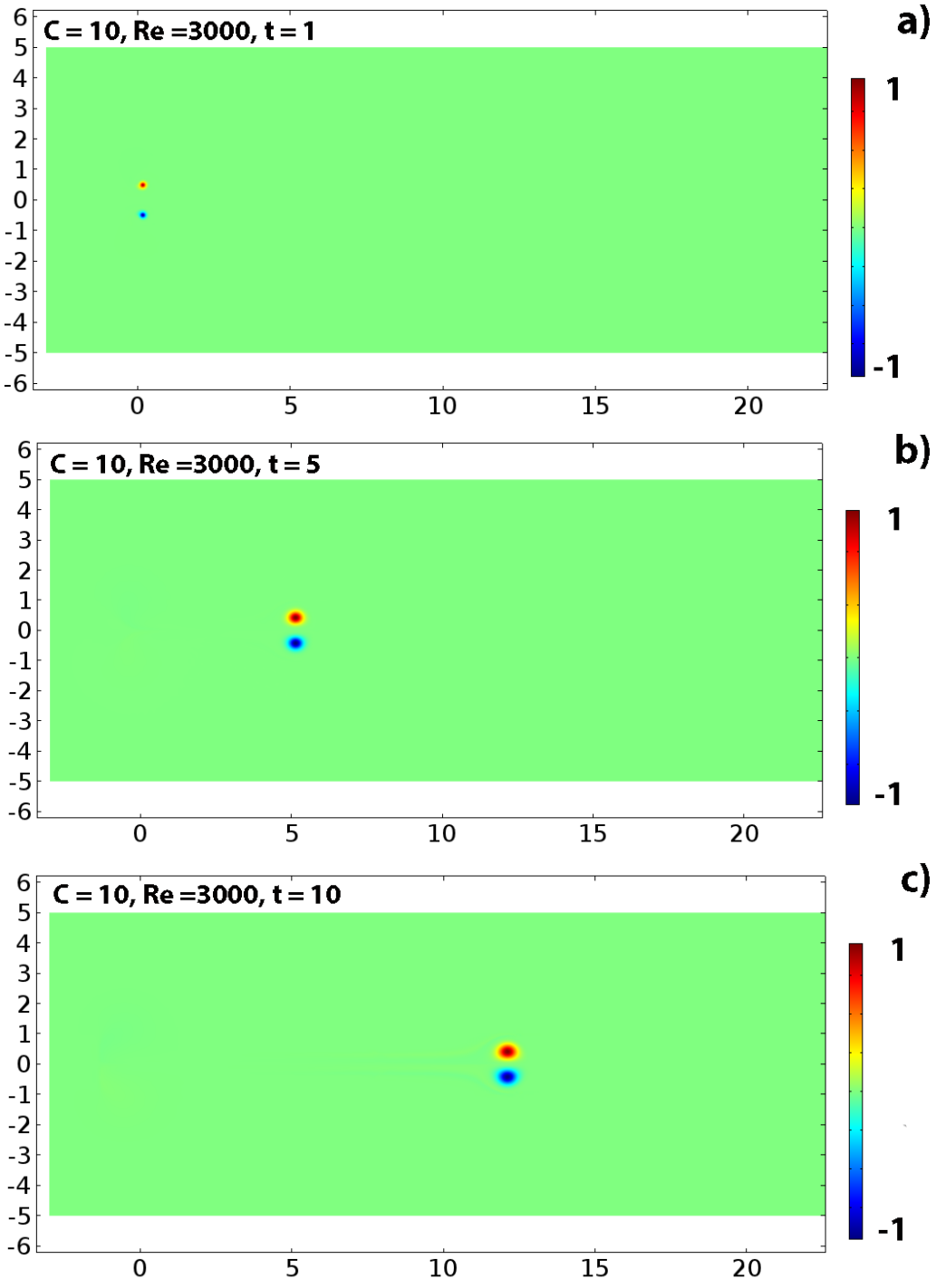

Figure 5.34: Numerically obtained snapshots of the dipole formation and propagation with $C = 10$ and $Re = 3000$ at three time steps. The colour bar indicates the normalized vorticity ω^*. a) $t = 1$, b) $t = 5$ and c) $t = 10$ scaled in t_f.

5.11.2 The effect of varying Re

The Reynolds number is defined in equation (2.13): Re= $d_e^2.\nu t_f$. The coefficient Re is varied in two simulations and vorticity fields are plotted at three time steps. These are shown in Figure 5.33 (Re = 10) and Figure 5.34 (Re = 3000). For C = 10 and low Re-values = 10, the dipole propagates very slowly and grows in size significantly. For high Re-values, the dipole only grows slightly in size but propagates much faster.

Chapter 6

Electromagnetically forced dipolar vortex collisions

The electromagnetic device and setup used during this study has a short experiment preparation time, which is in the order of a few minutes. Moreover, the device generates symmetric dipoles in addition to providing improved control over the forcing strength and the initial trajectory of the generated dipolar vortex. Dipolar vortex collisions provide a convenient way to illustrate this. Four cases are investigated:

1. The head-on frontal collision (no offset) of two identical dipoles
2. The frontal collision of two identical dipoles with an offset, with the aim to produce tripolar vortex-like structures;
3. Oblique dipole collisions;
4. Dipole collisions with a sharp edged wall;
5. Dipolar vortex collision with a sharp-edged gap in a simply connected domain.

6.1 Head-on frontal dipolar vortex collision

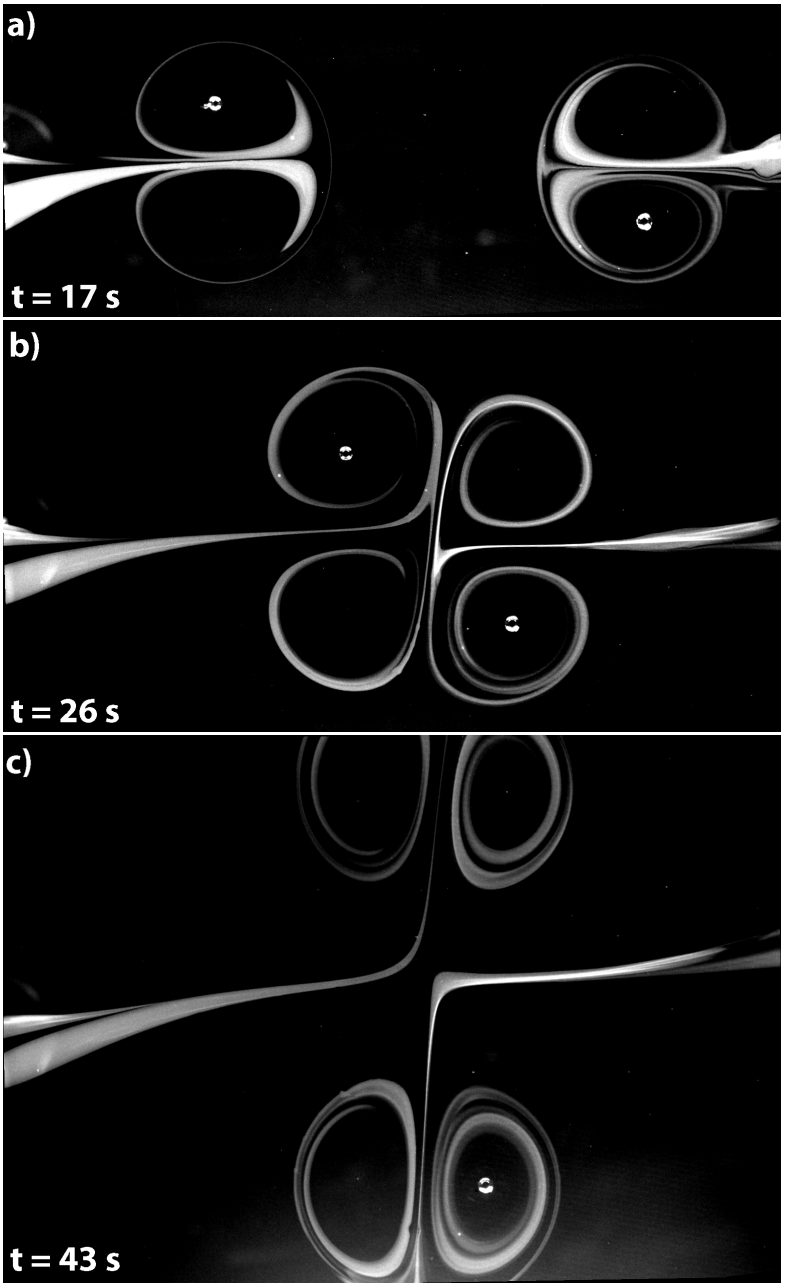

Figure 6.1: Dye visualization of a frontal collision of two dipolar vortices in gray-scale. The 90^o *deflection angle after collision indicates that the two dipoles had an (close to) equal strength with straight trajectories.*

Figure 6.1 shows an experimental observation of a head-on frontal collision between two dipolar vortices generated with the proposed device. The three images shown in Figure 6.1 have been re-sized to show the essential region of the collision in the the field of view. Figure 6.1a shows the two dipolar vortices approaching each other at a collision course, Figure 6.1b shows the collision of the dipolar vortices and Figure 6.1c shows the aftermath of the collision.

After the collision, two 'new' dipolar vortices emerge and the two initial dipolar vortex structures and the trajectories are symmetric. Consequently, the two emerging dipolar vortices exchange vortex cores and propagate perpendicularly with respect to the original trajectories.

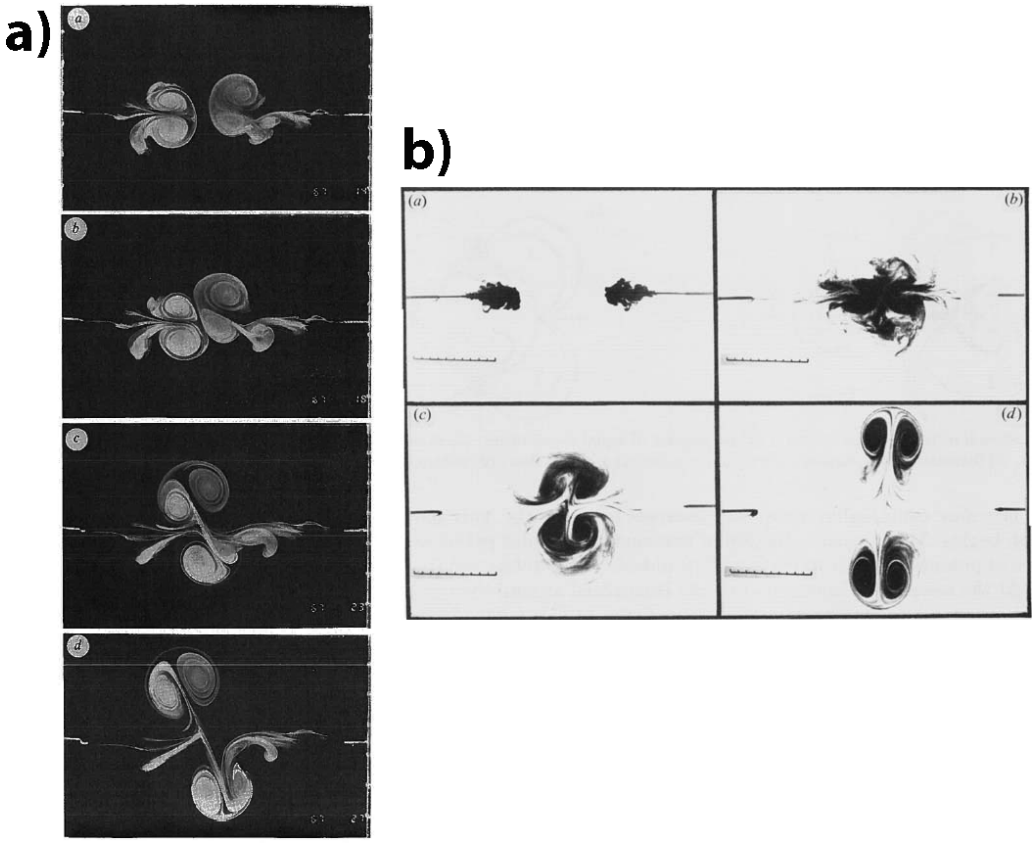

Figure 6.2: a) Figure illustrating a frontal collision of two dipolar vortices. Image courtesy of van Heijst and Flór [23]. b) Figure illustrating a frontal collision of two dipolar vortices. Image taken from Voropayev & Afanasyev [24].

Van Heijst and Flór [23] investigated dipolar vortex dynamics in a stratified fluid including a head-on frontal collision between two dipolar vortices shown in Figure 6.2a. In this study, the vortex dipole was generated using a syringe to inject fluid into the stratified fluid. This vortex generation method generally creates relatively asymmetric dipolar structures, which make the propagation trajectory less predictable and thus less reproducible.
The head-on collision was also investigated by Voropayev & Afanasyev [24] and the experimental observation obtained in that study are shown in Figure 6.2b. The setup is similar to the setup used by Van Heijst and Flór, with linearly stratified fluid and using a syringe-type device for generating dipoles.

6.2 Frontal dipolar vortex collision with offset

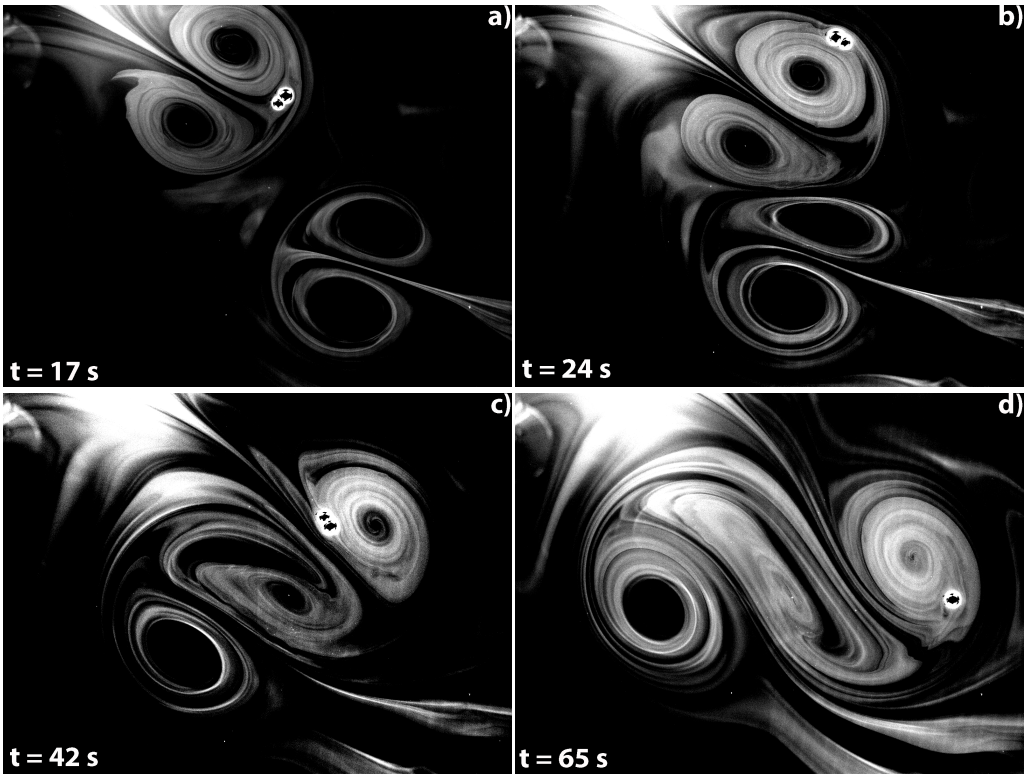

Figure 6.3: Dye visualization of an oblique collision of two dipolar vortices in gray-scale. a) shows the two dipolar vortices approaching each other. b) shows the start of the collision between the two dipolar vortices. c) shows the emergence of a tripolar vortex but this configuration is relatively unstable. d) the tripolar vortex starts to break up, where two 'new' dipolar vortices will propagate away from each other.

The frontal dipolar collision itself is interesting however if the collision is done carefully with a certain offset an (unstable) tripolar vortex can be created momentarily. Figure 6.3 shows snapshots of a dipole collision with a specific offset generated by the proposed device. Figure 6.3a shows the two dipolar vortices approaching each other. Figure 6.3b shows the start of the collision between the two dipolar vortices. Figure 6.3c shows the emergence of a tripolar vortex but this configuration is relatively unstable. In Figure 6.3d, the tripolar vortex starts to break up, where two 'new' dipolar vortices will propagate away from each other.

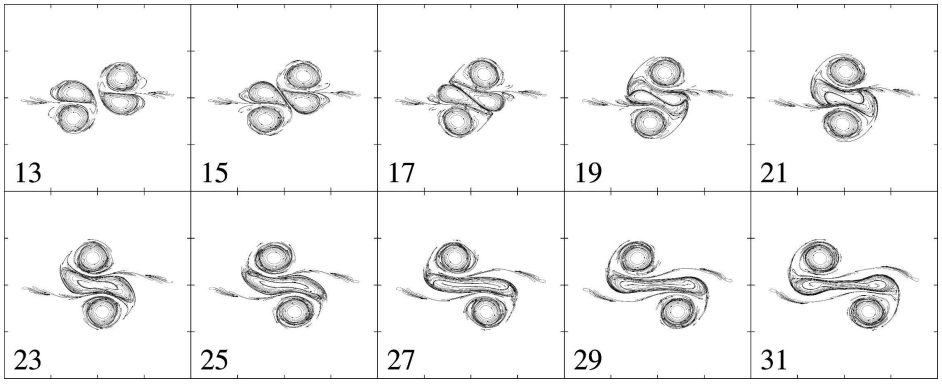

Figure 6.4: Figure illustrating a numerical collision of two dipolar vortices with an specific offset to a tripolar vortex. The dipolar vortices are visualized with potential vorticity. The time scale used in this figure is a advective time scale: $T = \frac{2\pi}{f}$, with f the Coriolis frequency. Image taken from Dubosq & Viúdez [25].

Figure 6.4 shows a numerical simulation of a tripolar vortex formed (temporarily) by a dipolar vortex collision performed in the numerical study by Dubosq & Viúdez [25].

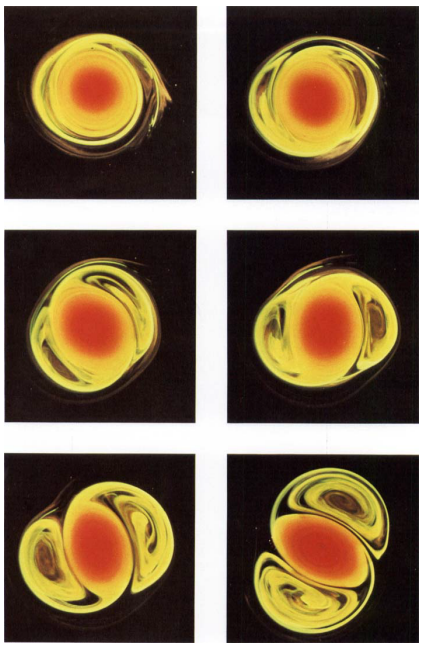

Figure 6.5: Figure showing a relatively stable tripolar vortex created using background rotation. Image courtesy of van Heijst et al. [26].

The formation of more stable tripolar vortex has been achieved in an experimental study by Van Heijst et al. [26]. Instead of using dipole collision, the tripolar vortex is created using a thin-walled cylinder placed at the centre of the setup with background rotation. The fluid inside the cylinder at the centre is stirred in the same rotational direction (cyclonic) as the background rotation and an isolated vortex emerges. This isolated vortex has a cyclonic vortex in the centre with a outer ring of anticyclonic vorticity. After the vortex is rotating in a stable fashion the cylinder is released swiftly. The formation of the tripolar vortex in this experiment is shown in Figure 6.5.

6.3 Oblique dipolar vortex collision

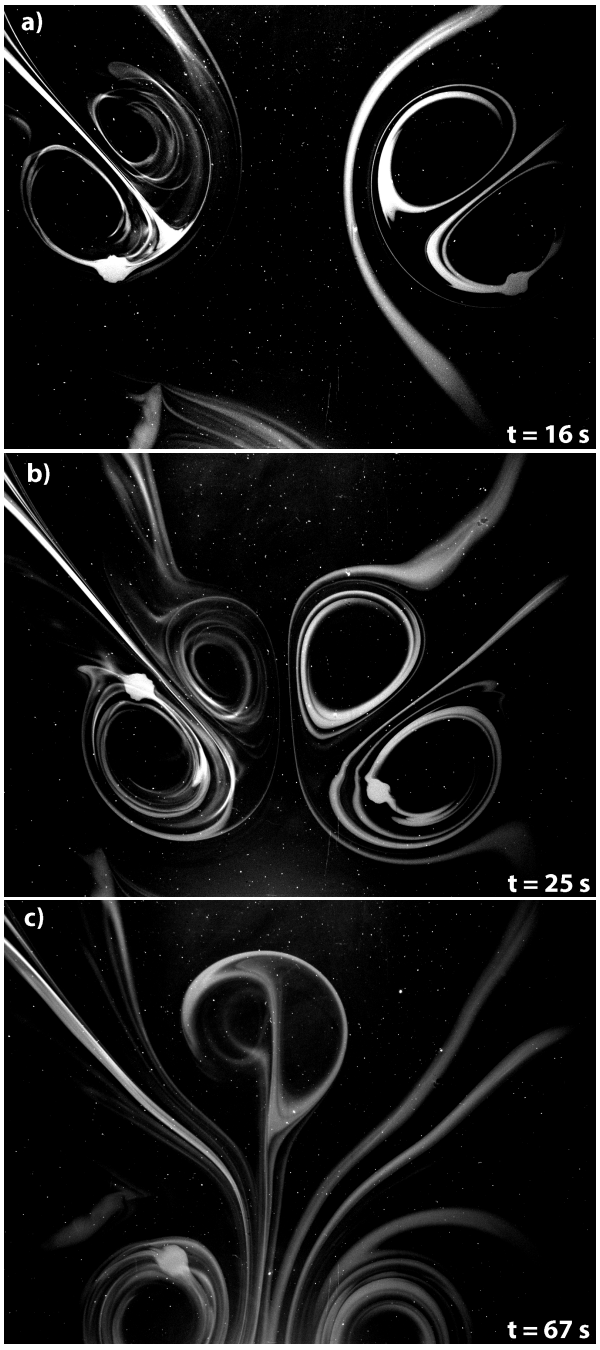

Figure 6.6: Dye visualization of an oblique collision of two dipolar vortices in gray-scale.

An experimental observation of the oblique vortex collision generated by the proposed device is shown in Figure 6.6. The initial stage where the two dipolar structures approach in an oblique collision course (the angle between the initial dipole trajectories is close to 90^0) is depicted by Figure 6.6a. Figure 6.6b shows the actual collision where the two dipolar structures come into contact and 'exchange' vortices. Figure 6.6c shows that the resulting 'upper' dipolar vortex is relatively small and compact while the opposite is true for the 'lower' vortex pair. The more compact upper dipolar vortex travels straight up, confirming the 90^o angle between the trajectories of the two initially symmetric vortex dipoles.

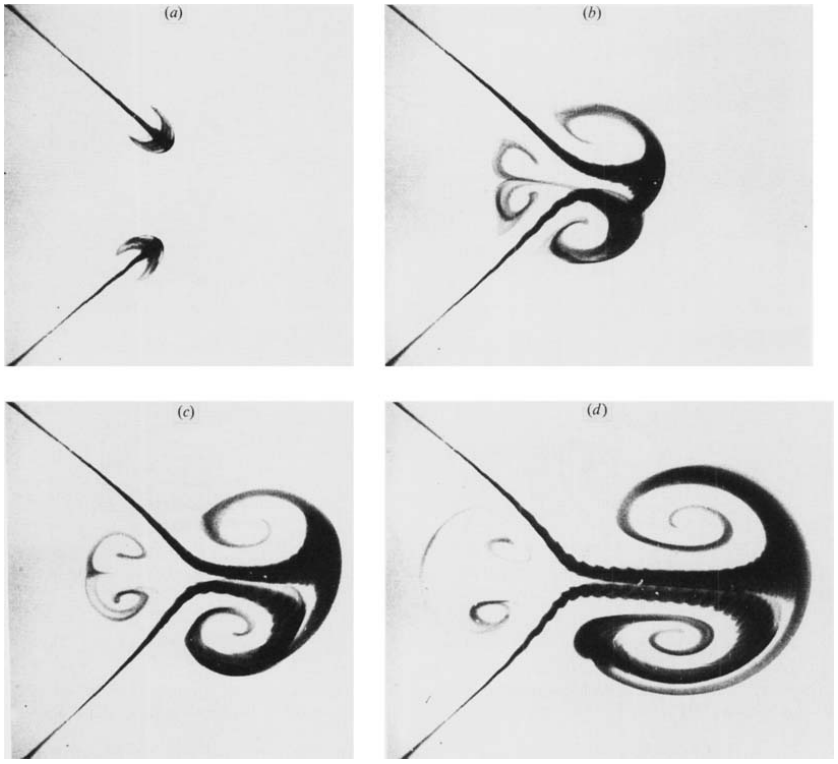

Figure 6.7: Figure illustrating an oblique collision of two dipolar vortices. Image taken from Voropayev & Afanasyev [24].

Voropayev & Afanasyev [24] have performed a study on dipolar vortex collisions in a stratified fluid, including frontal collisions but also oblique dipolar vortex collisions. Their experimental observation is shown in Figure 6.7. Their dipolar vortices are generated by injecting fluid into a stratified fluid utilizing a pair of syringes.

6.4 Dipolar vortex collision with a sharp-edged wall

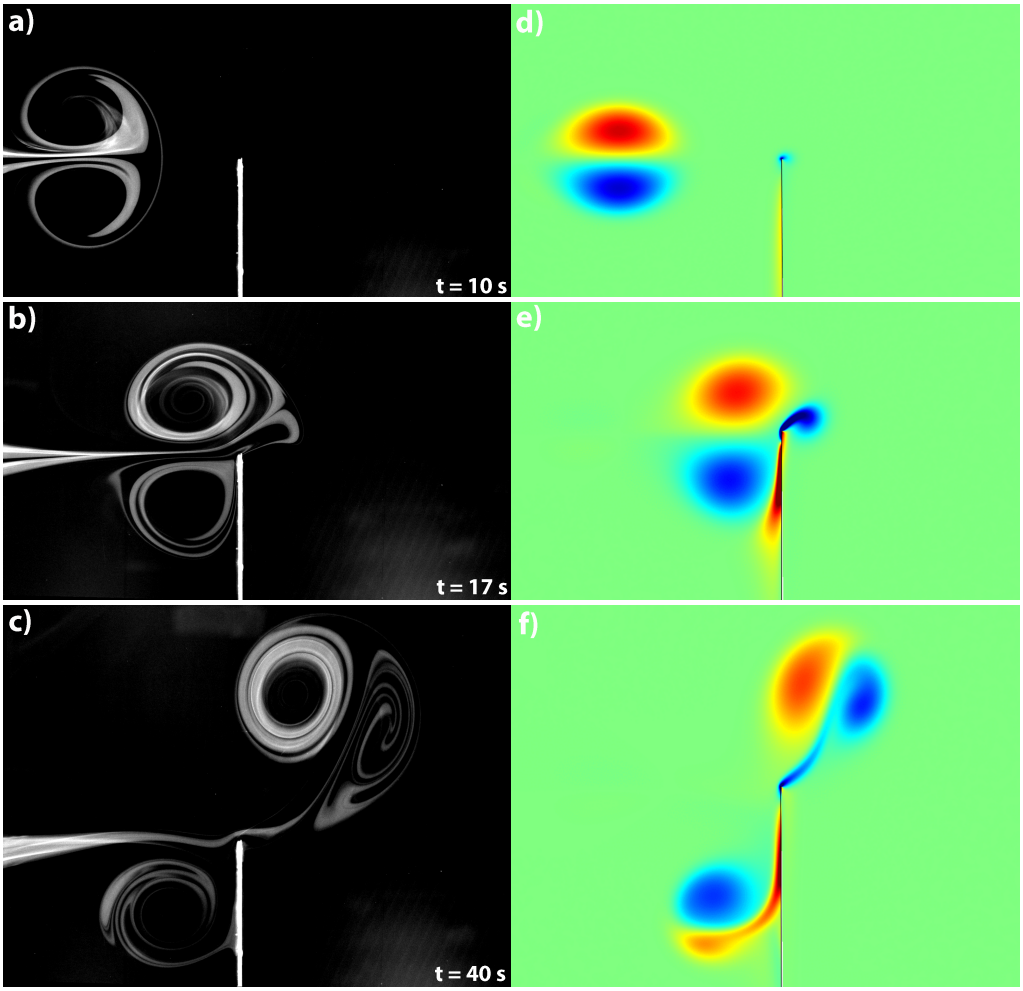

Figure 6.8: Dye visualization of a frontal collision of a dipolar vortex with a sharp edge with close to zero offset, in gray-scale. The colour plots show the numerically obtained vorticity time evolution of the collision between a dipolar vortex and a sharp-edge. Numerically obtained images courtesy of van Hooft [27].

The previous collisions considered two dipolar vortices colliding with each other, this section considers one dipolar vortex colliding with a sharp-edged wall. Figure 6.8a,b,c shows an experimental observation of the dipolar vortex-sharp-edged wall collision. Figure 6.8a shows the dipolar vortex approaching the tip of the sharp-edge. From this image a close to zero offset between the vortex centre and the sharp-edge tip is observed. This indicates the accuracy in which the dipole trajectory is controlled.

The actual collision is visible in Figure 6.8b where the dipolar vortex is deformed in an asymmetric fashion. This is due to the asymmetric geometry of the (sharp-edged) wall obstructing one half and with no obstruction in the other half with the region free of obstruction. The vortex dipolar vortex colliding with the sharp-edge wall generates secondary vorticity and results into two dipolar vortices propagating away from the wall. This is observed in Figure 6.8c, where two dipolar vortices are visible, the largest propagating 'upwards' and the smaller dipolar vortex in the vicinity of the wall propagating relatively slowly away. This asymmetrical geometry also affects the vorticity distribution of the two resulting dipolar vortices.

A numerical model of the collision is shown in Figure 6.8d,e,f. The flow is visualized with the vorticity field. Figure 6.8d shows the two dipolar vortex structures approaching. Figure 6.8e shows the collision and Figure 6.8f shows the resulting flow field after collision. The experimental observations and numerical simulation show similar behaviour qualitatively.

6.5 Dipolar vortex collision with a sharp-edged gap in a simply connected domain

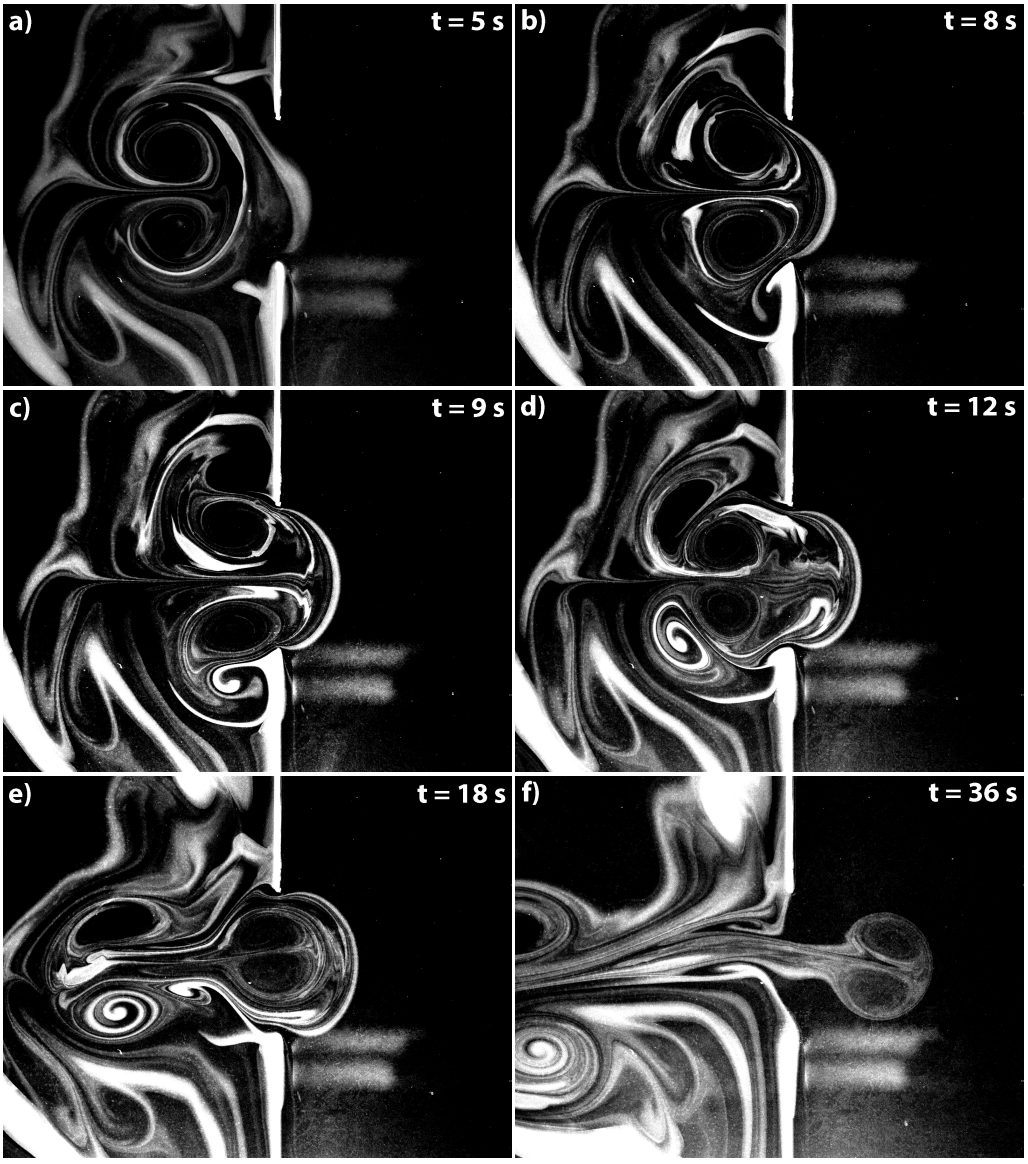

Figure 6.9: Figure showing a frontal collision of a dipolar vortex with a sharp-edged gap in a simply connected domain, in gray-scale.

Figure 6.9 shows a frontal collision of a dipolar vortex with a sharp-edged gap in a simply connected domain, visualized with dye. A simply connected domain means that the two walls/boundaries that create the gap are extended entirely towards the walls of the water tank, closing off/separating the tank into two halves. This is to ensure that there is no fluid flow in any region except through the shard-edged gap.

Figure 6.9 shows six snapshots of a dipolar vortex collision with a sharp-edged gap in a simply connected domain. Figure 6.9a shows a (primary) dipolar vortex approaching the sharp-edged gap. Figure 6.9b shows that this primary dipole cannot pass the gap but does advect/'push' some fluid through the gap however no vorticity is passed through. Figure 6.9c,d shows that secondary vorticity is created at the two sharp edges, similar to Figure 6.8. Two new (asymmetric) dipoles are created and 'rebound', following a curved trajectory where both collide. This collision is shown in Figure 6.9e which leads to vortex pair exhange. In Figure 6.9f, one dipole moves towards the left and the other propagates to the right-hand side towards the gap. The dipole that propagates through the gap is significantly smaller than the primary vortex shown in Figure 6.9a, which enables the passing-through.

Van Hooft [27] studied dipolar vortex collisions with a sharp-edged gap in a simply connected domain numerically. van Hooft concluded that a very well controlled environment is required in order to obtain a symmetrical result in an experiment; he was unable to perform experiments with sufficient symmetric results, which were conducted with a mechanical forcing mechanism in a rotating fluid (background rotation).

Figure 6.9 highlights the novel electromagnetic generation method's ability of generating symmetric dipolar vortices with improved control over dipole propagation trajectories.

Chapter 7

Vortex-shear interaction

7.1 Brief introduction

Atmospheric blocking is an example of a dipolar vortex structure. This structure can affect the weather and climate in the surrounding region for a prolonged time. A deforming background flow can influence the stability of this blocking structure. In order to investigate the stability of dipolar vortices, the dipolar vortices are subjected to a deforming background flow i.e. a shearing background flow.

7.2 Experimental setup: Dipolar vortex and shear flow interaction

The interaction between a vortex dipole and a shear flow is investigated experimentally. As a first step, a mechanical piston mechanism is used similar to mechanism used by Fernandes et al. [10].
The experimental setup to investigate the interaction consists of a water tank with length $L_1 = 200$ cm, width $W_1 = 100$ cm and the tank is filled with a two-layer stratified shallow fluid with a total fluid depth $H = 8$ mm, in order to promote a Q2D flow.

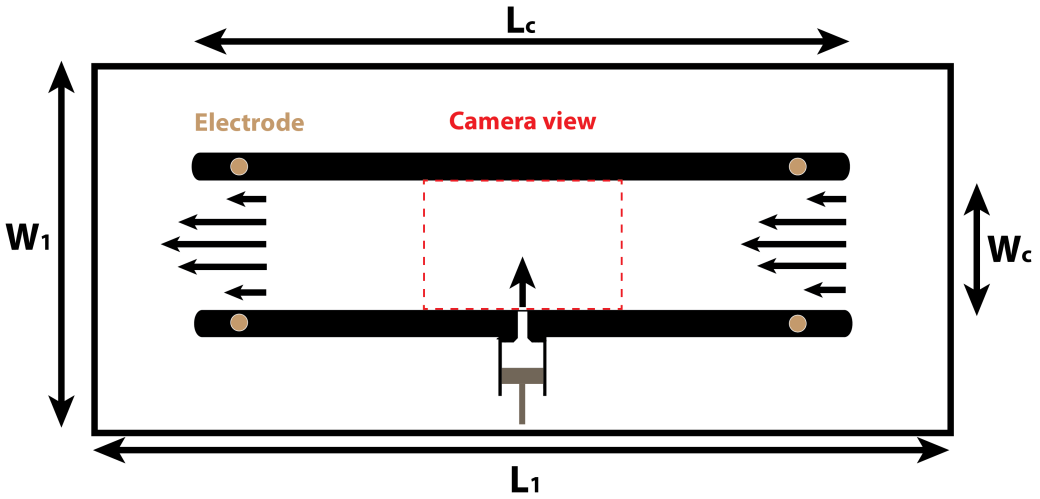

Figure 7.1: A sketch showing the top-view of the setup in which the interaction of dipole with a shearing background flow is studied. The two channel walls are sketched as two black bars. The direction of the shear flow is also indicated. The mechanical piston system responsible for injecting fluid into the channel is also visible in the lower part of the sketch.

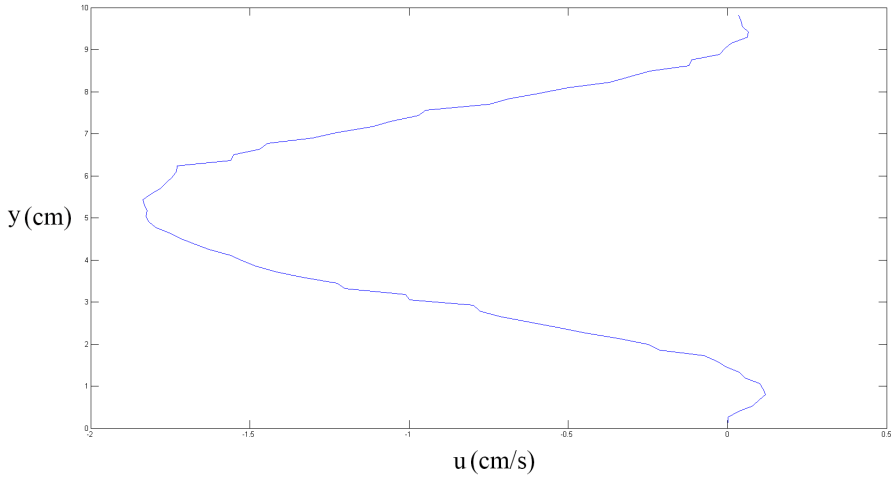

Figure 7.2: Experimentally obtained velocity profile of the shearing background flow.

Figure 7.1 shows a sketch illustrating the top view of the experimental setup. Electromagnets are installed beneath the water tank and electrodes are installed at the channel walls in order to generate a magnetic field and electric current to maintain a shear flow in the fluid present in the channel.

The piston injects fluid perpendicularly to the shear flow propagation direction. The fluid is injected at the centre of a channel where the shear flow has a Poiseuille-like profileas illustrated in Figure 7.2. The velocity profile of the shear flow has a negative direction close to the channel walls.

The mechanical generator consists of two parts, a piston which pushes fluid into the injector front piece. This front piece is a narrow corridor where the fluid goes through and then moves outwards into the channel as a jet. This jet is initially turbulent but soon a dipolar vortex structure is formed.

There are two cases of dipolar vortex-shear interaction are investigated. These are the perpendicular fluid injection and fluid injection at an angle, into the channel.

7.3 Perpendicular fluid injection

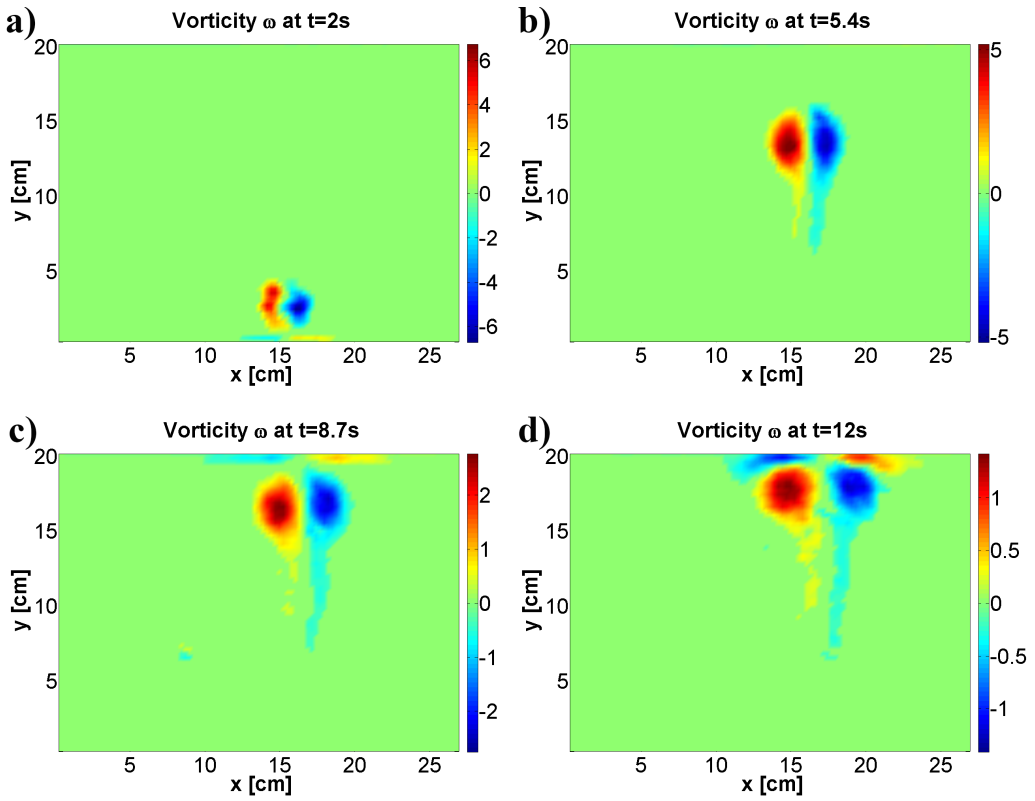

Figure 7.3: Experimentally obtained time evolution of a perpendicular dipole injection without a shearing background flow that is created through injection of luid through the lower channel wall and perpendicular to it: a) The dipole formation starts with secondary vorticity created at the lower channel wall, b,c) The dipole moves in a straight trajectory from the lower channel wall to the upper channel wall and d) the dipolar vortex collides with the upper wall creating secondary vorticity close to the upper channel wall.

Fluid is injected into the channel perpendicularly with respect to the wall and a jet of fluid is created. Subsequently a dipolar vortex structure emerges. In the absence of a background flow, the dipolar vortex propagates along a straight-line trajectory from the lower channel wall towards the upper channel wall. The vortex dipole can collide with the upper channel wall, depending on the injection volume and speed.
The subsequent formation and propagation of the dipolar vortex without a background flow is shown in Figure 7.3.

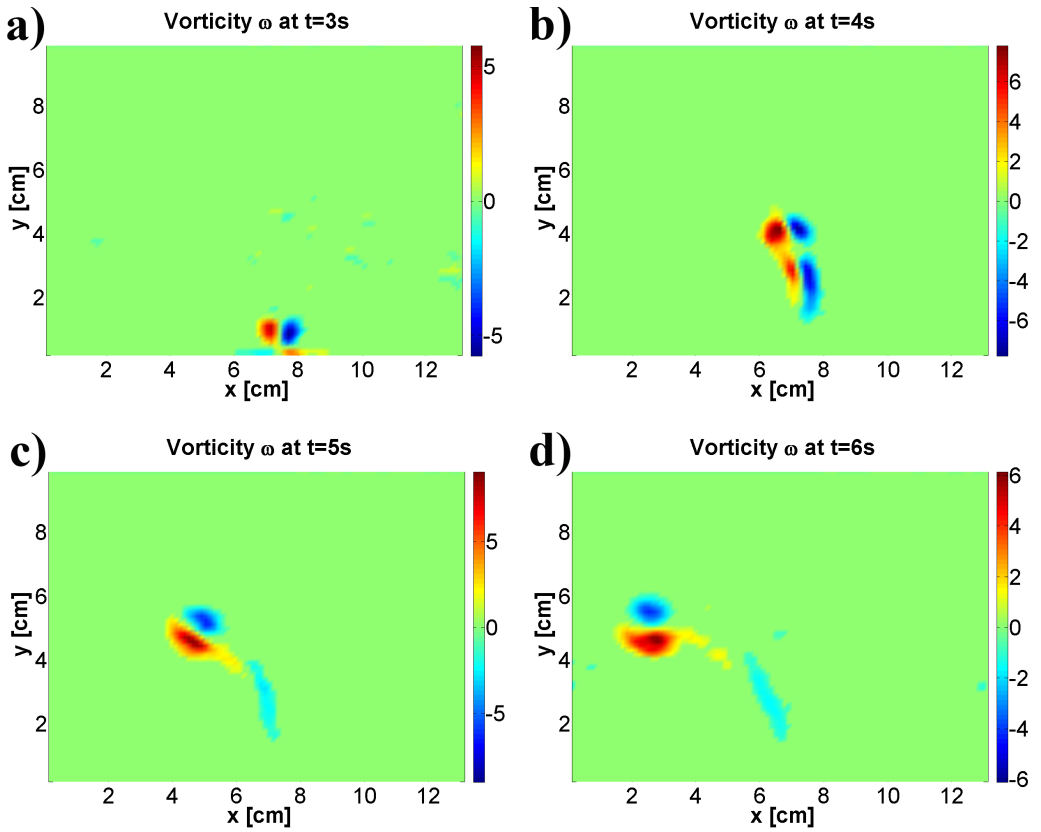

Figure 7.4: Experimentally obtained time evolution of a perpendicular dipole injection into a shearing background flow: a) The fluid is injected and the dipole is starting to form, note that the (opposite) secondary vorticity at the lower channel walls are also visible, b) The formation process is finalizing and the shear-flow is starting to advect the dipole structure in the direction along the channel. c) and d) the dipolar structure is starting to deform as a result of the interaction with shear, depending on either adverse or cooperative shear the adverse shear interaction is breaking up one of the two vorticity patches.

In the case the shearing background flow is present, initially the vortex dipole propagates perpendicularly into the channel. This is illustrated in Figure 7.4a. Afterwards, the shearing flow causes the vortex dipole to be advected into a certain direction along the channel length as shown in Figure 7.4b.

Moreover, the shear flow interaction causes the negative vorticity 'patch' to be deformed and disintegrated. The disintegration is visible as the negative vorticity core is smaller in size and there is a negative vorticity tail which has been 'shed' off the dipolar structure (Figure 7.4c,d). In this specific case, the negative vorticity patch has been deformed while the positive patch is only slightly deformed.
Consequently, the total circulation is no longer zero but is in this case positive. This results in an asymmetric dipolar vortex curving towards the lower channel wall.

The shearing background flow induces vorticity in the fluid as follows:

$$\omega = \frac{\partial v}{\partial x} - \frac{\partial u}{\partial y} \tag{7.1}$$

with the velocity component along the channel u and the velocity component perpendicular to the channel v. If the vorticity of the dipolar vortex has the same sign as the vorticity induced by the shearing flow then this is called 'co-operative shear' and if the vorticity of the dipolar vortex has the opposite sign as the vorticity induced by the shearing flow then this is called 'adverse shear'.

Earlier studies [9][28][29] have revealed that monopolar vortices in adverse shear interaction may break up. This is in contrast to cooperative shear interaction, which deforms the initially circular-shaped monopolar vortex into an elliptic monopolar vortex.
This effect is also visible in Figure 7.4, where the negative vorticity patch is experiencing an adverse shearing interaction and the positive vorticity patch is interacting cooperatively with the shear-flow.

7.4 Oblique fluid injection

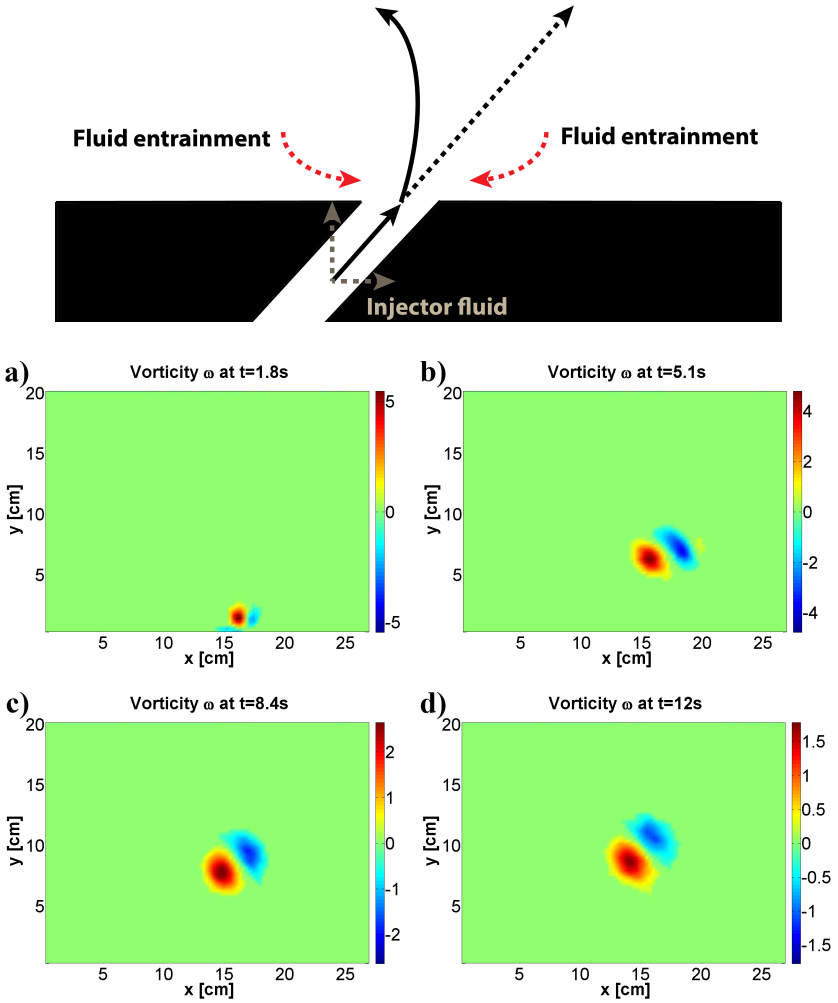

Figure 7.5: The top-half image is a sketch of the injection of a dipole at an angle. This causes an asymmetry in fluid entrainment and consequently the formation of an asymmetric dipole. The injection fluid velocity is decomposed in the x and y-direction and the dashed line arrow shows the straight path and the non-dashed arrow shows the actual (curved) path of the dipole after formation. The bottom-half shows experimental results of an oblique injection of fluid. This results in an asymmetric entrainment of fluid and consequently the formation of an asymmetric dipole. a) The formation of the dipole where the asymmetry in generated vorticity is already visible and this is also visible in the secondary vorticity produced. b,c,d) The dipole is following a curved trajectory caused by the asymmetric vorticity distribution.

The interaction between a dipole propagating at an angle and a background shear flow is studied next. Fluid is mechanically injected into channel at an angle to create a dipolar vortex with an oblique trajectory. This situation is illustrated in Figure 7.5. The dipolar vortex does not propagate along a straight trajectory (as in the case with a perpendicular injection), but has a curved path. This is due to an asymmetric geometry, which induces an asymmetric entrainment of fluid. This generates an asymmetric dipole with a curved path.

At this particular angle, the x-component of the velocity enhances the fluid entrainment from the left-hand side. While the fluid entrainment does not enhance fluid coming from the right-hand side. More fluid entrainment causes the dipole to be asymmetric and in this specific case, strengthens the left patch which has positive vorticity. This asymmetric dipole does not propagate along a straight path but initially bends towards the left as the net vorticity of the dipole is positive. The injection fluid velocity is decomposed in the x and y-direction.
The dashed line arrow shows the desired straight path and the non-dashed arrow shows the actual (bended) path of the dipole after injection.

This effect is shown experimentally in Figure 7.5. Figure 7.5a shows the formation of a asymmetric dipolar structure and the positive vorticity patch is already visibly larger in both size and strength. This results in a larger generation of secondary vorticity at the lower channel wall.
The asymmetric dipolar vortex continues to follow a curved trajectory path towards the left as shown in Figure 7.5b,c and d. This means that this particular mechanical dipole generation mechanism is not viable for creating a symmetric dipolar vortex with an angled trajectory.
Furthermore, parallel injections are also not possible, where a generated dipolar vortex propagates parallel to the channel and shearing background flow. This is because the piston mechanism is permanently mounted into the lower channel wall.

7.5 Applying the electromagnetic dipole generator in a shearing background flow

7.5.1 Parallel vortex-shear interaction

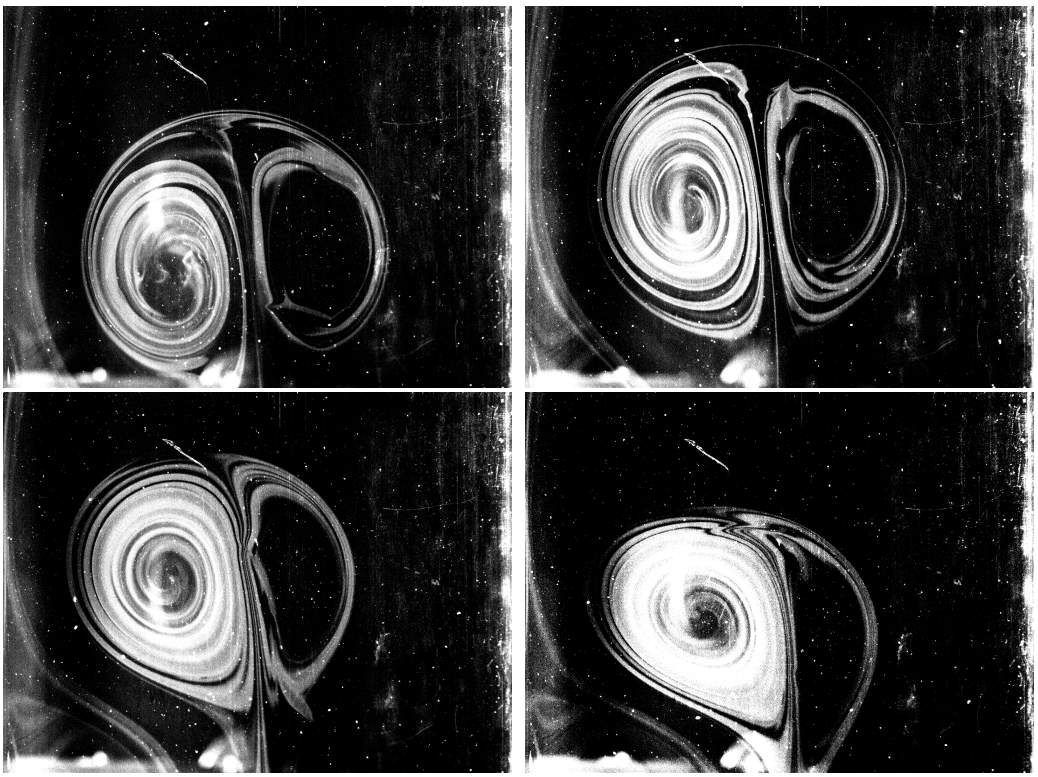

Figure 7.6: Dye visualization of a dipolar vortex propagating parallel into an adverse shearing background flow with a relatively large offset to the channel left-side, in gray-scale. The camera field of view is centred with respect to the channel walls and shearing background flow (velocity profile as shown in Figure 7.2).

Figure 7.6 shows four experimentally obtained snapshots of a generated dipole using the novel electromagnetic generation method propagating parallel with respect to the channel walls into an adverse shearing background flow. The profile of the shearing background flow is similar to the one shown in Figure 7.2.

The camera field of view is centred with respect to the two channel walls. The dipole in Figure 7.6a shows a small offset to the left-hand side of the channel. This small offset causes an asymmetric (adverse) shearing on the dipole. The asymmetric shearing causes a difference in deformation of the two vortex cores shown in Figure 7.6b,c and d.

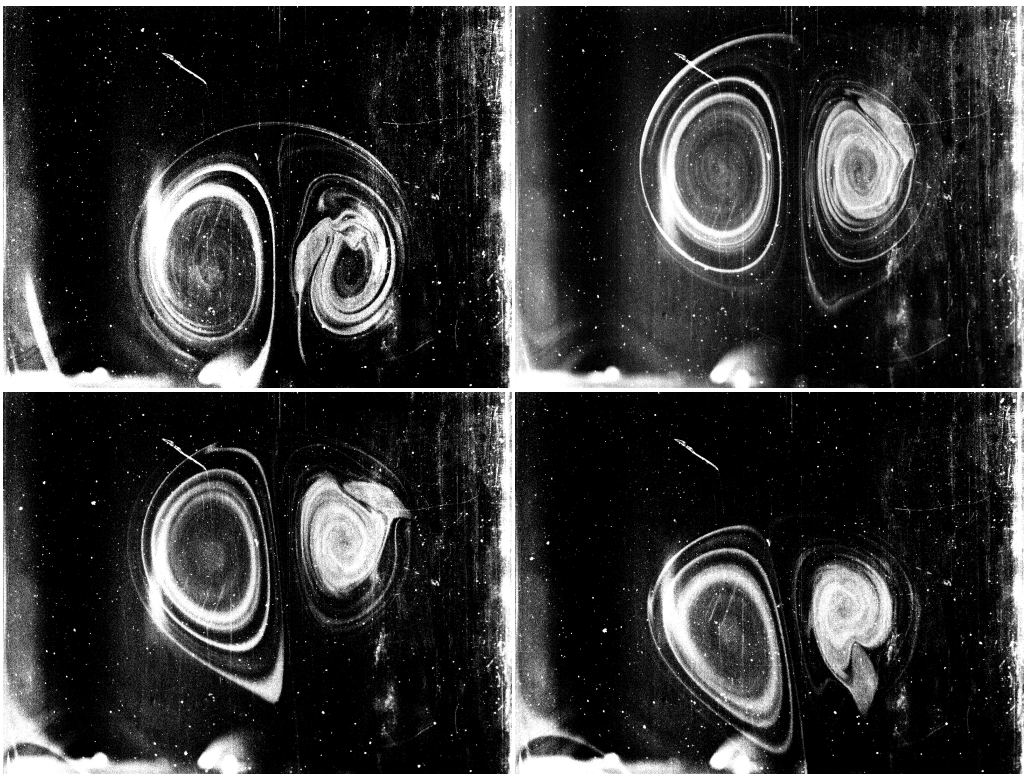

Figure 7.7: Figure showing a dipolar vortex propagating parallel to the adverse shearing background flow with only a slight offset to the channel left-side, in gray-scale. The camera field of view is centred with respect to the channel walls and shearing background flow (velocity profile is shown in Figure 7.2).

Figure 7.7 shows four experimentally obtained snapshots of a generated dipole also propagating parallel into the identical adverse shearing flow. However, the dipole shown in Figure 7.7a has a much smaller offset than the dipole shown in Figure 7.6a. Although there is less dye in the right vortex core, it is visible that the deformation is less pronounced in Figure 7.7b,c and d.

Chapter 8

Conclusions

The novel electromagnetical dipolar vortex generation method has been studied experimentally and numerically. As a first step, the generated dipoles have been characterized using the time evolution of the vorticity field, the vorticity cross-section, the vortex eccentricity ϵ and the ω-ψ scatter plots.
The generated dipole just after forcing has a point-dipole-like structure, gradually changing into a super-smooth-like dipole at an early time stage and finally evolving into a Chaplygin-Lamb dipole-like dipole at later time stages.

Subsequently, the generated dipoles have been studied with varied forcing parameters: the electric current I, the magnetic field strength B, the forcing time t_f and the electrode gap distance d_e.
This has been done by analyzing the effect of varied forcing parameter on: the maximum vorticity ω_{max}, vortex size d_v, the vortex core distance d_c, the vortex enstrophy decay time t_d, the dipole (centre) propagation velocity v_c and the ω-ψ scatter plots.

The novel generation method has been applied in experiments where the outcome is sensitive to propagation trajectories and showcased the method's ability to generate symmetric dipolar vortices with improved control over (initial) propagation trajectories.
Furthermore, the novel method has been applied in a shearing background flow and showcased the novel method as a minimally intrusive way of generating dipolar vortices in a background flow.

Recommendations for future studies

For future studies, the dipole generator can be applied into various experiments where a well-controlled environment is required. The generator can also be applied more extensively in experiments with a background shear flow. The effectiveness of the novel generator in the presence of background rotation can also be studied in the future.

Additionally, the formation stage(vorticity generation) can be investigated in a more detailed way. Furthermore, the effect of different electrode shapes (circular or rectangular) can be investigated and possibly more than two electrodes can be utilized.

References

[1] G. I. Taylor, Experiments on the motion of solid bodies in rotating fluids, Proc. R. Soc. Lond. A, 104, 725, 213-218 (1923).

[2] J. Proudman , On the motion of solids in a liquid possessing vorticity, Proc. R. Soc. Lond. A, 92, 408–424 (1916).

[3] L. Zavala Sansón, G. J. F.van Heijst and N.A. Backx, Ekman decay of a dipolar vortex in a rotating fluid, Phys. Fluids, 13, 440-451 (2001).

[4] P. Tabeling, O. Cardoso and B. Perrin, Chaos in a linear array of vortices. J. Fluid Mech., 213, pp 511-530 (1990).

[5] H. Honji, Y. Haraguchi, Electrolytically induced quasi-two-dimensional vortex pair, J. of the Phys. Soc. of Japan, 64, 2274-2277 (1995).

[6] J. B. Flór, H. J. S. Fernando, and G. J. F. van Heijst, The evolution of an isolated turbulent region in a twolayer fluid, Phys. Fluids, 6, 287 (1994).

[7] J. B. Flór and G. J. F. van Heijst, An experimental study of dipolar vortex structures in a stratified fluid, J. Fluid Mech., 279, 101-133, (1994).

[8] J. Albagnac, L. Lacaze, P. Brancher and O. Eiff, On the existence and evolution of a spanwise vortex in laminar shallow water dipoles, Phys. Fluids, 23, 6601 (2011).

[9] R. R. Trieling, J. M. A. van Wesenbeeck, and G. J. F. van Heijst, Dipolar vortices in a strain flow, Phys. Fluids, 10, 144 (1998).

[10] V.H.M.R Fernandes, to be published (2015).

[11] Batchelor, G. K. (1967), An Introduction to Fluid Dynamics, Cambridge University Press, ISBN 0-521-66396-2

[12] S. A. Chaplygin, 1903 One case of vortex motion in fluid. Trans. Phys. Sect. Imperial Moscow SOC. Friends of Natural Sciences 11, N 2, 11-14. Also In Collected Works, 2, 155-165 (1948) (in Russian).

[13] H. Lamb, 1895 Hydrodynamics (2nd edn). Cambridge University Press.

[14] V. V. Meleshko and G. J. F. van Heijst, On Chaplygin's investigations of two-dimensional vortex structures in an inviscid fluid. J. Fluid Mech., 272, 157—182 (1994).

[15] Z. Kizner, R. Khvoles and D. Kessler, Viscous selection of an elliptical dipole, J. Fluid Mech., 658, 492–508 (2010).

[16] R. Khvoles and Z. Kizner, Two variations on the theme of Lamb–Chaplygin: supersmooth dipole and rotating multipoles, Reg. Chaot. Dyn., 9, 4, (2004).

[17] R. Khvoles, D. Berson and Z. Kizner, The structure and evolution of elliptical barotropic modons, J. Fluid Mech., 530, 1–30 (2005).

[18] R. Trieling, R. Santbergen, G. J. F. van Heijst and Z. Kizner, Barotropic elliptical dipoles in a rotating fluid, Theor. Comput. Fluid Dyn., 24, 111–115 (2010).

[19] G. E. Swaters, Viscous modulation of the Lamb dipole vortex. Phys. Fluids, 31, 2745-2747 (1988).

[20] J. B. Flór, G. J. F. van Heijst, and R. Delfos, Decay of dipolar vortex structures in a stratified fluid, Phys. Fluids 7, 374 (1995).

[21] H. J. H. Clercx, G. J. F. van Heijst, and M. L. Zoeteweij, Quasi-two-dimensional turbulence in shallow fluid layers: The role of bottom friction and fluid layer depth, Phys. Rev. E 67, 066303 (2003).

[22] W. R. Orndorff and A. J. Hemmer, Fluorescein and some of its derivatives, J. Am. Chem. Soc., 49 (5), 1272–1280 (1927).

[23] G. J. F. Van Heijst and J. B. Flór, Dipole formation and collisions in a stratified fluid, Nature, 340, 212-215 (1989).

[24] S. I. Voropayev and Ya. D. Afanasyev, Two-dimensional vortex-dipole interactions in a stratified fluid, J. Fluid Mech., 236, 665- 689 (1992).

[25] S. Dubosq and Á. Viúdez, Three-dimensional mesoscale dipole frontal collisions, J. Phys. Oceanogr., 37, 2331–2344 (2007).

[26] G.J.F van Heijst, R.C Kloosterziel, C.W.M Williams, Laboratory experiments on the tripolar vortex in a rotating fluid, J. Fluid Mech., 225 , 301–331 (1991).

[27] J.A. van Hooft, The Dynamical Behavior of a Dipolar Vortex near Sharp-edged Boundaries, Master thesis, Eindhoven University of Technology (2015).

[28] Legras, Bernard, David G. Dritschel, and Philippe Caillol, The erosion of a distributed two-dimensional vortex in a background straining flow., J. Fluid Mech., 441, 369-398 (2001).

[29] O. Paireau, P. Tabeling and B. Legras, A vortex subjected to a shear: an experimental study, J. Fluid Mech., 351, 1-16 (1997).